UNIVERSIDAD DE CHILE
FACULTAD DE CIENCIAS FÍSICAS Y MATEMÁTICAS
DEPARTAMENTO DE ASTRONOMÍA

INDEPENDENT EVIDENCE FOR THE COSMIC ACCELERATION FROM TYPE II SUPERNOVAE.

TESIS PARA OPTAR AL GRADO DE DOCTOR EN CIENCIAS, MENCIÓN ASTRONOMÍA

THOMAS MAXIMILIEN de JAEGER

PROFESOR GUÍA:
MARIO HAMUY WACKENHUT
MIEMBROS DE LA COMISIÓN:
ALEJANDRO CLOCCHIATTI GARCÍA
PAULINA LIRA TEILLERY
RENÉ MÉNDEZ BUSSARD

SANTIAGO DE CHILE
2016

RESUMEN DE LA TESIS PARA OPTAR AL GRADO DE DOCTOR EN CIENCIAS, MENCIÓN ASTRONOMÍA

EVIDENCIA INDEPENDIENTE DE ACCELERACIÓN CÓSMICA A PARTIR DE SUPERNOVAS DE TIPO II

El trabajo de tesis se titula “Evidencia independiente de acceleración cósmica a partir de supernovas de tipo II”; y tiene como objetivo estudiar la utilidad de las supernovas de tipo II como indicadores de distancias extragalácticas. Las supernovas tienen potencial para ser usadas como patrones lumínicos. Los patrones lumínicos son objetos luminosos para los cuales se conoce su brillo intrínseco, permitiendo medir distancia usando la ley del cuadrado inverso. La medición de distancias es un elemento fundamental para caracterizar la expansión del Universo. Con estos datos y aplicando modelos teóricos uno puede restringir parámetros cosmológicos tales como la cantidad de materia oscura o de energía oscura.

Durante la ultima década usando las supernovas de tipo Ia (explosiones estelares termonucleares), dos grupos de investigadores (Riess et al., 1998; Perlmutter et al., 1999; Schmidt et al., 1998) lograron medir distancias muy lejanas y demostrar que el Universo está actualmente en un estado de expansión acelerada. Aunque otros experimentos denominados “Oscilaciones Acústicas Bariónicas” y “Fondo de Radiación Cósmicos” han confirmado estos sorprendentes resultados y tienen sus propios méritos, estás técnicas no están libres de errores sistemáticos. Es por eso que necesitamos desarrollar la mayor cantidad de métodos posibles para obtener mejores estimaciones de los parámetros cosmológicos. Ha habido múltiples trabajos que demostraron que las supernovas de tipo II también constituyen competitivos indicadores de distancias para la determinación de distancias extragalácticas. El objetivo de esta tesis es refinar estos métodos y desarrollar nuevas técnicas para medir distancias en el Universo.

En este trabajo nos proponemos desarrollar y refinar métodos para usar supernovas de tipo II como indicadores de distancia. Para la primera parte de esta tesis, vamos a usar datos de bajo redshift que provienen del Carnegie Supernova Project (CSP, Hamuy et al. 2006). Vamos a desarrollar un método que permita corregir y estandarizar las supernovas usando sólo datos fotométricos (sin usar información espectroscópica). Estandarizar las supernovas significa corregir las magnitudes por diferencias intrínsecas, para que al final las diferencias de brillo observadas entre los diferentes objetos dependan solamente de distancia. Debido a la alta calidad de los datos también vamos a poder refinar el método propuesto por Hamuy & Pinto (2002) para lo cual se necesitan espectros. La segunda parte de la tesis será la extensión de estos dos métodos a más alto redshift con el fin de caracterizar los parámetros cosmológicos. Para esto usaremos datos del Sloan Digital Sky Survey y del Supernova Legacy Survey. Lograremos mostrar que los métodos de bajo redshift pueden ser aplicados a alto redshift y además podremos derivar parámetros cosmólogicos consistentes con el modelo actual.

SUMMARY OF THESIS FOR THE DEGREE OF DOCTOR OF PHILOSOPHY IN ASTRONOMY

INDEPENDENT EVIDENCE FOR THE COSMIC ACCELERATION FROM TYPE II SUPERNOVAE

The purpose of this thesis entitled “Independent evidence for the cosmic acceleration from Type II supernovae” is to study the usefulness of Type II supernovae as extragalactic distance indicators. Supernovae have shown a great potential to be used as standard candles. Standard candles are astrophysical sources for which the intrinsic brightness is known, and thus, applying the inverse square law, distances can be measured. A fundamental probe in modern astronomy to understand the Universe is the measurement of distances. Using observed data and theoretical models one can constrain cosmological parameters such as dark energy or matter densities.

For more than two decades, Type Ia supernovae (thermonuclear explosion) have been used as standard candles in cosmology and led to the revolutionary discovery of the accelerated expansion of the Universe driven by an unknown force attributed to dark energy (Riess et al., 1998; Perlmutter et al., 1999; Schmidt et al., 1998). Over recent years, several techniques have confirmed these surprising results: refined versions of the SNe Ia method, cosmic microwave background radiation measurements, and baryon acoustic oscillation measurements. All of the above techniques have their own merits, but also their own systematic uncertainties that could become dominant with the increasingly higher level of precision required. Thus, it is important to develop as many methods as possible, since the truth will likely emerge from the combination of different independent approaches. Hamuy & Pinto (2002), showed that Type II supernovae can also be used as independent distance indicators. The purpose of this thesis is to refine these methods and develop new techniques to measure distances in the Universe.

In this work, I will use Type II supernovae (SNe II) as distance indicators. First, using the low redshift data sample from the Carnegie Supernova Project (CSP, Hamuy et al. 2006), I will develop a new method to correct and to standardise the SNe II solely from photometry, with no input of spectral information. Standardise means correcting the magnitudes for intrinsic differences, so the difference in the observed brightness between two objects is only due to difference in distance, in the sense of more distance less bright. Thanks to the high data quality, I will also be able to refine the most common method used to derive SNe II distances for which spectra are needed (Hamuy & Pinto, 2002). The last part of my work will consist to extend these two methods to higher redshift in order to derive the cosmological parameters. For this purpose, I will use data from the Sloan Digital Sky Survey and from the Supernova Legacy Survey. I will succeed in extending these methods at high redshift and in deriving cosmological parameters consistent with the current cosmological model.

Dedicated to Daniela

Acknowledgements

En primer lugar quiero agradecer a mi Profesor guía Mario Hamuy quien fue la razón de mi llegada a Chile. Le doy mis sinceras gracias por haberme transmitido todo su entusiasmo y sobre todo una parte su conocimiento para permitirme llevar a cabo mi tesis. Gran parte del científico que soy le debo a él. Quiero dar las gracias a Santiago González-Gaitán quien fue mi extraoficial co-supervisor para responder a todas mis preguntas/dudas. Quiero agradecer a Paulina Lira, Alejandro Clocchiatti y René Méndez por ser parte de mi comité. Me gustaría agradecer también al grupo de supernovas (Hanin Kuncarayakti, Lluis Galbany, Claudia Gutierrez, Francisco Forster) y especialmente a Joe Anderson quien me ayudo enormemente a mi llegada en el grupo de supernovas. Si los días en Calán fueron más agradables es gracias a mis compañeros y sobre todo los de mi oficina (Felipe, Celia, Zeus, Sergio, Seba, Julián y Ale) con quienes hemos tenido largas e intensas charlas/juegos. Agradezco a todos los profesores de Calán por haber participado a mi desarrallo científíco. No quiero omitir a James quien me acompañó durante largas tardes a mirar los partidos de fútbol. Tampoco quiero olvidar los funcionarios de Calán y en particular a Marta y Nati por la ayuda en los tramites, la Señora Maria y Jorge por sus ricos almuerzos, la Señora Nelly por su buena onda, los compañeros de almuerzo Alejandro, Lucho Lalo, Ricardo, Jose, Francisco, Pablo por sus entretenidas discusiones y por fin Rogelio, Lucas, Alejandro por los partidos de fútbol. Je voudrais aussi remercier mes amis de France, ceux du Kartier, les gaziers mais aussi ceux de Paul Sab pour leurs soirées d'anthologies et pour cette amitié qui ne disparaîtra jamais malgré la distance. Une petite pensée aussi pour mes amis français chiliens et nos discussions rugbystiques et le fameux colonel.

Bien entendu cette thèse n'aura jamais pu voir le jour sans le soutien inconditionnel de ma famille, celui de mes parents et de mon frère qui m'ont toujours aidé et encouragé dans cette voie. Je suis reconnaissant de vous avoir comme famille.

Finalmente quiero agradecer a mi "belle famille" por haberme acogido en su familia haciendo mi estancia en Chile más agradable y sobre todo quiero dar mis infinitas gracias a la persona mas importante de mi vida, mi amada Daniela. Me siento muy afortunado de tenerla a mi lado y sentir su absoluto apoyo. Siempre ha creído en mis capacidades y mi amor por ella me ha obligando a superarme para no defraudar su confianza. Este trabajo recibió el apoyo del Instituto Milenio de Astrofísica (MAS) a través de la beca IC120009 financiado por el Ministerio de Economía, Desarrollo y Turismo.

Table of Contents

List of Figures

List of Tables

Chapter 1

Introduction

Contents

1.1 Supernova

1.1.1 Background and classification

1.1.1.1 Historical background

A supernova is a violent stellar explosion that briefly outshines an entire galaxy ($10^9 - 10^{10} L_\odot$). The word supernova was first introduced in 1934 by Baade & Zwicky (1934), coming from the Latin "novae" which means "new" and refers to the appearance of a bright new object in the sky. The suffix "super" was added when we understood that the nebulae which hosted these enormous explosions were, in fact, galaxies at great distances outside the Milky Way (Hubble, 1926). These amazing objects are so bright that some of them are visible to the naked eye and were observed long before the use of the telescope. Even if these naked-eye supernovae are rare, at least, five events have been seen in our Galaxy and well-detailed records can be found.

The first observation of such objects was done in AD 185 between the constellations Circinus and Centaurus by Chinese astronomers. They described the phenomenon as a strange star which appeared in the middle of Nan Mun and looked like a large bamboo mat. The second object identified in our Galaxy was also the brighter explosion ever seen in the Milky Way. In AD 1006, in the constellation Wolf, astronomers from Asia, Africa or Europe had described this object as "a large circular body, 2-3 times as large as Venus" and had the chance to see this spectacle during at least two years. In AD 1054, another less luminous stellar explosion occurred in the constellation Taurus. This very famous supernova was observable for several months and later faded back out of sight to what today is known as the Crab nebula (cf Figure 1.1). The last two events which occurred in our Galaxy were observed in Europe during the late sixteenth century by two very famous astronomers: Tycho Brahe and Johannes Kepler (1572 and 1604 respectively). Note also we can mention one very important supernova which exploded in the nearby dwarf galaxy, the Large Magellanic Cloud. This object named SN 1987A, is crucial in the understanding of the supernovae physics and was the first detection of neutrinos outside our Solar System (Hirata et al., 1987; Bionta et al., 1987).

1.1.1.2 Classification

Historically, the supernovae (SNe, hereafter) were classified into two groups based on their spectral characteristics (Minkowski, 1941): Type I class was characterised by the absence of Hydrogen and Type II are those showing a spectrum dominated by strong Hydrogen Balmer lines.

With the increase of the data quality it became easier to differentiate the Type I group in three subgroups according to the presence of the Si II $\lambda 6355$ line (subgroup Ia), the absence of the Si II $\lambda 6355$ line coupled with the presence of the He I $\lambda 5876$ line (subgroup Ib), and finally the absence of both lines (subgroup Ic) (Harkness & Wheeler, 1990).

The Type II group was also divided into subgroups based on spectral features (see Filippenko 1997; Howell 2011 for review): the SNe IIb which evolve spectroscopically from SNe IIP/L at early time to H I deficient few weeks to a month past maximum (Woosley et al., 1987), SNe IIn which have narrow H I emission lines (Chevalier 1981; Fransson 1982; Schlegel 1990; Chugai & Danziger 1994; Van Dyk et al. 2000; Kankare et al. 2012). In the past, Type II was also separated in two more subgroups based on the photometric properties: SNe IIP which are characterised by long duration plateau phases (≤ 100 days) of constant luminosity, and SNe IIL which have linearly declining light curve morphologies (Barbon et al., 1979). However, as discussed in detail in Anderson et al. (2014b); Sanders et al. (2015); Valenti et al. (2016), it is not clear how well this terminology describes the diversity of SNe II, which suggested that the

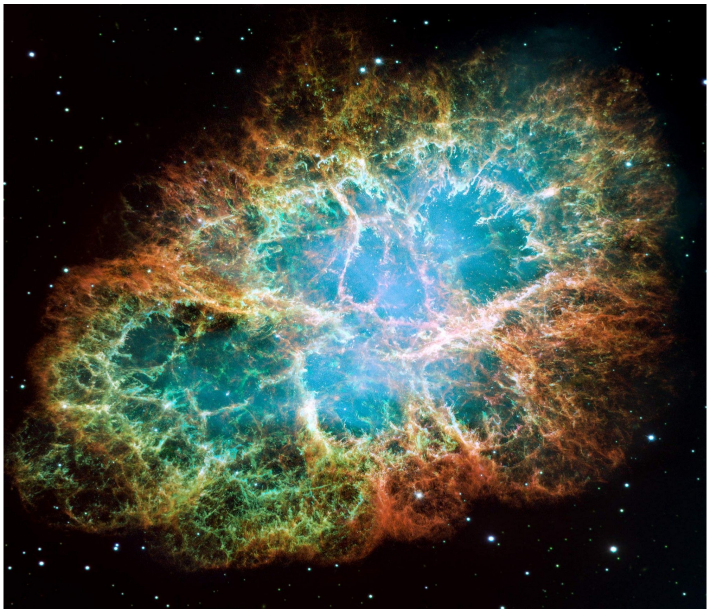

Figure 1.1: Crab nebula, the result of the supernova 1054. The orange filaments are the tattered remains of the star and consist mostly of Hydrogen. The blue light comes from electrons whirling at nearly the speed of light around magnetic field lines from the neutron star. The colours in the image indicate the different elements that were expelled during the explosion. Blue in the filaments in the outer part of the nebula represents neutral oxygen, green is singly ionised sulphur, and red indicates doubly-ionised oxygen. The image was taken by the Hubble Space Telescope. Image Credit: NASA, ESA, J. Hester, A. Loll (ASU).

SNe II family forms a continuous class. Some authors (Arcavi et al., 2012; Faran et al., 2014a,b) have argued for two separate populations but their results are affected by low number statistics.

This simple observational classification was later improved by theorists and lead to modern classification. By 1934, Baade and Zwicky suggested that SNe came from stars collapsing into neutron stars (Baade & Zwicky, 1934; Zwicky, 1935) which is consistent with SNe II models but could not explain the nature of SNe Ia. Unlike SNe Ibc, SNe Ia do not occur only in star forming regions of galaxies but also in elliptical galaxies which suggests that they do not come from massive stars (van den Bergh, 1959; Filippenko, 1989; van den Bergh, 1990; Anderson et al., 2012; Habergham et al., 2014).

The current picture of SNe nature is that Type II and Ibc all come from the collapse after a few million years[1] of evolution of massive stars with zero-age main-sequence mass[2] $\geq 8\ M_{\odot}$ (Woosley & Weaver, 1995; Arnett, 1996; Burrows, 2000; Smartt, 2009) and lead to the formation of a neutron star or, in some cases, to a black hole (Bethe, 1990). On the other hand, SNe Ia are not Core-Collapse Supernovae (CCSNe) but are believed to originate from the thermonuclear explosion of a carbon-oxygen (C-O) white

---

[1] $t_{MS} \sim (\frac{M}{M_{\odot}})^{-3.5} 10^{10}$ yrs

[2] Refers to the mass of the progenitor star at the time when Hydrogen burning is first initiated

dwarf in a binary system and that leaves no compact remnant (Hoyle & Fowler, 1960).

For the sake of completeness it should be pointed out that in addition to the classification described above, the existence of transients which have originally been defined as SNe IIn, but a link to a definitive SN event is questionable. Such events have been defined as SN "impostors" (Van Dyk et al., 2000; Maund et al., 2006) and are believed to be luminous non–terminal eruptions of massive stars. There are multiple cases of such events(Pastorello et al. 2013; Van Dyk et al. 2000; Tartaglia et al. 2015; Smith et al. 2011) and in particular one object SN 2011A for which I found that it was an impostor event due to its faint magnitude ($M_V \geq 15.72$), its small P-Cygni H_α velocity (≤ 1200 km s^{-1}) and the presence of the double plateau in light curve likely due to circumstellar medium composed of two interacting shells. This work led to a publication in the Astrophysical Journal (ApJ) as first author (de Jaeger et al., 2015a).

Figure 1.2 displays a summary of the modern classification diagram that allows one to disentangle the different SNe using spectral and photometric features (Ia, Ib, Ic, II, IIn, IIb) or the theoretical nature of the SNe: thermonuclear (see Section 1.1.2) or core-collapse (see Section 1.1.3).

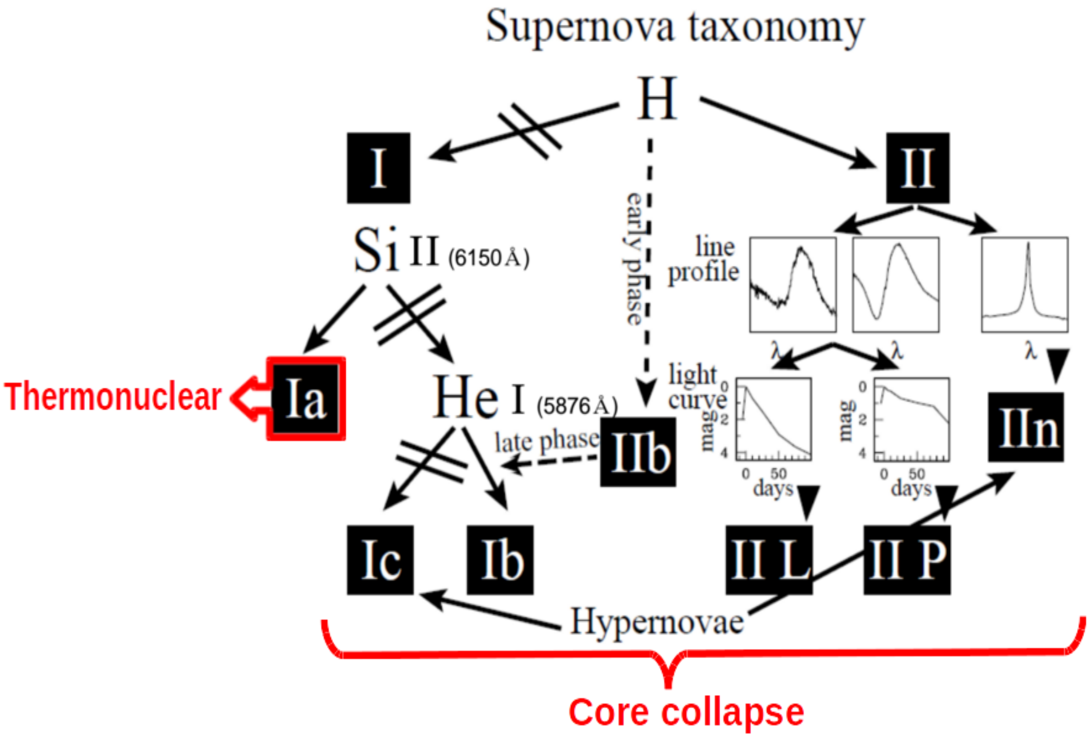

Figure 1.2: The detailed classification of SNe from Cappellaro & Turatto (2001).

1.1.2 Thermonuclear Supernovae: Type Ia

1.1.2.1 Formation

The lack of Hydrogen lines in their spectra and their occurrence in every galaxy type suggest that SNe Ia are evolved objects (associated with an old stellar population) and thus, originate from long-lived low-mass stars ($\leq$ 8 $M_\odot$) that end up their lives as carbon-oxygen white dwarfs (WDs) with typical mass distribution which peaks at 0.6 $M_\odot$. As our Sun, these WDs can die after releasing all their internal heat during billions of years but they also can end up as SNe Ia if they happen to be in a binary system. In the standard scenario, mass from the binary companions can be accreted ($\dot{M} \sim 10^{-8}$ to 10^{-6} $M_\odot$ yr^{-1}) into the WD nearing the Chandrasekhar limit ($\sim$ 1.4 $M_\odot$,Chandrasekhar 1931), i.e., the maximum mass above which a WD's electron degeneracy pressure is unable to sustain the self-gravity of the star. Then the C/O material can be ignited and because the WD is degenerate, the pressure does not increase with the increasing temperature, nothing can control thermonuclear reaction: this burning becomes explosive and destroys the entire star. The temperature is sufficient to start the thermonuclear reaction and form iron-peak and intermediate-mass elements which are ejected to the interstellar medium. Note that no remnant is present after the explosion.

We know the general picture of the SNe Ia progenitor: a WD in a binary system (Hoyle & Fowler, 1960) but the exact nature of its companion is still in debate. Currently, three different models are proposed: the single-degenerate (SD; Whelan & Iben 1973; Arnett 1996; Hillebrandt & Niemeyer 2000; Thielemann et al. 2004) scenario, the double degenerate (DD; Iben & Tutukov 1984; Webbink 1984) scenario and the sub-Chandrasekhar scenario (subCh; (Nomoto, 1982a,b; Woosley & Weaver, 1994)) which is similar to the SD scenario.

In the SD scenario, a C/O WD accretes Hydrogen-rich or helium-rich material from a non-degenerate companion star, increases its mass to the Chandrasekhar mass limit, and then explodes. This scenario can explain the homogeneities in SNe Ia light curves but how this scenario explains the lack of Hydrogen seen in SNe Ia? This problem was solved recently by the discovery of the SNe Ia which presents H_α lines (e.g. SN 2002ic), and suggests that at least some SNe Ia are the result of accretion from a giant star (Hamuy et al., 2003; Deng et al., 2004; Kotak et al., 2004).

For the DD scenario, two WDs in a binary system whose combined mass exceeds the Chandrasekhar limit, merge due to the loss of gravitational wave radiation. This model can explain for example the absence of Hydrogen lines but current models of WDs merger can only produce sub-luminous SNe Ia (Pakmor et al., 2010). Unfortunately, the DD scenario leads to the formation of compact object which at are not observed after SNe Ia explosions (Saio & Nomoto, 1985).

In the sub-Chandrasekhar model, a helium-accreting C/O WD explodes below the Chandrasekhar mass due to an explosive burning initiated in the thick helium shell which triggers a secondary core detonation by compressional heating (Nomoto, 1982a,b; Woosley & Weaver, 1994).

To summarise, SNe Ia can originate via multiple channels, where each scenario could have its own contribution and to date no scenario has been favoured.

1.1.2.2 Photometry

SNe Ia are extremely bright, i.e., $M_B \sim -19.25$ (Richardson et al., 2014), and have very homogenous light curve properties. Most of the energy from the explosion is released by kinetic energy (1.3×10^{51} ergs) to unbind the star and to eject the material ($\sim 10^4$ km s^{-1}). To explain the observed light-curve, another source of energy is needed, and this energy is provided by the radioactive beta decay of ^{56}Ni to ^{56}Co and then to ^{56}Fe ($\sim$0.6 M$_\odot$,Truran et al. 1967; Colgate & McKee 1969; Arnett 1982). Overall, the SNe Ia light curve shape is determined by the competition between three effects: the conversion of internal energy to kinetic energy, the deposition of energy from radioactive decay (1.0×10^{49} ergs), and finally, the escape of internal energy as the observed light curve (Pinto & Eastman, 2000).

At the beginning, the ejecta is tremendously optically thick, the photon diffusion time is bigger than the time since the explosion. Thus, all of the energy liberated in the explosion is converted into kinetic energy. As the star expands, the ejecta becomes more diluted, the optical depth decreases and this energy can escape in shorter timescales. The luminosity increases and after typically 18 days after the explosion (Hayden et al., 2010) reaches a maximum. Because the energy deposition by the radioactive burning products decreases exponentially with time, the peak luminosity occurs when the diffusion time-scale becomes comparable to the expansion time-scale, i.e, when the fraction between the product of the rising escape and the decreasing deposition of energy is maximum. As the ejecta expands the decay of ^{56}Ni to ^{56}Co (half-life=5.5 days, $\sim$ 0.087 mag/days) releases energy into the ejecta which powers the optical light curve (few weeks after explosion). Afterwards ($\sim$ 60 days post-explosion) the photon diffusion time is so short that the radiation escapes freely and the luminosity follows the instantaneous energy deposition which at that time is dominated by the decay of ^{56}Co to ^{56}Fe (half-life=78 days, $\sim$ 0.015 mag/days). During these radioactive decays, a lot of gamma photons interact with the ejecta by photoelectric absorption, Compton scattering and pair-production, and are finally thermalised to optical, near-ultraviolet, and near-infrared photons.

One important characteristic of SNe Ia light curves is their homogeneity. The shape and the peak luminosity depend on the amount of ^{56}Ni, i.e, more ^{56}Ni for brighter SNe Ia. Phillips (1993) derived a relation between the luminosity at peak and the light curve shape, in the sense that brighter SNe Ia decline more slowly. The original relation found by Phillips (1993) is shown in the top of Figure 1.3 and the bottom figure shows some low redshift SNe Ia light curves from the Calán-Tololo survey (Hamuy et al., 1996) in which we can clearly see that the brightest supernovae decline slower (Salmon colour). More information about this relation and the use of the SNe Ia as standard candles will be given in Section 1.2.2.

1.1.2.3 Spectroscopy

The spectroscopic evolution of the SNe, in general, can be divided into two phases: the photospheric phase and the nebular phase. During the photospheric phase, the ejecta is optically thick (optical depth equals to 1) and a continuum radiation field is emitted by a photosphere which can be regarded as an infinitely thin layer. The photosphere is defined as the mass zone where the electron scattering optical depth in B band turns above 2/3. Above the photosphere, the radiation interacts with an optically thin "atmosphere" where the absorption lines are formed by scattering (Branch et al., 2003). As the SN expands, the photosphere recedes in mass coordinates and it is possible to look directly to the inner parts of the star, and inner products of the explosion appear in the spectra. The nebular phase starts when the whole SN ejecta is optically thin. During this phase, the emitted photons escape directly, and the spectrum consists of emission lines. Note that there is no sharp division between the two phases and the duration of the photospheric phase depends on the SN progenitors, the more compact, the shorter the photospheric phase.

At the beginning, the SNe Ia spectra show a lack of H and He lines with abundant intermediate mass elements such as Si II, S II, O I, and Ca II. Near the maximum, additionally to the latter lines, the spectra show iron lines such as Fe II, and Fe III. Finally, during the nebular phase, the spectra become dominated by emission lines due to forbidden transitions of [Fe II], [Fe III], and also [Co III].

1.1.3 Core-collapse Supernovae: II, Ib, Ic

1.1.3.1 Formation

It is believed that CCSNe have massive progenitors with zero-age main-sequence mass ≥ 8 $M_\odot$ (Smartt, 2009). Massive stars have a quick evolution of few millions years (see Woosley et al. 2002 for review), during which a nuclear fusion of higher mass elements starting with Hydrogen occurs one after the other until the formation of an iron core. These burning stages become faster and faster as heavier elements are produced by the fusion of lighter elements. The evolution of these stars ends up in an onion-like star with heavier elements in the centre, and shells of successively lighter elements burning around this iron core as is presented in Figure 1.4 (also figure (a) from Figure 1.5)

To this final stage, the enormous mass of the star has been supported against gravity by the energy released in fusing elements. Unfortunately, iron is the most stable element (highest binding energy per nucleus), thus the iron fusion does not create more

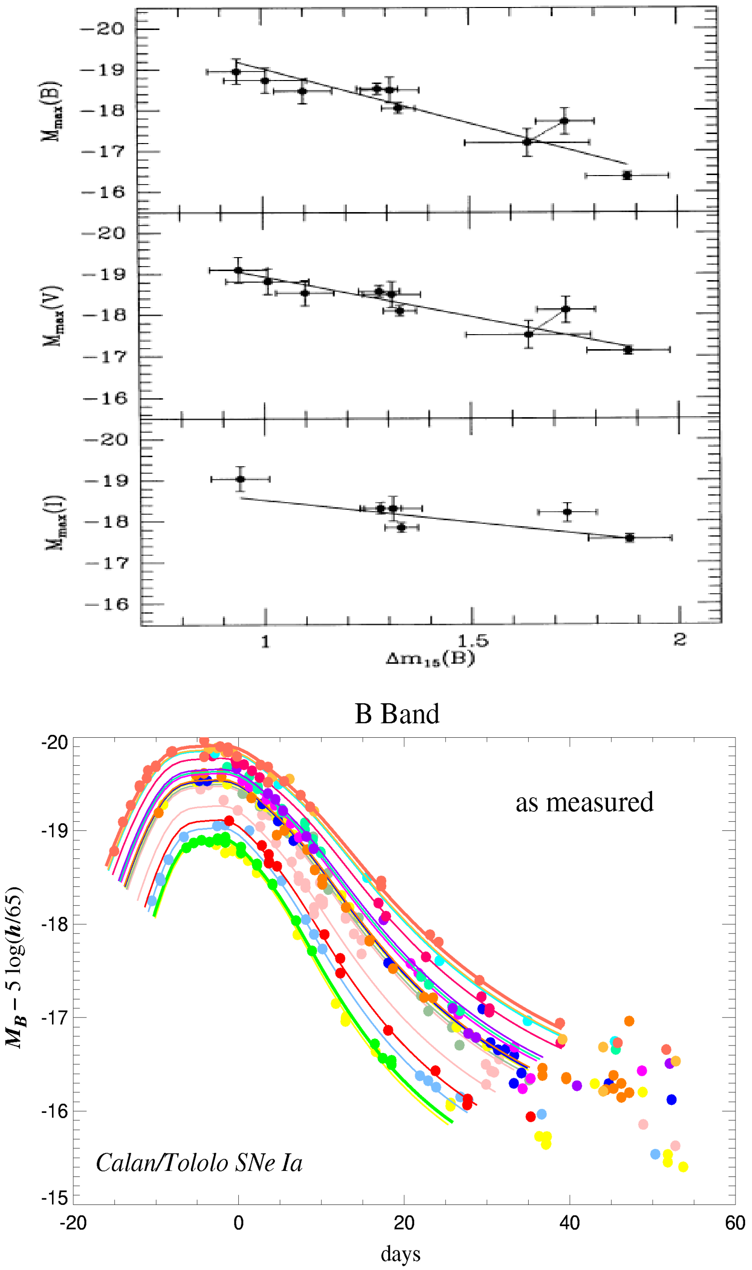

Figure 1.3: *Top figure:* The original plot from Phillips (1993) showing the relation between the luminosity at peak and the decline rate presented as Δ_{m15}, i.e., the decline rate between the peak and 15 days after the explosion. *Bottom figure:* SNe Ia B-band light curves from Calán-Tololo are presented (Hamuy et al., 1996).

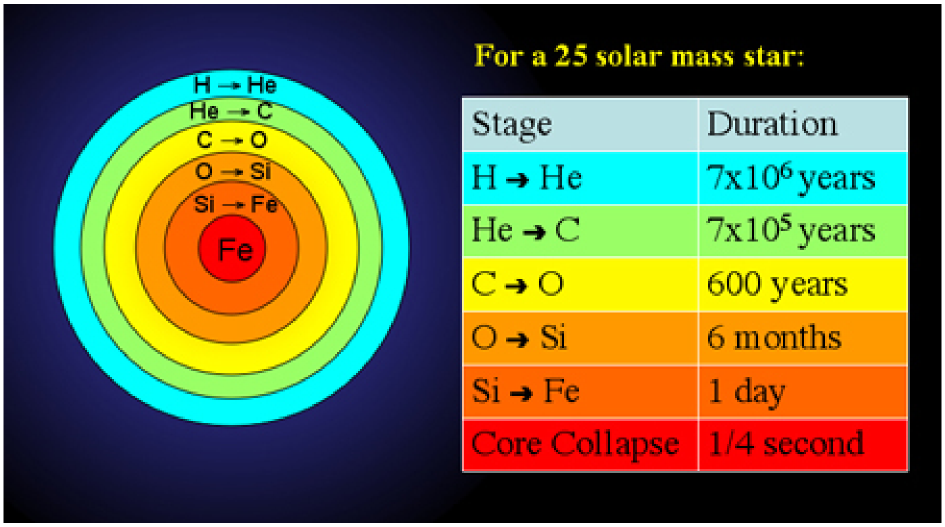

For a 25 solar mass star:

Stage	Duration
H → He	$7\text{x}10^6$ years
He → C	$7\text{x}10^5$ years
C → O	600 years
O → Si	6 months
Si → Fe	1 day
Core Collapse	1/4 second

Figure 1.4: The onion-like structure of a massive star ($M=25M_\odot$) before collapsing with the duration for each step. Copyright Swinburne University of Technology.

energy than it takes to produce it and the fusion processes stop. No more energy is available to fight against gravity. The iron core will grow to the Chandrasekhar mass and because the pressure provided by the electrons becomes insufficient to balance gravity, the core is condemned to gravitational collapse in few milliseconds timescale (figure (b) from Figure 1.5). During this collapse very high energy gamma rays are released which photo-dissociate iron nuclei into neutrons and α particles[3]. This process releases vast quantities of neutrinos and neutrons as the core density increases and electrons are captured. The contraction is finally stopped when the neutron degeneracy pressure counterbalances the gravity (figure (c) from Figure 1.5). Therefore, the falling matter rebounds in a shock wave propagating outwards (figure (d) from Figure 1.5). The shock begins to stall as it propagates against the flow of infalling material (figure (e) from Figure 1.5). At this point, a new energy source is needed. We believe that the escaping neutrinos could play this role and blast the outer layers away. We know that in normal circumstances neutrinos interact very weakly with matter, but here in these extreme densities/temperatures in the collapsing core, few neutrinos could be trapped between the proto-neutron star and the stalled shock (Mayle & Wilson, 1988; Burrows & Goshy, 1993; Janka, 2001). The energy of these trapped neutrinos increases the temperature and pressure behind the shock wave, which in turn gives it strength as it moves out through the star. The collapse results in a compact object such as a neutron star or a black hole, depending on the initial mass of the star, and the formation of elements heavier than iron by neutron capture (figure (f) from Figure 1.5).

---

[3] two protons and two neutrons bound together into a particle identical to a helium nucleus.

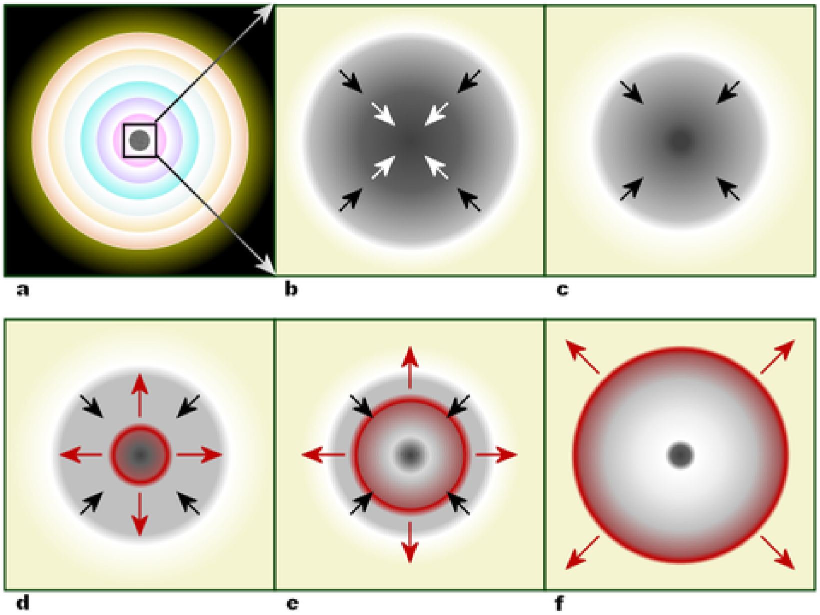

Figure 1.5: Simplified core collapse scenario. (a) Onion-layered shells of elements undergoing fusion with an inert iron core. (b) This iron core reaches Chandrasekhar-mass and starts to collapse (c) The inner core compresses into neutrons and the gravitational energy is converted into neutrinos. (d) The infalling material bounces off the nucleus and forms an outward-propagating shock wave (red). (e) The shock begins to stall as nuclear processes drain energy away, but it is re-invigorated by interaction with neutrinos. (f) The material outside the inner core is ejected, leaving behind only a degenerate remnant. Credit to R.J. Hall

1.1.3.2 Progenitors

CCSNe have a large variety of observed properties (mass, metallicity,...) which results from a diverse range of progenitors (see Smartt 2009, 2015 for review). Thanks to direct detections and hydrodynamical models and other evidences like environments, SNe II progenitors are believed to come from red supergiants (RSG) with low mass (8 - 20 $M_\odot$, Grassberg et al. 1971; Falk & Arnett 1977; Chevalier 1976; Van Dyk et al. 2003; Smartt et al. 2009; Anderson et al. 2012; Habergham et al. 2014). It has also been suggested that fast decliners SNe II progenitors have smaller Hydrogen envelopes (less than ~ 2 $M_\odot$ Popov 1993) and may also be more massive than slow decliners SNe II (Elias-Rosa et al., 2010, 2011)

The origin of SNe Ibc is believed to originate from Wolf-Rayet stars (WR) which are evolved, single massive stars that have lost their Hydrogen envelopes (WR with strong nitrogen emissions lines: SNe Ib) and also helium layers (WR with dominant carbon/oxygen (C/O) emission lines: SNe Ic) primarily through radiatively driven winds (Vink & de Koter, 2005) or episodic mass-loss (Smith & Owocki, 2006; Vink, 2008). Another possibility for the SNe Ibc progenitor is that they come from lower mass stars that lost their envelopes through stripping from mass transfer in a binary system (Podsiadlowski et al., 1992; Eldridge et al., 2008). SNe Ic progenitor discoveries through pre-explosion images have been inconclusive but recently one SNe Ib progenitor has been found. iPTF13bvn, a SNe Ib, gives the first evidence of a binary progenitor for this kind of supernova (Bersten et al., 2014; Folatelli et al., 2015, 2016).

1.1.3.3 Photometry

The total gravitational energy released during the collapse is about 100×10^{51} ergs. Unlike SNe Ia, almost all of this energy is radiated away in the form of neutrinos (~ 99 %). A very small fraction of the energy (1.0×10^{51} ergs) goes into accelerating a shock wave which heats and accelerates the matter at velocities up to $\sim 10\ 000$ km s^{-1}. Even if CCSNe are more energetic than SNe Ia they are less bright because only a small fraction of the energy is released as electromagnetic radiation, around $0.1 - 1 \times 10^{49}$ ergs. SNe II have an absolute magnitude peak magnitude in B-band around -17.0 mag against -18.0 mag for the SNe Ibc. (Richardson et al., 2014)

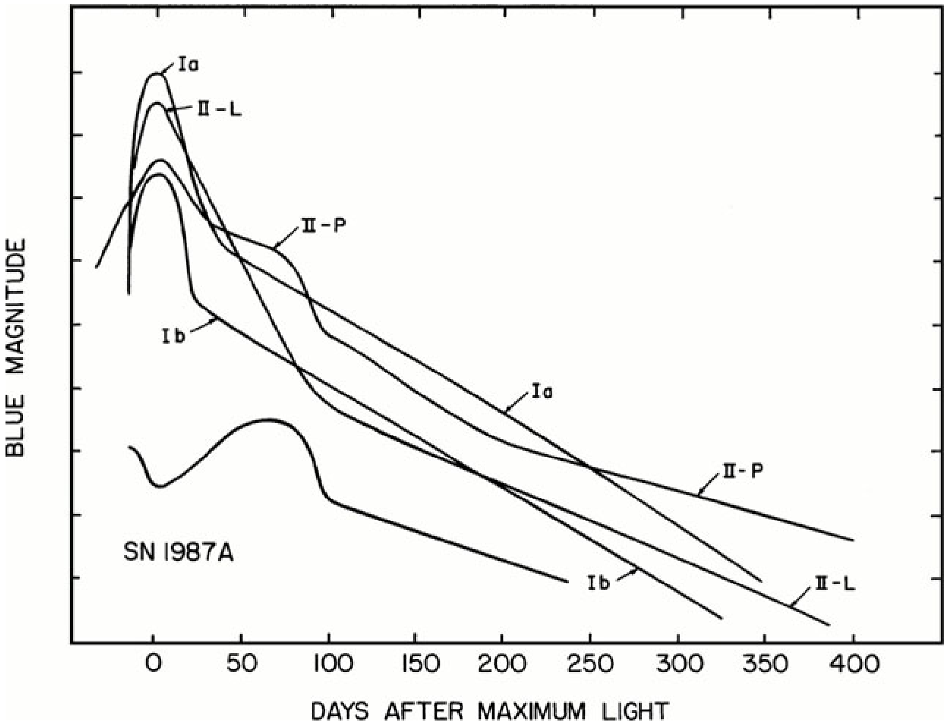

Figure 1.6: Schematic light curves for SNe of Types Ia, Ib, II-L, II-P, and SN 1987A. The curve for SNe Ib includes SNe Ic as well, and represents an average. For SNe II-L, SNe 1979C and 1980K are used, but these are unusually luminous (Wheeler & Harkness, 1990)

The CCSNe light curves show a huge variety of shapes, depending upon the mass of the envelope, the radius of the progenitor, energy of the explosion, and mass of

^{56}Ni produced. In Figure 1.6 from Wheeler & Harkness (1990), we show the schematic light curves for different types of SNe: SNe Ia, SNe Ib, SNe IIL, SNe IIP. Even if all these light curves show differences (plateau, linear decline...) we can describe here a typical light curve of a red supergiant, i.e., a SN II light curve into 3 phases: the shock breakout (SBO), the plateau, and finally the radiative tail.

Apart from the neutrino signal, the first sign of a SN explosion is when the shock wave breaks out of the star and appears as an X-ray flash (Colgate, 1974; Klein & Chevalier, 1978), followed by a UV/optical transient (Falk, 1978). The SBO ($\sim 10^6$ K) lasts from few hours to days depending on the size of the progenitor and the presence or not of a circumstellar medium (Chevalier & Fransson, 2008; Chevalier & Irwin, 2011; Tominaga et al., 2011; Moriya et al., 2015). From this point onwards, the supernova can be considered an expanding and cooling sphere of gas due to the expansion of the ejecta. Its luminosity is determined by the location of the photosphere, which recedes in mass coordinates. After the SBO+cooling, the supernova enters into a phase where the temperature and the luminosity remain fairly constant, this phase is called the plateau phase.

The optically thick phase is physically well-understood and is due to a change in opacity and density in the outermost layers of the SN. At the beginning, the Hydrogen present in the outermost layers of the progenitor star is ionised by the shock wave, which implies an increase of the opacity and the density that prevents the radiation from the inner parts to escape (Top left figure from Figure 1.7). After a few weeks, the star has cooled to the temperature allowing the recombination of ionised Hydrogen, i.e. higher than 5000 K due to the large optical depth (Top right figure from Figure 1.7). The ejecta expands and the photosphere recedes in mass space, releasing the energy stored in the corresponding layers (bottom figure from Figure 1.7). Since the photospheric radius changes only slowly in this phase (10^{15} cm), even if the H recombination front moves inwards in mass coordinates, the luminosity appears constant. As Anderson et al. (2014b) show, this delicate balance between the recession of the photosphere in mass and the radius is rarely observed and there is significant diversity observed in the SNe II light curve morphologies. Once the photosphere has passed through the H-rich ejecta, the plateau ends, the SN is now optically thin, the luminosity drops to the radioactive tail.

The radioactive tail is powered by the radioactive decay ^{56}Co to ^{56}Fe, which itself is the product of radioactive decay 0.1 $M_\odot$ of ^{56}Ni produced in the explosion. The γ-rays are captured and converted to optical photons which can escape freely. For SNe Ibc, due to the lack of Hydrogen envelope, their light curve are essentially powered by the radioactive decay.

1.1.3.4 Spectroscopy

The spectral differences among the CCSNe family are thought to be due to the relative ability of the SN progenitors to retain their outermost envelopes of unprocessed Hydrogen or helium. SNe II have less massive progenitors which keep a significant fraction of

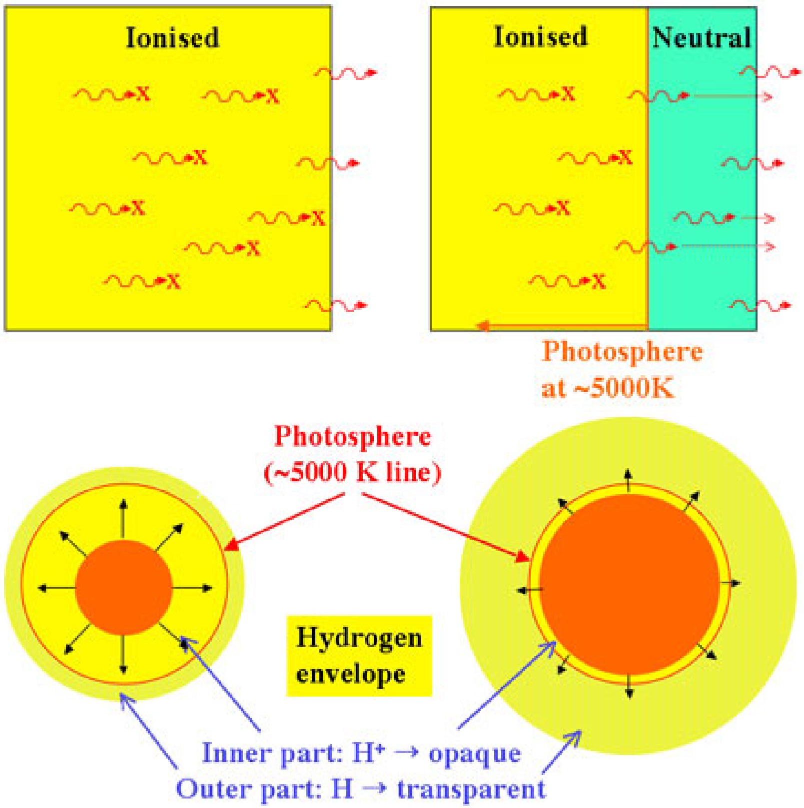

Figure 1.7: *Top*: At the beginning, the Hydrogen envelope is fully ionised and only photons from the outermost regions can escape the supernova (left). Then, when the supernova cools, the Hydrogen recombines to its neutral form and we are able to observe photons from deeper layers in the star (right). *Bottom*: Position of the photosphere. The temperature of recombination is constant, thus the photosphere receeds into the star and a plateau is seen in the light curve. Copyright Swinburne University of Technology.

their unprocessed H layers, unlike SNe Ibc which have more massive progenitors that lose their H due to strong stellar winds or transfer to a binary companion.

At early phases, SNe II spectra exhibit a blue continuum and is dominated by strong P Cygni profiles of Balmer lines (H_α, H_β, H_γ) and He I lines. The P-Cygni profile is characteristic of material in an expanding shell. In Figure 1.8, the P-Cygni profile formation in the SN spectra is explained. The P-Cygni profile shows two components: a redshifted emission (Doppler effect) from the expanding shell moving away from the observer. The ejecta expanding perpendicular to the line-of-sight will not move, and will remain at the same wavelength as the rest wavelength. The second component is a blueshifted absorption feature due to the cooler material between the star and the observer which is expanding towards the observer. In the CCSNe spectra, after the maximum, the continuum becomes redder and new absorption lines appear as: Ca II, Na I, Fe II, Ti II, and Sc II. For example, some useful lines for the photospheric expansion velocity measurements like Fe II $\lambda 5169$ or Fe II $\lambda 5018$ appear $\sim$ 20 days after the explosion. Finally, during the nebular phase, the optical emission is dominated by emission lines formed by recombination or collisional excitation as the forbidden lines: [O I] and [Ca II].

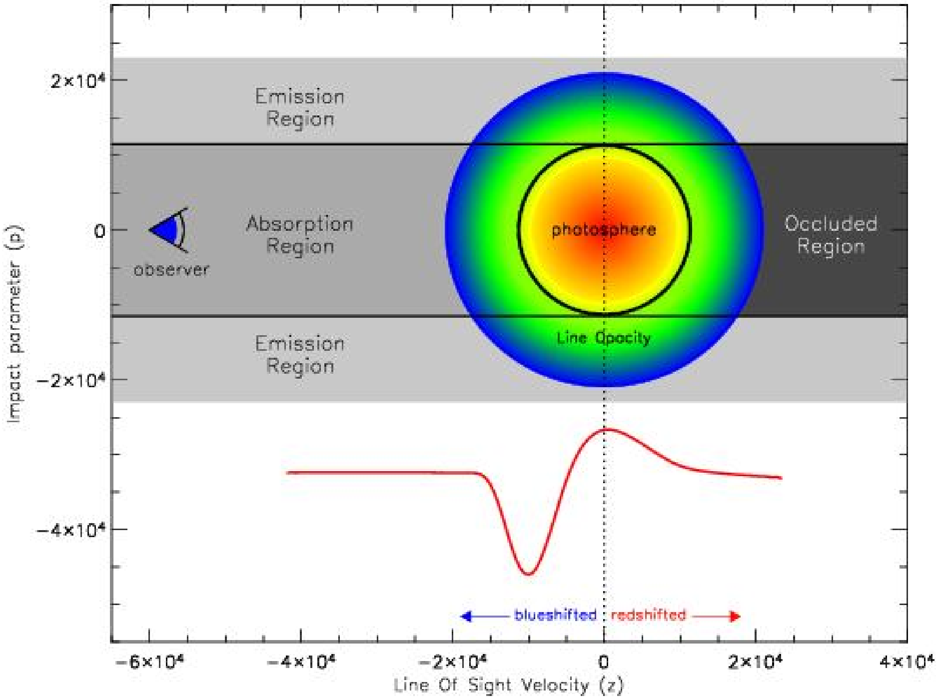

Figure 1.8: A P Cygni profile showing blueshifted absorption trough and doppler broadened emission towards the red. Image from Daniel Kasen, http://supernova.lbl.gov/∼dnkasen/

SNe Ibc spectra show a lack of Hydrogen in their spectra, and SNe Ic do not show any He feature. In both SNe Ib and SNe Ic, strong lines of O I, Ca II are present but also Na I, Fe II, and Ti II (Millard et al., 1999; Branch et al., 2002). As the supernova enters into the nebular phase, oxygen lines start to appear like [O I] $\lambda5577$ and also the weaker [O I] $\lambda\lambda6300, 6364$. Finally, at late time lines of Ca II $\lambda\lambda7291, 7324$ can be seen together with Mg I] $\lambda4571$. In Figure 1.9, I show a summary of the variety in SNe spectra for SNe Ia, SNe II and SNe Ibc for three different epochs: at maximum, 3 weeks after maximum and 1 year after (Turatto et al., 2003).

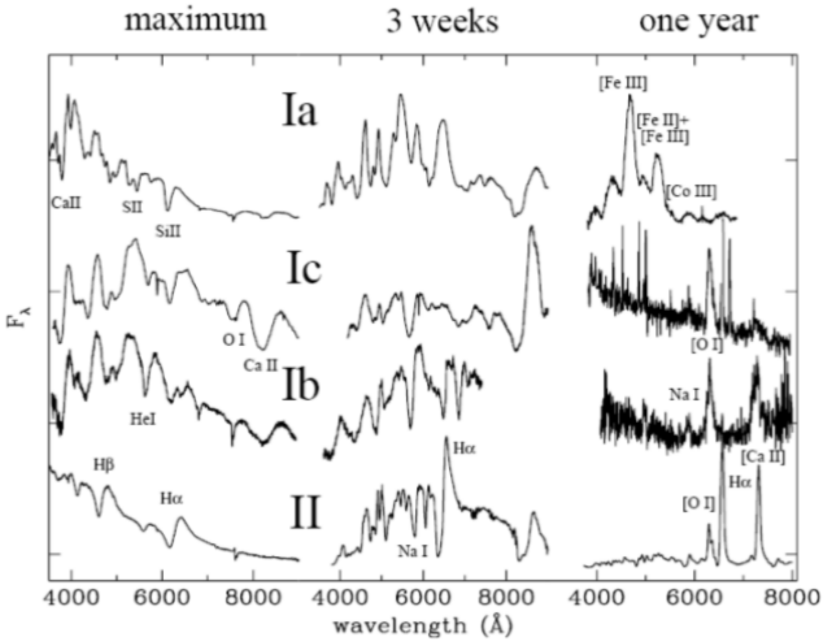

Figure 1.9: Spectra of the most common supernovae types, at maximum light, three weeks later (from maximum light) and one year after maximum light. The spectra are from SN 1996X (SNe Ia), SN 1994I (SNe Ic), SN 1997B (late time Ic spectra), SN 1999dn (for the fist two epochs in the SNe Ib example) and SN 1990I (late time Ib spectra) and from SN 1987A (SNe II). See Turatto et al. (2003).

1.2 Cosmology and supernova

The term cosmology comes from the Greek, kosmos "world", and -logia "study of", whose purpose is to study the evolving Universe as a whole. As we know since Copernicus, the Earth is not in a privileged place in the Universe, thus all lines-of-sight should be equivalent. All the cosmological models are based on this principle: the Universe is *homogeneous* and *isotropic* on larges scales. This cosmological principle was confirmed in 1992 with the COBE satellite (COsmic Background Explorer; Fixsen et al. 1996; Jaffe et al. 2001), then using the WMAP satellite (Wilkinson Microwave Anisotropy Probe; Barnes et al. 2003) in 2003, and finally during the Planck mission in 2013 (Planck Collaboration et al. 2013). These three missions are dedicated to observe the first radiation from the Big Bang called the Cosmological Microwave Background (CMB[4]) discovered by Arno Penzias and Robert Wilson in 1964. As we can see in Figure 1.10, the CMB observed during the Planck mission appears almost uniform in all directions of the sky with only tiny fluctuations in temperature (10^{-5}). Even if these fluctuations are very small, they represent differences in densities of structure and they will be responsible for the large structure formations.

---

[4] The CMB is a thermal radiation ($\sim$ 2.7K) emitted after the recombination (380 000 years after the Big Bang), is the furthest back in time we can explore using light.

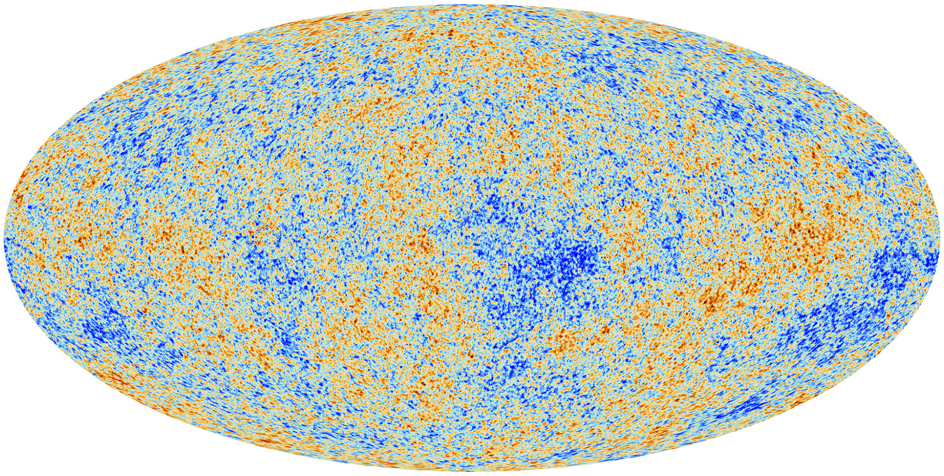

Figure 1.10: The anisotropies of the Cosmic microwave background as observed by Planck. The blue colour represent the coldest of the CMB (Planck Collaboration et al. 2013).

1.2.1 Brief Review of modern cosmology

1.2.1.1 Einstein equation

In 1915, Albert Einstein proposed his revolutionary theory which now is the basis of modern cosmology, general relativity (GR). GR connects the spatial curvature and the energy content and explains how matter/energy determines the curvature of spacetime:

$$R_{\mu\nu} - \frac{1}{2} g_{\mu\nu} R = \frac{8\pi G T_{\mu\nu}}{c^4} + \Lambda g_{\mu\nu} \tag{1.1}$$

where $R_{\mu\nu}$ is the Ricci curvature tensor, R is the scalar curvature, $g_{\mu\nu}$ is the metric tensor, G is Newton's gravitational constant, c is the speed of light in vacuum, and $T_{\mu\nu}$ is the stress-energy tensor. The left-hand side represents the curvature of spacetime as determined by the metric and the right-hand side the matter/energy content of spacetime. Note that this equation includes the extra term $\Lambda g_{\mu\nu}$, called the cosmological constant, introduced by Einstein in 1917 to force the equations to predict a stationary Universe.

1.2.1.2 Friedmann-Lemaître equation

Our Universe is homogeneous and isotropic, so we use the Friedman-Lemaître-Robertson-Walker metric to describe its geometry:

$$ds^2 = -c^2dt^2 + a^2(t)[\frac{dr^2}{1-kr^2} + r^2(d\theta^2 + sin^2\theta d\phi^2)] \tag{1.2}$$

where r, θ, and ϕ are the comoving coordinates, a(t) is the scale factor and k indicates the curvature 0, -1, or $+1$ for a flat, closed, or open Universe, respectively. Using this metric and assuming that the energy content of the Universe acts as a perfect fluid on cosmological scales, we can derive solutions for equation (1.1) and we find a relation between the scale factor, the space curvature, the energy density ρ (the sum of matter, radiation, dark energy) and the pressure p (the sum of the pressures of each component) :

$$H^2 = \left(\frac{\dot{a}}{a}\right)^2 = \frac{8\pi G\rho}{3} - \frac{k}{a^2} + \frac{\Lambda}{3} \tag{1.3a}$$

$$\frac{\ddot{a}}{a} = -\frac{4\pi G}{3}(\rho + 3p) \tag{1.3b}$$

where ρ and p are related through the equation-of-state (EOS), $p = \omega\ \rho$ where ω is a dimensionless number. After the initial big bang, the energy content of the universe was dominated by relativistic particles ($\omega = 1/3$), which were eventually surpassed by non-relativistic matter (ω=0). For ω=-1, the energy will be dominated by the cosmological constant. If we divide equation (1.3a) by H^2 we can define a new equation and four cosmological parameters including the Hubble constant: Ω_M, Ω_Λ, Ω_k, and Ω_R:

$$1 = \Omega_M + \Omega_\Lambda + \Omega_k + \Omega_R \tag{1.4}$$

$$\begin{aligned} \Omega_M &= \frac{8\pi G}{3H_0^2}\rho_{M_0} \\ \Omega_\Lambda &= \frac{\Lambda}{3H_0^2} \\ \Omega_k &= \frac{-k}{a^2H_0^2} \\ \Omega_R &= \frac{8\pi G}{3H_0^2}\rho_{R_0} \end{aligned} \tag{1.5}$$

where Ω_M, Ω_Λ, Ω_k, and Ω_R are the density matter, the dark energy matter, the curvature, and radiation density respectively. The goals of observational cosmology are to derive these parameters and understand the Universe evolution. For example, the CMB measurement constrains the curvature of the Universe to be zero (Planck Collaboration et al., 2015). We know also that the radiation density is currently very small and can be neglected (Planck Collaboration et al., 2015).

1.2.1.3 Cosmological distances

Here we will define all the different cosmological distances as it was defined in Hogg (1999). The first cosmological distance that we can define is the Hubble distance. The Hubble distance is defined as

$$d_H = \frac{c}{H_0} \tag{1.6}$$

where c is the speed of light in km s^{-1}, and H_0 the current Hubble constant in km s^{-1} Mpc^{-1}. If we take the value of 69 km s^{-1} Mpc^{-1} found by the Planck Collaboration et al. (2015), the Hubble distance is 4.4 GMpc.

The proper distance can be defined as the distance between two points if we freeze the Universe. This distance depends on the Universe evolution, indeed for our Universe in expansion, the proper distances were smaller in the past. Related to this distance, we define the comoving distance. The comoving distance does not evolve with time due to the expansion of space and can be defined as the proper distance between two points measured along a path defined at the present cosmological time.

$$d_C = d_H \int_0^z \frac{dz'}{\sqrt{\Omega_M(1+z')^3 + \Omega_k(1+z')^2 + \Omega_\Lambda(1+z')^{3(1+\omega)}}} \tag{1.7}$$

We can also define an angular distance which is very useful in gravitational lensing and for the baryonic acoustic oscillation measurements,

$$d_A = \frac{d_M}{(1+z)} \tag{1.8}$$

where the d_M transverse comoving distance is equal to the comoving distance for a flat Universe. In a flat Universe in expansion, the objects appear bigger than they really are.

Finally we can define the luminosity distance d_L, which is the key distance for SNe cosmology and is used through this thesis. The flux density f of the light emitted isotropically from an object, and passing through a spherical surface is $f = P/A$ where P is the total power of the light, i.e., the amount of energy emitted per unit time and A the proper area. The proper area can be defined as $A = 4\pi d_p^2$ where d_p is the proper distance today. For a total power L emitted by the source we obtain:

$$f = \frac{P}{A} = \frac{L}{4\pi d_p^2}. \tag{1.9}$$

This is the case only in a static Universe. Due to the expansion of the Universe, the power of the light is reduced by a factor (1+z)^2. One (1+z) factor is due to the fact that photons received which lose energy as their wavelengths are redshifted (E=hc/λ) and the second factor is due to the relativistic time dilation in the photon emission rate since the source is moving away from us. The total flux at reception will be reduced by the two factors of (1+z), so we have:

$$f = \frac{L}{4\pi d_p^2 (1+z)^2} = \frac{L}{4\pi d_L^2}, \tag{1.10}$$

where d$_L$=(1+z)d$_p$. Finally, we can rewrite the luminosity distance as function of the cosmological parameters using equation (1.7):

$$d_L = \frac{c(1+z)}{H_0} \int_0^z \frac{dz'}{\sqrt{\Omega_M(1+z')^3 + \Omega_k(1+z')^2 + \Omega_\Lambda(1+z')^{3(1+\omega)}}} \tag{1.11}$$

Figure 1.11, taken from Sahni & Starobinsky (2000), shows the evolution of the luminosity distance versus redshift (Hubble diagram) for different cosmological models (flat Universe). From this Hubble diagram, it is clear that the determination of the cosmological parameters from standard candles requires objects at low and high redshifts. Indeed at low redshifts, the luminosity distance is independent of the cosmological model, the local geometry is very close to being Euclidean, and thus the effects of the global curvature can be safely ignored. The slope determines the current normalised expansion rate, i.e., the Hubble constant ($d_L = vH_0^{-1}$, with v the recession velocity). The sample of objects at higher redshifts is very useful to determine the cosmological parameters. For higher redshifts, the shape of the Hubble diagram does not depend on the absolute value of the luminosities (independent of the Hubble constant), so the curvature reflects directly the global kinematics of the Universe and the cosmological parameters (Ω_M, Ω_Λ, Ω_k) can be determined. For example, if at a given time you find SNe with higher redshift than expected from the current expansion rate, that would imply that the expansion was faster in the past and has been slowing down. As described in Section 1.2.2, Riess et al. (1998); Perlmutter et al. (1999); Schmidt et al. (1998) found that distant SNe Ia are fainter than expected from their redshift, i.e., they are farther away than one would expect, thus the expansion is accelerating.

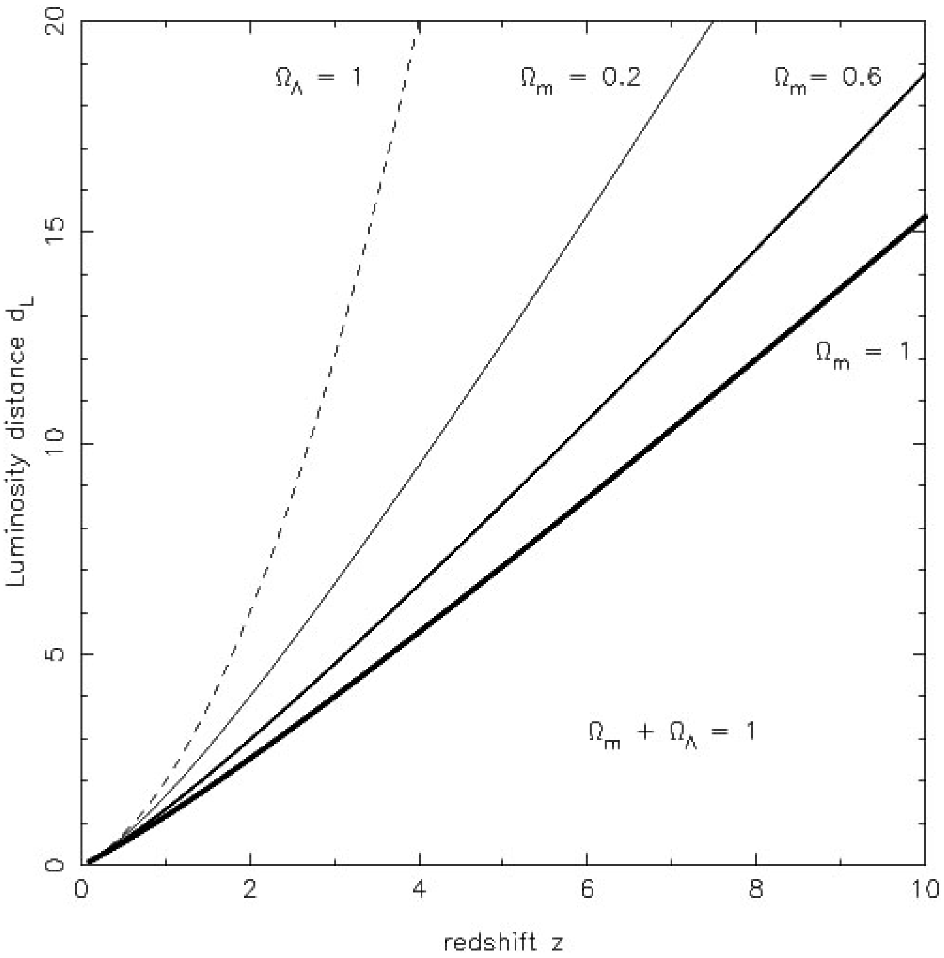

Figure 1.11: The luminosity distance versus redshift for different flat cosmological models. The dashed line represents a de Sitter model, i.e., a Universe without matter. The bold line represents a Universe without dark energy (Einstein-de Sitter model) and the two others line a mix of dark energy and dark matter (Sahni & Starobinsky, 2000).

1.2.1.4 Universe in expansion

The greatest astronomical discoveries of the 20th century was claimed by Edwin Hubble in 1929 (Hubble, 1929). For his discovery, Hubble used two important tools, distances and velocities.
For this purpose, to measure distances, Hubble used Cepheid stars. A Cepheid star's period is directly related to its intrinsic luminosity (Leavitt, 1908; Benedict et al., 2007) and allows one to probe the Universe to 15 Mpc. Hubble succeeded to measure distances to 18 galaxies.

Obtaining velocities of these galaxies was very difficult and was done by Vesto Slipher (Slipher, 1917). Few years before, in 1912 Slipher (Slipher, 1912) after obtaining a galaxy spectrum, found that some absorption lines were shifted with respect to their theoretical wavelength. He suggested that it was due to the motion of the galaxy and thus, its velocity. When a galaxy moves away, the wavelength will be shifted to the red part of the spectrum. As the Universe expands, this wavelength will be shifted by the same factor as the Universe, and we can define the redshift as (relativistic case):

$$1 + z = \frac{\lambda_0}{\lambda_e} = \frac{a(t_0)}{a(t_e)} = \frac{v}{c} \tag{1.12}$$

where z is the redshift, λ_e and λ_0 are the emitted and observed wavelengths respectively, and a(t) is the scale factor of the expanding universe as defined previously.

Using the distances measured by himself and the velocities from Slipher (not cited by Hubble in his famous paper !!!), Hubble found a linear relation between distance and recession velocity, where more distant galaxies are receding faster. This was the first observational proof of the expansion of the Universe. The famous Hubble law can be written as:

$$v = H_0 \times d_L \tag{1.13}$$

where v is the recession velocity in km s^{-1}, H$_0$ the Hubble constant in km s^{-1} Mpc^{-1} and d_L the luminous distance in Mpc. In Figure 1.12 we show the original plot, for which Hubble found an expansion rate of 500 km s^{-1} Mpc^{-1}. The current value is 67.8 ± 0.9 km s^{-1} Mpc^{-1} (Planck Collaboration et al. 2015). For completeness about the expansion discovery it is very important to point out that two years before Hubble's observations, Georges Lemaître published in a Belgium review a paper titled "Un Univers homogène de masse constante et de rayon croissant rendant compte de la vitesse radiale des nébuleuses extra-galactiques" (A homogeneous Universe with constant mass and increasing radius to explain the radial velocities from the nebulae). In his theoretical paper, Lemaître used the velocities measured by Slipher and concluded that the velocities are due to an expanding Universe. He derived a rate of expansion similar to what Hubble would publish two years later (600 km s^{-1} Mpc^{-1}).

1.2.2 SNe Ia and cosmology

To reach larger distances one needs brighter objects. In 1939, Wilson (1939) and Zwicky (1939) suggested that due to their brightness, SNe could be useful tools to measure distances at higher redshifts. Unfortunately, SNe Ia are not perfect standard candles. As it was shown in Figure 1.3, SNe Ia have dispersion at peak magnitude of 1.1 mag. Fortunately, as it was also shown in this figure, the luminosity at peak is directly related to the light-curve shape, i.e., SNe Ia are standardisable (Phillips, 1993; Hamuy et al., 1996). A second parameter was found to correlate with the luminosity, the colours. Redder SNe Ia are fainter (Riess et al., 1996; Tripp, 1998), so we can

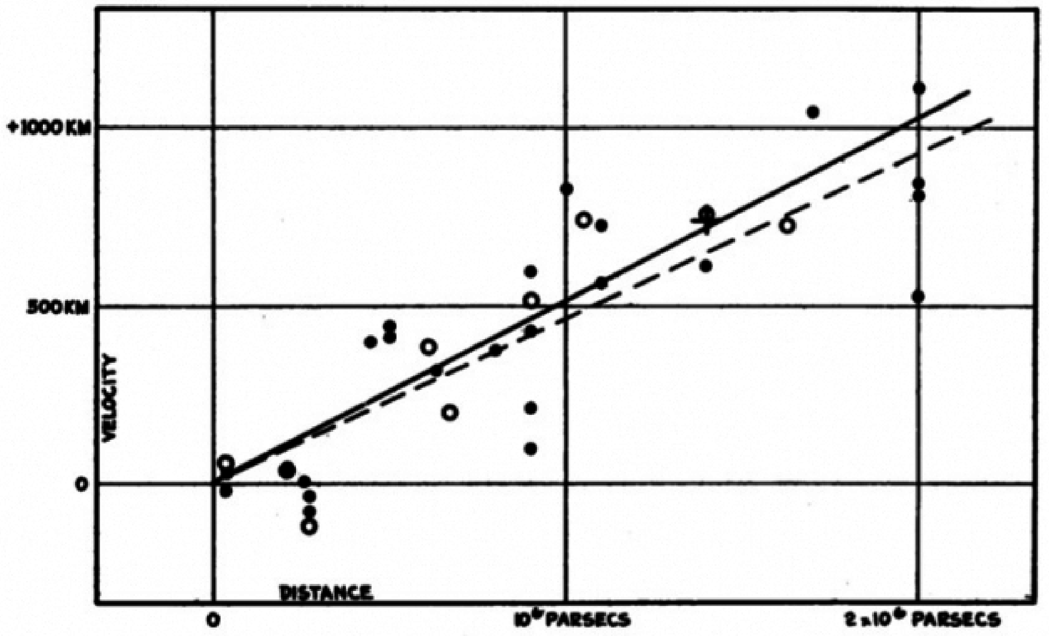

FIGURE 1

Velocity-Distance Relation among Extra-Galactic Nebulae.

Figure 1.12: Edwin Hubble's plot of the Velocity-Distance relationship for galaxies (Hubble, 1929).

correct the apparent magnitude by these two factors and reduce the dispersion in their peak magnitude. The standardisation of SNe Ia allows us to reach a dispersion of only 0.15–0.2 mag in the Hubble diagram (Phillips, 1993; Hamuy et al., 1996; Riess et al., 1996). In Figure 1.13 we show the same light-curves shown in Figure 1.3 but this time after applying a timescale stretch correction (Perlmutter et al., 1997). The stretch correction is one method (the others are the $\Delta_{m_{15}}$ method: Hamuy et al. 1996; Phillips et al. 1999, and the multi-light curve shape correction: Riess et al. 1996) to standardise the SNe Ia. The stretch correction consists in stretching the time evolution of the light-curve with a factor, s. If $s \geq 1$ the light-curve is brighter, else the light-curve is fainter. With this stretch correction, all the observed curves converge to the template curve with very little scatter.

The use of SNe Ia as standard candles led to the measurement of the expansion history of the Universe and showed that, contrary to expectations, the Universe is undergoing an accelerated expansion (Riess et al., 1998; Perlmutter et al., 1999; Schmidt et al., 1998). In Figure 1.14, the Hubble diagram plotted by the Supernovae Cosmology Project (SCP) team (Perlmutter et al., 1999) is presented. In this plot, the authors used 42 high redshift supernovae and 18 low redshift supernovae from the Calán-Tololo (Hamuy et al., 1996) and we clearly see that the supernovae are situated on the top of this diagram, supporting the existence of dark energy. For this first proof of the

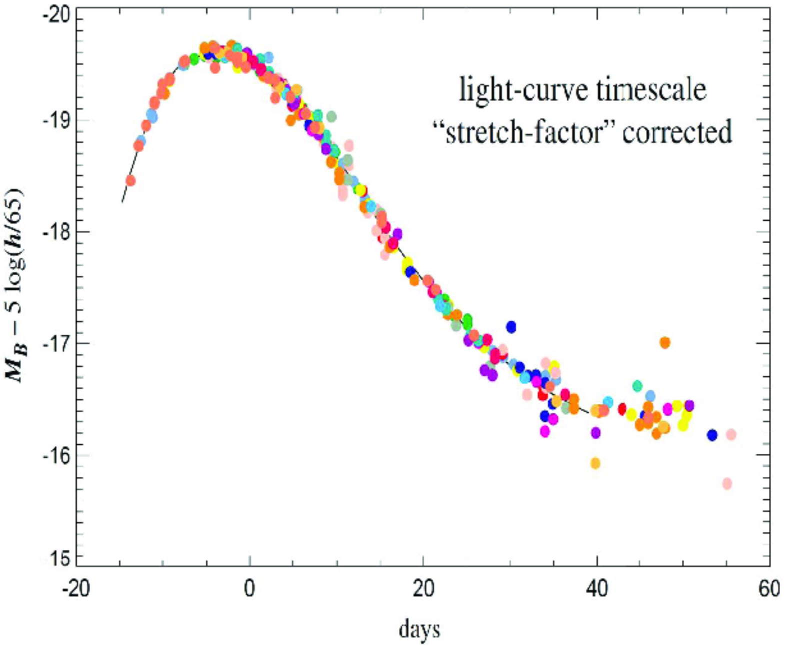

Figure 1.13: The light-curve for different SNe Ia from Calán-Tololo project (Hamuy et al., 1996) after correction using the stretch factor method (Kim et al., 1997).

accelerating expansion of our Universe, the total sample was very small (high statistical uncertainties) and also the systematic uncertainties due to the combination of two different samples (Calán-Tololo and SCP) were dominant. To date, the statistical errors are smaller due to the greater numbers of SNe Ia observed and are comparable to the systematical errors. Thanks to an important effort to obtain observed light-curves in the same and well understood photometric system, different surveys such as the Carnegie Supernova Project, the Sloan Digital Survey-II, and the Supernova Legacy Survey (Hamuy et al., 2006; Frieman et al., 2008a; Astier et al., 2006) were created, and the systematic errors have been reduced considerably. In Figure 1.15 we show a complete Hubble diagram for SNe Ia. Betoule et al. (2014) used more than 740 SNe Ia, and obtained a dispersion in the Hubble diagram of around 0.15 mag, which allowed them to derive very precise cosmological parameters using a combination of SNe Ia, the CMB and the BAO[5]. They found Ω_M=0.295 ± 0.034 (stat+sys) and ω=-1.018 ± 0.057 (stat+sys).

---

[5] BAO are periodic fluctuations due to the fight between pressure and gravitation in the primordial plasma. They provide a "standard ruler" for length scale in cosmology (∼ 490 million light years in today's universe)

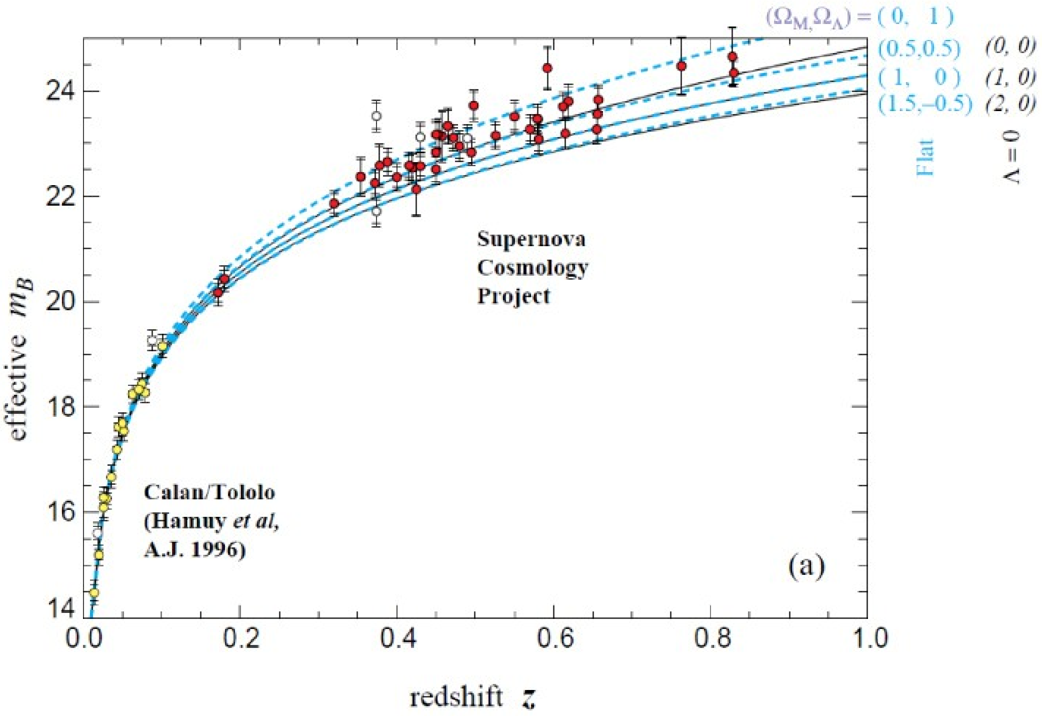

Figure 1.14: Hubble diagram. The yellow symbols represented the low redshift sample and the red dots the SNe Ia from the Supernova Cosmology Project. The dashed curves are for a range of flat cosmological models: $(\Omega_M, \Omega_{Lambda})$ = (0,1) on top, (0.5,0.5) third from bottom, (0.75,0.25) second from bottom, and (1,0) is the solid curve on bottom. The middle solid curve is for $(\Omega_M, \Omega_{Lambda}) =$ (0,0). See Perlmutter et al. (1999)

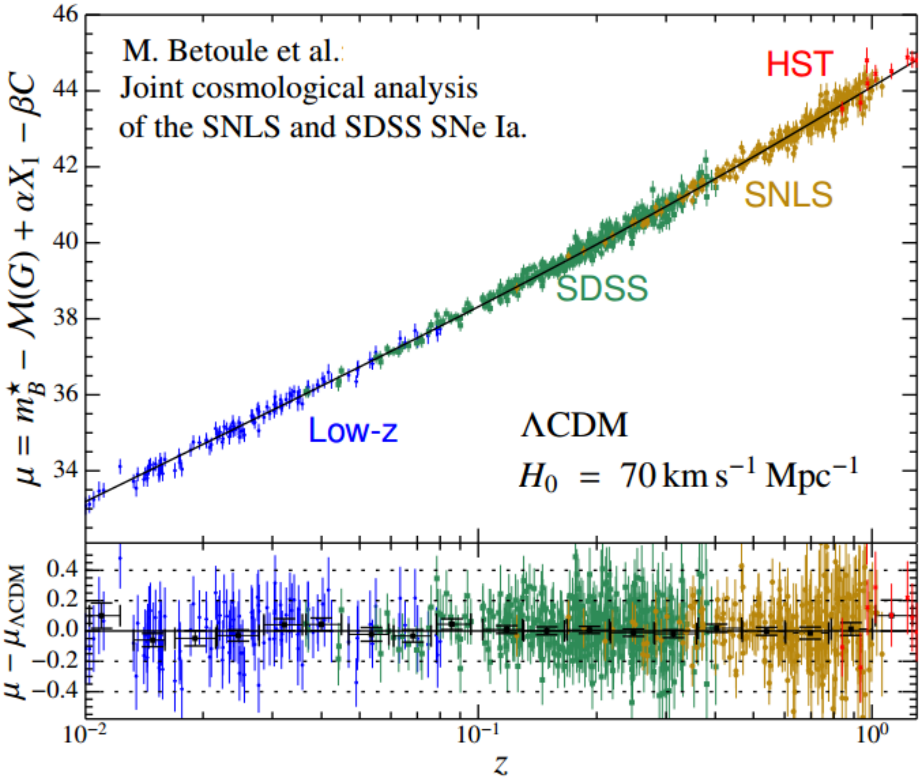

Figure 1.15: Hubble diagram of the combined sample (lower and higher redshifts). The distance modulus redshift relation of the best-fit ΛCDM cosmology for a fixed H_0=70 km s^{-1} Mpc^{-1} is shown as the black line (Betoule et al., 2014).

1.2.3 Actual picture of our Universe

In Figure 1.16 we see our current picture of our Universe (Planck Collaboration et al., 2015). It is composed of only 0.01% of radiation, 4.9% of baryonic matter (atoms, galaxies, gas, dust), i.e., only 1 proton per meter cubic, 25.8 % of cold dark matter, and 69.3 % of dark energy. Around 95% of the total energy density in the Universe is in a form that we cannot see directly.

Dark matter is suspected to be constituted by weakly interacting massive particles (WIMPs) that interact only through gravity and the weak force. First suspected by Zwicky (1933) in 1933, due to the difference between the gravitational mass of the galaxies within galaxy clusters and the mass excepted from the luminosity (400 times smaller than the gravitational), the dark matter was then confirmed in 1980 by Rubin et al. (1980) from the rotation curves of galaxies.

Dark energy was discovered from the SNe Ia and then confirmed by different experiments (CMB, baryon acoustic oscillation measurements (Blake & Glazebrook 2003; Seo & Eisenstein 2003) but its nature remains uncertain. Two forms have been proposed for the dark energy, the cosmological constant or a scalar field. The main difference between both models is that for the scalar fields model (or quintessence, Caldwell et al. 1998) the dark energy changes over time. The last cosmological observations favour the cosmological constant model, with $\omega \sim -1$ (Betoule et al., 2014; Planck Collaboration et al., 2015) but some questions remains about the nature of this cosmological constant. Indeed, the cosmological constant could be attributed to the vacuum energy density, but the difference between the energy density predicted and the observed are enormous; 120-orders-of-magnitude discrepancy.

Now that we know the current composition of our Universe, it is very interesting to look at its evolution. In Figure 1.17, from Frieman et al. (2008b) we can see the evolution in time of the radiation, matter and dark energy densities. The Universe evolution can be separated into three distinct phases: the radiation-dominated until $z \sim 3000$, the matter-dominated from $z \sim 3000$ to $z \sim 0.5$ with a deceleration of the expansion, and the present time, the dark energy dominated with a Universe in an accelerated expansion. When the Universe is dominated by radiation, the energy density scales as $a(t)^{-4}$, $a(t)^{-3}$ due to the expansion of the Universe ($a(t)$ increases in the three direction) and $a(t)^{-1}$ because photon energies scale like the inverse of their wavelength. For the Universe during the matter-dominated area, the energy density simply scales as $a(t)^{-3}$, and for our actual Universe, dominated by the cosmological constant, the energy density is constant.

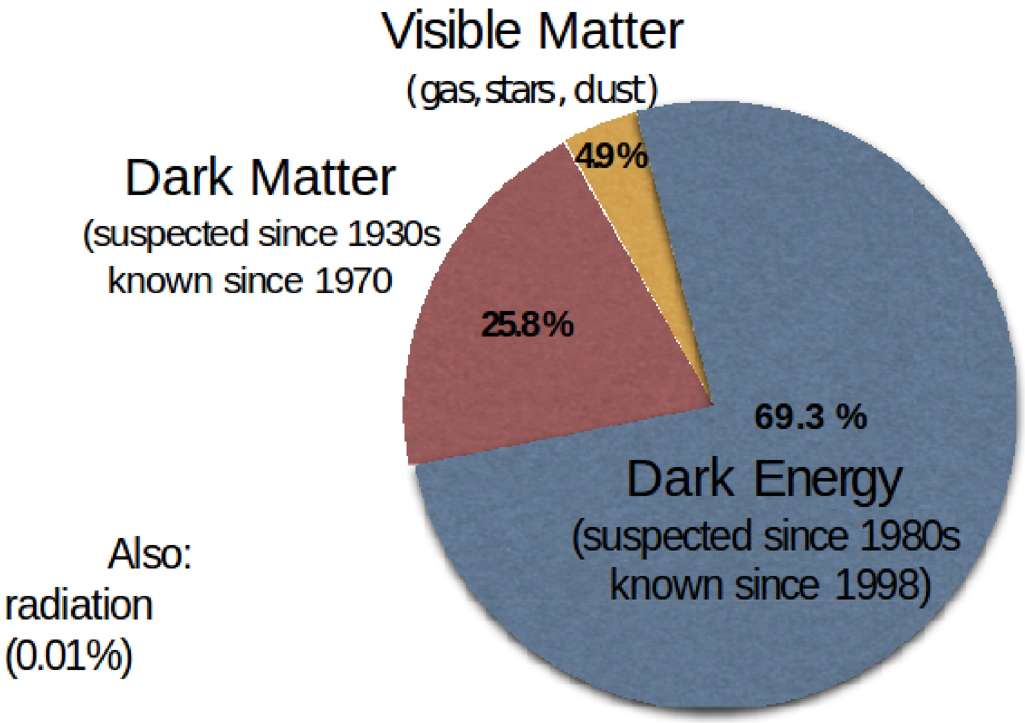

Figure 1.16: The proportion of the different components of the Universe: Baryonic matter, dark matter, and dark energy (Planck Collaboration et al., 2015).

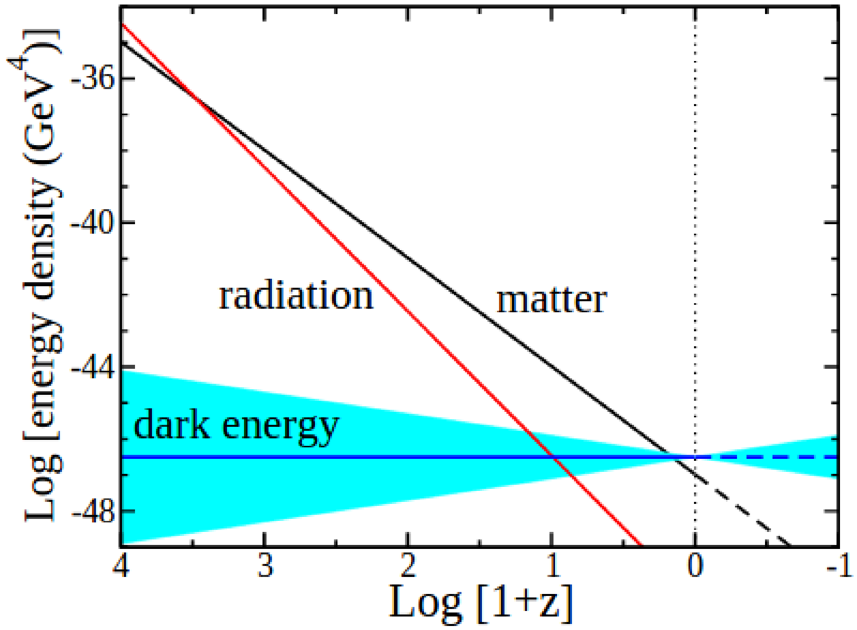

Figure 1.17: Evolution of radiation, matter, and dark energy densities with redshift. For dark energy, the band represents $\omega = -1 \pm 0.2$ (Frieman et al., 2008b).

1.2.4 SNe II and cosmology

While SNe Ia have been used as the primary diagnostic in constraining cosmological parameters, type IIP supernovae have also been established to be useful independent distance indicators. SNe IIP are 1–2 mags less luminous than SNe Ia however, their intrinsic rate is higher than SNe Ia (Li et al., 2011), and additionally the rate peaks at higher redshifts than SNe Ia (Taylor et al., 2014), which motivates their use as cosmological probes (see Hamuy & Pinto 2002). Also the fact that in principle their physics and their progenitors are better understood (see Section 1.1.3.2) than those of SNe Ia, further encourages investigations in this direction.

To date, several methods have been developed to standardise SNe II. The first method called the "Expanding Photosphere Method" (EPM) was developed by Kirshner & Kwan (1974) and allows one to obtain the intrinsic luminosity assuming that SNe II radiate as dilute blackbodies, and that the SN freely expands with spherical symmetry. The EPM was implemented for the first time on a large number of objects by Schmidt et al. (1994) and followed by many studies (Hamuy et al., 2001; Dessart & Hillier, 2005, 2006; Jones et al., 2009; Emilio Enriquez et al., 2011). One of the biggest issues with this method is that the EPM only works if one corrects for the blackbody assumption which requires correction factors computed from model atmospheres (Eastman et al. 1996; Dessart & Hillier 2005 and see Dessart & Hillier 2006 for the resolution of the EPM-based distance problem to SN 1999em). Also to avoid the problem in the estimate of the dilution factor, Baron et al. (2004) proposed a distance correcting factor that takes into account the departure of the SN atmosphere from a perfect blackbody, the "Spectral-fitting Expanding Atmosphere Method" (SEAM, updated in Dessart et al. 2008). This method consists of fitting the observed spectrum using an accurate synthetic spectrum of SNe II, and then since the spectral energy distribution is completely known from the calculated synthetic spectra, one may calculate the absolute magnitude in any band.

A simpler method, also based on photometric and spectroscopic parameters, the "Standardised Candle Method" (SCM) was first introduced by Hamuy & Pinto (2002). They found that the luminosity and the expansion velocity are correlated when the SN is in its plateau phase (50 days post-explosion). In Figure 1.18, we show the original correlation found by Hamuy & Pinto (2002) between the expansion velocity and the luminosity. Thanks to this method the scatter in the Hubble diagram drops from 0.8 mag to 0.29 mag in the I-band. This relation is physically well understood: for a more luminous SN, the Hydrogen recombination front will be at a larger radius thereby the velocity of the photosphere will be greater for a given post-explosion time (Kasen & Woosley, 2009). In Figure 1.19, we show the theoretical correlation found by the authors using different progenitors (mass, nickel mass, energy, metallicity) together with observational values found by Hamuy (2003). As we can see the theoretical predictions fit perfectly the observed data and the dispersion (0.27 mag) in the relation are only due to variations in the progenitor mass and metallicity for a given explosion energy.

Nugent et al. (2006) improved the SCM by adding a host galaxy extinction correction term based on the $(V - I)$ colour at day 50 after maximum. This new method is very powerful and many other studies (Nugent et al., 2006; Poznanski et al., 2009; Olivares et al., 2010; D'Andrea et al., 2010) have confirmed the possibility to use SNe II as standard candles finding a scatter between 0.25-0.3 mag. In Figure 1.20 we show the most complete Hubble diagram using SNe II and the SCM. For this Hubble diagram Poznanski et al. (2010) used 49 SNe II and they found a dispersion in the Hubble diagram of 0.25 mag. Recently, Maguire et al. (2010) suggested that using near-infrared (NIR) filters, and the SCM, the dispersion can drop to a level of 0.1–0.15 mag (using only 12 SNe IIP). Indeed, in the NIR the host-galaxy extinction is less important, thus, there may be less scatter in magnitude. Note also the work by Rodríguez et al. (2014) where the authors used the Photospheric Magnitude Method (PMM) which corresponds to a generalisation of the SCM for various epochs throughout the photospheric phase and found a dispersion of 0.12 mag using 13 SNe.

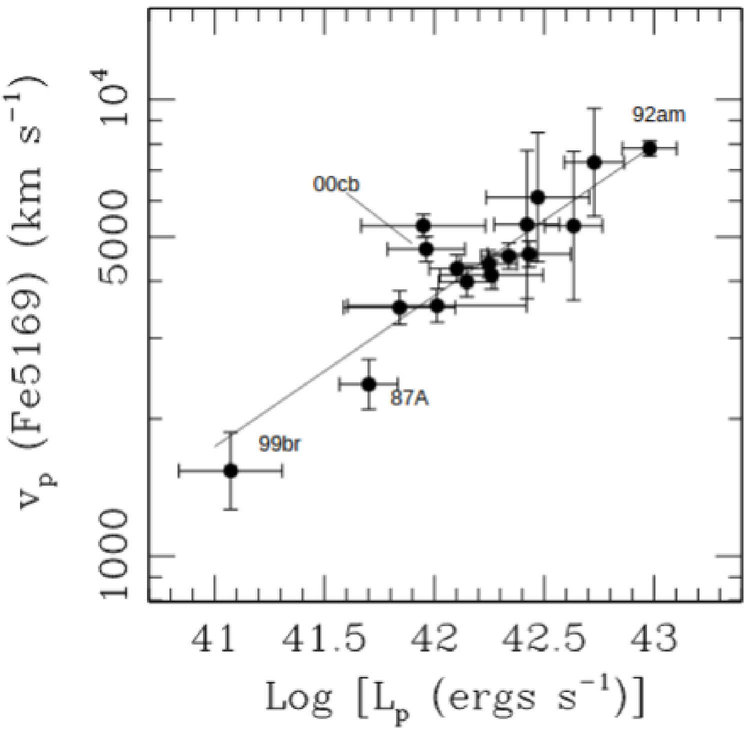

Figure 1.18: Expansion velocities from Fe II λ5169 versus bolometric luminosity, both measured in the middle of the plateau (day 50). The line is a weighted fit, and the relation between the two quantities is: v$_p \sim$ L$^{0.33}$ (Hamuy & Pinto, 2002).

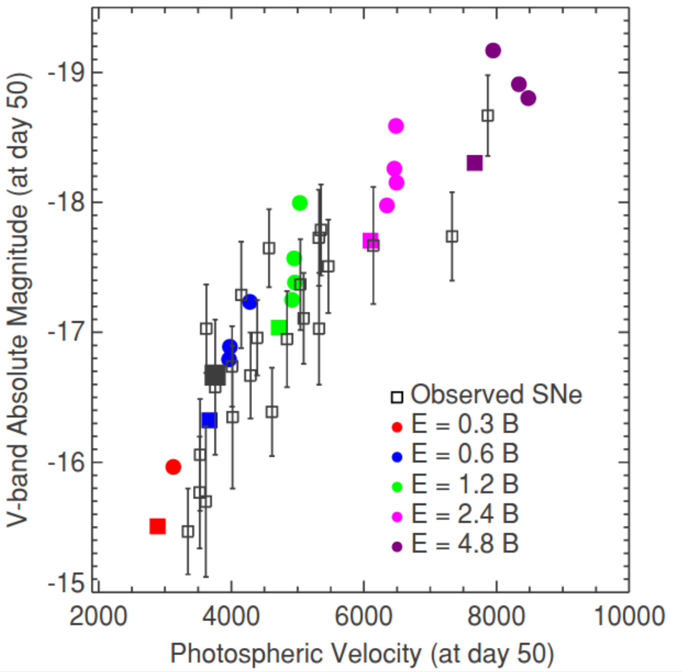

Figure 1.19: Comparison of the model relation from Kasen & Woosley (2009) represented by the circles/squares with the observation sample in open squares compiled by Hamuy (2003). The different colours for the models represent different energy. Circles represent the model with a solar metallicity and squares 0.1 solar models. Note that for each colour the upper circles represent progenitor with higher mass.

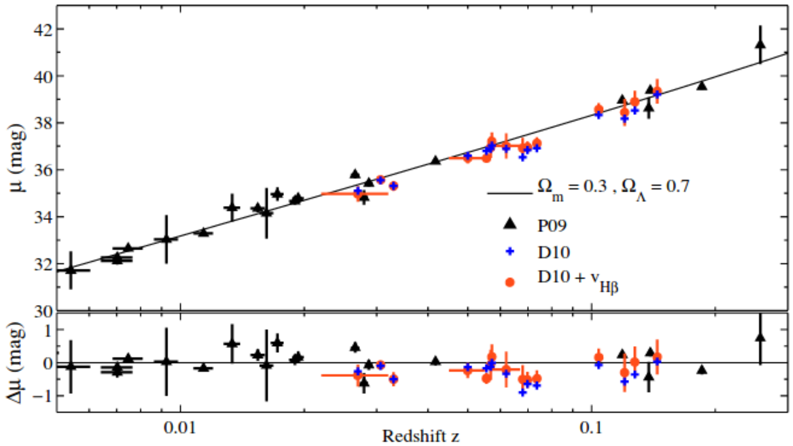

Figure 1.20: Hubble diagram from Poznanski et al. (2010). Top figure represents the Hubble diagram and the bottom shows the residuals from the standard concordance cosmological model. Blue colour is the value found by D'Andrea et al. (2010) for the SDSS sample, red for the same sample revisted by Poznanski et al. (2010). Black colour shows the Poznanski et al. (2009) sample (black triangles). For clarity, we show here only the sample of 36 SNe II at redshifts z > 0.005, where peculiar-velocity uncertainties are less dominant.

1.3 Goals of this dissertation

SNe Ia cosmology has reached a mature state in which cosmological parameters have statistical errors comparable to systematic errors (Conley et al., 2011; Rest et al., 2014; Betoule et al., 2014) and further improvement to constrain the unknown nature of the dark energy is not just a matter of improving the quantity of measurement but also, the quality. Thus, it is important to develop as many independent methods as possible, since the truth will likely emerge from the combination of different independent approaches as we can see in Figure 1.21 where the (Ω_m, ω) plane is plotted using three different methods: SNe Ia, the Cosmic Microwave Background radiation measurements (Wilkinson Microwave Anisotropy Probe, Spergel et al. 2007; Bennett et al. 2003; Dunkley et al. 2009; Komatsu et al. 2011; and more recently the Planck mission, Planck Collaboration et al. 2013 and the Baryon Acoustic Oscillation measurements (Blake & Glazebrook 2003; Seo & Eisenstein 2003; Percival et al. 2010).
The main purpose of this work is to use Type II SNe as distance indicators and derive the cosmological parameters independently. For this, I develop a new method to obtain purely photometric distances using my low redshift supernovae sample (Carnegie Supernova Project). I standardise SNe II using solely light curve and colour-curve parameters, unlike other methods (SCM) which require spectroscopic parameters. Purely photometric methods will be an asset for the next generation of surveys such as the large synoptic survey telescope (LSST; Ivezić et al. 2009). These surveys will discover such a large number of SNe (10^5 core-collapse supernovae per year; Lien et al. 2011) that spectroscopic follow-up will be impossible for all but only for a small number of events. Afterwards, I use two high redshift supernovae samples (Sloan Digital Sky Survey-II and Supernova Legacy Survey) to derive the Hubble diagram and the cosmological parameters. To finish, I apply the SCM to all my supernovae sample, to compare with the purely photometric method.

In summary, I present in Chapter 2 a description of the data set, then in Chapter 3, I explain my procedure to correct apparent magnitudes for Milky Way extinction, S-correction (Stritzinger et al., 2002) and K-correction (Hubble, 1936). In Chapter 4, I describe a new method to standardise the SNe II, using only photometric input, the photometric colour method (PCM) and build a Hubble diagram from z=0.01 to 0.5. In Chapter 5, I use the SCM to derive distances and build a Hubble diagram between z=0.01-0.2. I discuss my results in Chapter 6 and conclude with a summary in Chapter 7.

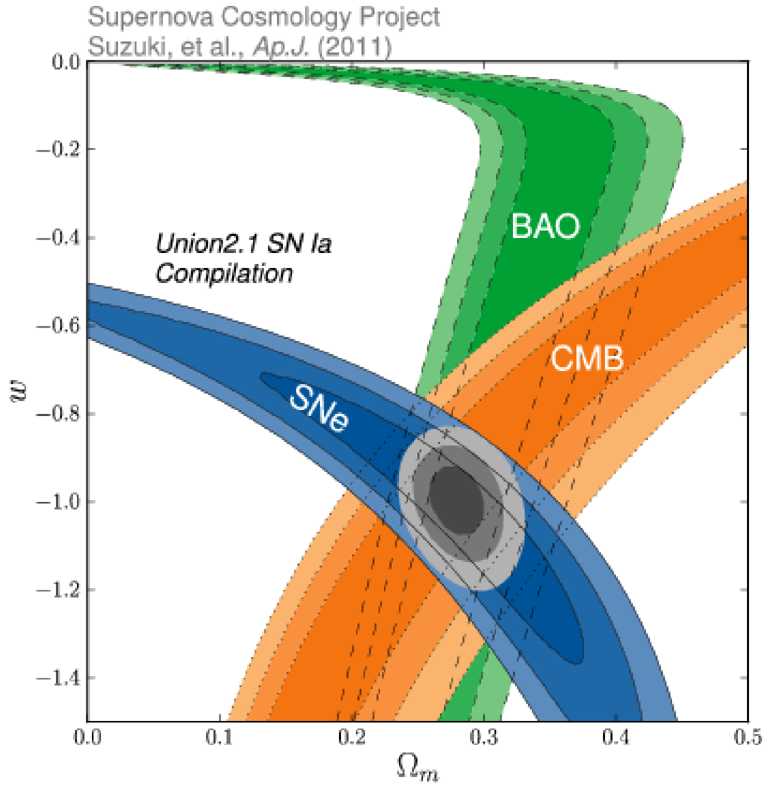

Figure 1.21: ωCDM model: 68.3%, 95.4%, and 99.7 % confidence regions in the (Ω_m, ω) plane from SNe Ia, BAO, and CMB. The SNe Ia confidence region includes statistical uncertainties only.

Chapter 2

Observations and Supernovae sample

Contents

2.1 Carnegie Supernova Project (CSP)

The *Carnegie Supernova Project*[1] (CSP, Hamuy et al. 2006) provided all the photometric and spectroscopic data for the low redshift sample ($z \leq 0.04$). The goal of the CSP was to establish a high-cadence data set of optical and near-infrared (NIR) light-curves in a well-defined and well-understood photometric system and obtain optical spectra for these same SNe. This could be done thanks to guaranteed access to 300 nights per year on the Swope 1-m and the du Pont 2.5-m telescopes at the Las Campanas Observatory (LCO) both equipped with high-performance CCD and IR cameras. Between 2004 and 2009, the CSP observed many low redshift SNe II ($N_{SNeII} \sim 70$), and from this sample more than 50 SNe had both optical and NIR light-curves; one of the largest NIR data samples. Note that from all the SNe II sample, two SN 1987A-like events were removed (SN 2006V and SN 2006au see Taddia et al. 2012). All the CSP SNe II are listed in Table 2.1 and those with NIR data have a note mark. Note that we do not include SNe IIb or SNe IIn. From the CSP sample, I removed six outliers: two SNe (SN 2004ej, SN 2008K) for which I had problems to compute the AKS corrections (in particular with the warping function, see Chapter 3), one because we do not have

---

[1] `http://csp.obs.carnegiescience.edu/`

a clear explosion date (SN 2005hd), another due to its particular characteristics like clear signs of interaction with the circumstellar medium (SN 2007X). I removed also SN 2008bp which is identified as an outlier by Anderson et al. (2014b), and finally, SN 2009au was classified at the beginning as a SNe IIn showing strong interaction (Rodriguez et al. in prep.) The final CSP sample is composed of 61 SNe II for which 50 SNe II have optical and near-infrared photometry.

2.1.1 Data reductions

2.1.1.1 Photometry

All the photometric observations were taken at the Las Campanas Observatory (LCO) with the Henrietta Swope 1-m and the Irénée du Pont 2.5-m telescopes using optical (u, g, r, i, B, and V), and NIR filters (Y, J, and H, see Stritzinger et al. 2011). For this work, all the data were reduced by the CSP members and I only needed to reduce 15 SNe II NIR photometry, that is why I will solely explain briefly the photometric and spectroscopic reductions. In Figure 2.1 the different normalised throughput band-passes are represented for all the samples: CSP, Sloan Digital Sky Survey-II SN Survey (SDSS-II) and Supernova Legacy Survey (SNLS). As we can see the CSP filters and the SNLS filters were built to match very well the SDSS-II filters, permitting a minimisation of systematic errors when combining all the samples.

All optical images were reduced in a standard way including bias subtractions, flat-field corrections, application of a linearity correction and an exposure time correction for a shutter time delay. The NIR images were reduced through the following steps: dark subtraction, flat-field division, sky subtraction, geometric alignment and combination of the dithered frames. Due to the fact that SN II measurements can be affected by the underlying light of their host galaxies, we took care in correctly removing the underlying host-galaxy light. The templates used for final subtractions were always taken months/years after each SN II had faded and under seeing conditions better than those of the science frames. Because the templates for some SNe II were not taken with the same telescope, they were geometrically transformed to each individual science frame. Then they were convolved to match the point-spread functions, and finally scaled in flux. The template images were then subtracted from a circular region around the SN II position on each science frame (see Contreras et al. 2010).

Observed photometry of each SN II was derived relative to local sequence stars and calibrated from observations of standard stars in the Landolt (1992) (BV), Smith et al. (2002) ($u'g'r'i'$), and Persson et al. (2004) ($YJHKs$) systems. The photometry of the local sequence stars are an average of at least three photometric nights. Magnitudes are expressed in the natural photometric system of the Swope+CSP bands. Final errors for each SN II are the result of the instrumental magnitude uncertainty and the error on the zero point. The full photometric catalog will be published in an upcoming paper (Anderson et al. in prep), the V-band photometry has been already published in Anderson et al. (2014b).

As stated previously, the CSP data is one the best low redshift SNe II samples with unique well-defined and well-sampled light-curves in the optical and NIR. In Figure 2.2, I show the quality of the data by representing the light-curves ($ugri$ and $YJHK$) of two different SNe II, SN 2004fx, and SN 2005dz. As we can see, these SNe II have well sampled photometry during at least 100 days after the explosion. In Figure 2.3 for only the SNe II with optical and NIR photometry ($ugri$ and $YJHK$) I show two histograms. First, I present the number of SNe II versus the number of epochs for each SN II and second, I plot the epoch distribution of the first photometric point with respect to the explosion date. We can see that in average for the optical filters we have 15 epochs per SNe II, and the first epoch is around seven days after the explosion. On another hand, for the NIR filters we have 7-10 epochs per SNe II, while the first epoch is around 10 days after the explosion.

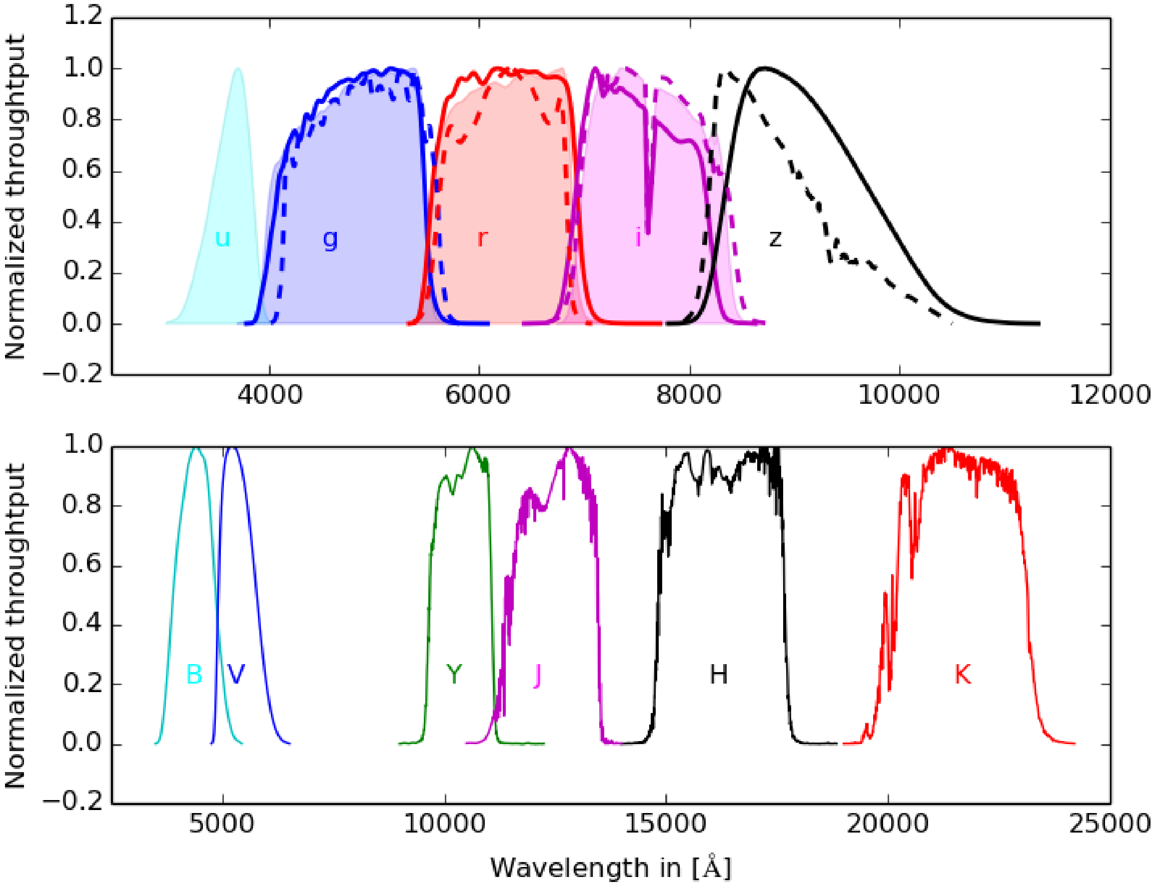

Figure 2.1: The CSP, SDSS-II, SNLS normalised throughput band-passes are represented. *Top:* The u, g, r, i, z normalised band-passes for the three sample are plotted. Filled curves is used for the CSP filters, solid lines for SDSS-II and dashed lines for SNLS. Cyan, blue, red, magenta and black are for u, g, r, i, z respectively. *Bottom:* B, V and Y, J, H, K normalised throughput band-passes are represented in cyan, blue, green, magenta, black, and red respectively.

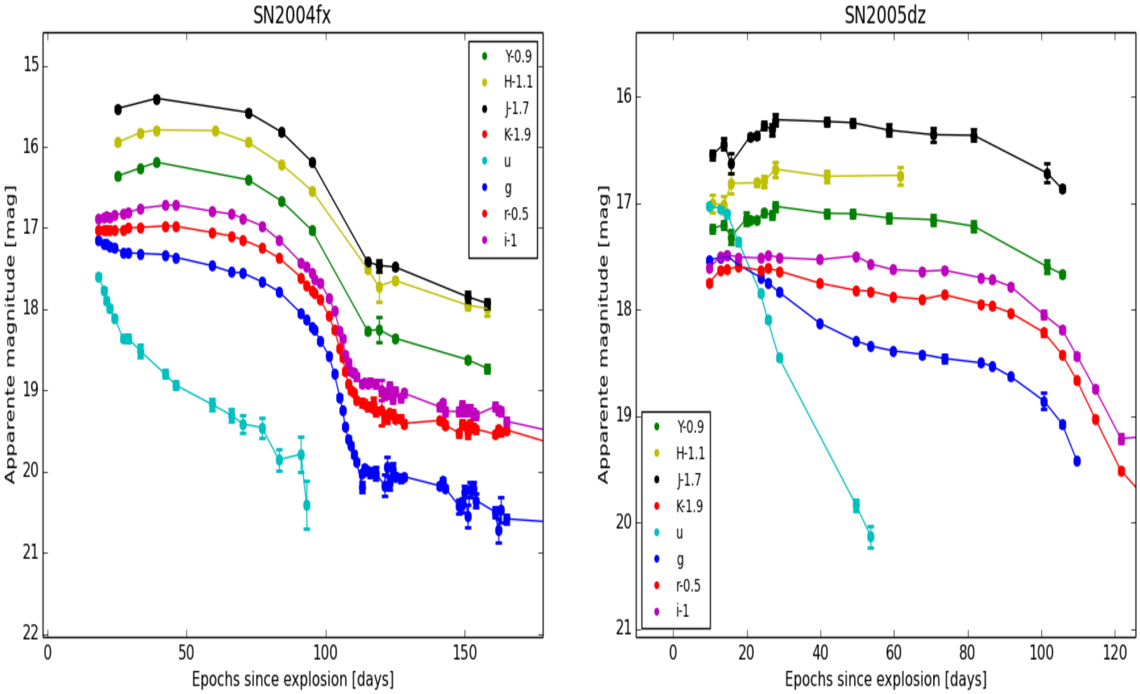

Figure 2.2: For $ugri$ and $YJHK$ filters for two SNe II (SN 2004fx, and SN 2005dz) from the CSP sample.

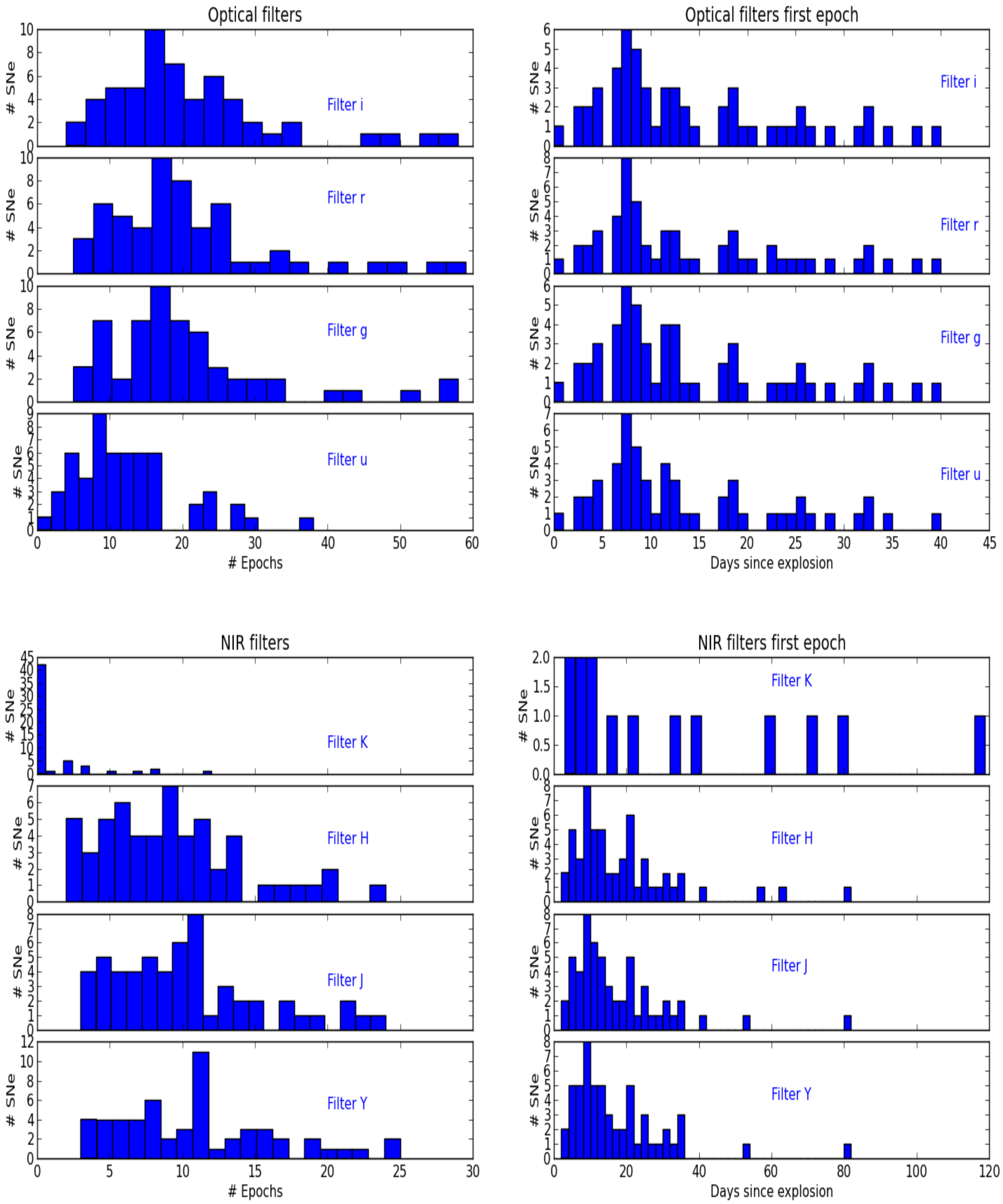

Figure 2.3: *Top Left:* Histogram of the number of epochs per SNe II for the optical bands. *Top Right:* Histogram of the number of days after explosion for the first photometric point for each SN II for the optical bands. *Bottom Left:* Histogram of the number of epochs per SNe II for the NIR bands. *Bottom Right:* Histogram of the number of days after explosion for the first photometric point for each SN II for the NIR bands.

2.1.1.2 Spectroscopy

The majority of our spectra were obtained with the 2.5m Irénée du Pont telescope using the WFCCD, Boller and Chiven instruments (the last is now decommissioned) at LCO. Additional spectra were obtained with the 6.5m Magellan Clay and Baade telescopes with LDSS-2, LDSS-3, MagE (see Massey et al. 2012 for details) and IMACS together with the CTIO 1.5m telescope and the Ritchey-Chrétien Cassegrain Spectrograph, and the New Technology Telescope (NTT) at La Silla observatory using the EMMI and EFOSC instruments. The majority of the spectra are the combination of three exposures for cosmic-ray rejection. Information about the grisms used, the exposure time, the observation strategy can be found in Hamuy et al. (2006), and Folatelli et al. (2010). All spectra were reduced in a standard way as described in Hamuy et al. (2006), Contreras et al. (2010), Stritzinger et al. (2011), and Folatelli et al. (2013). Briefly, the reduction was done with IRAF[2] using standard routines (bias subtraction, flat-field correction, 1-D extraction, wavelength and flux calibration). The full spectroscopic sample will be published in an upcoming paper and the reader can refer to Anderson et al. (2014a) and Gutiérrez et al. (2014) for a thorough analysis of this sample.

In Figure 2.4, I show two spectral sequences for two different SNe II: SN 2004fx and SN 2009N. I show for all the SNe II from the CSP sample two histograms. One is the number of spectra per SNe II and the second the epoch distribution since the explosion for the whole sample. The majority of the SNe II have several spectra (5-6) which allows us to measure the expansion velocity at different epochs, and thus have a better constraint on this value (cf Section 5). Additionally, in the second histogram we see that the majority of the spectra were taken during the plateau phase (~ 50 after the explosion), a period generally used to apply the SCM.

---

[2] IRAF is distributed by the National Optical Astronomy Observatory, which is operated by the Association of Universities for Research in Astronomy (AURA) under cooperative agreement with the National Science Foundation.

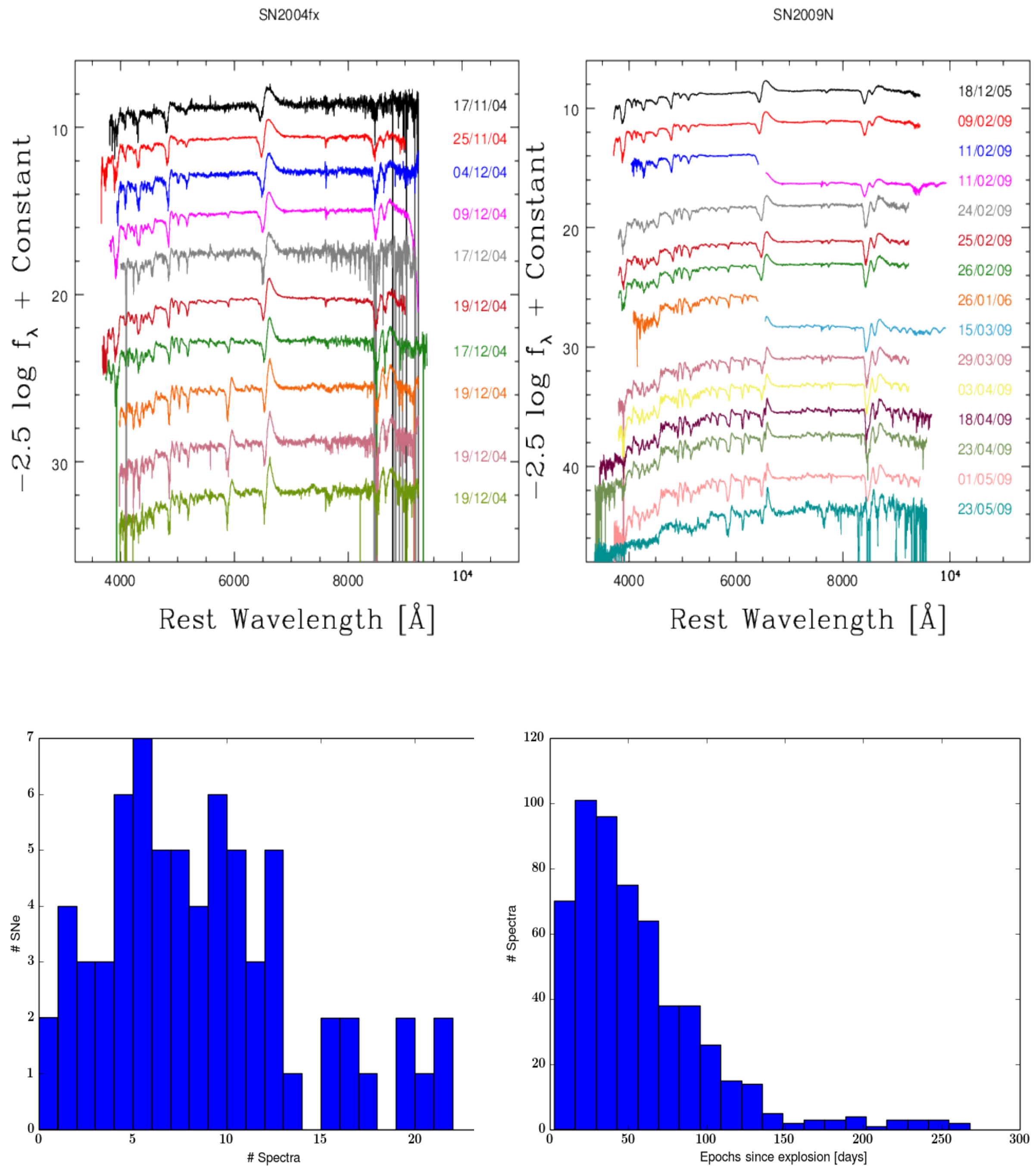

Figure 2.4: In both cases, each spectrum is labeled with the observation date. *Top Left*: Spectral sequence for SN 2004fx. *Top Right*: Spectra sequence for SN 2009N. *Bottom Left:* Histogram of the number of spectra per SNe II. *Bottom Right:* Histogram of the epoch of the spectra since the explosion.

2.2 Sloan Digital Sky Survey-II SN Survey (SDSS-II)

A better understanding of our Universe requires the observation of more distant SNe II. The differences between the expansion histories are extremely small, and distinguishing among them will require measurements extending far back in time, this is why we need to add to our low redshift sample, two other samples with SNe II at higher redshift.

The SDSS-II SN Survey (Frieman et al., 2008a) was operated during 3-years, from September 2005 to November 2007. Using the 2.5-m telescope at Apache Point Observatory in New Mexico (Gunn et al., 2006), repeatedly imaged the same region of the sky around the Southern equatorial stripe 82 (Stoughton et al., 2002). This survey observed about 80 spectroscopically confirmed CCSNe but the main driver of this project was the study of SNe Ia, involving the acquisition of only one or two spectra per SNe.

The images were obtained using the wide-field SDSS-II CCD camera (Gunn et al., 1998) and the photometry was computed using the five *ugriz* filters defined in Fukugita et al. (1996). The imaging data consist of 55 s exposures and were processed through the SDSS-II pipeline. More information about the data reduction can be found in York et al. (2000), Ivezić et al. (2004), and Holtzman et al. (2008).

Spectroscopic observations were performed using different telescopes and instruments such as: the 9.2 m HobbyEberly Telescope (HET) at McDonald Observatory, the 3.6 m New Technologies Telescope (NTT), the 3.5 m Astrophysical Research Consortium Telescope at Apache Point Observatory, the 8.2 m Subaru Telescope, the 2.4 m Hiltner Telescope at MDM Observatory, the 4 m Mayall Telescope at Kitt Peak National Observatory, the Magellan 6.5 m Clay Telescope, the 4.2 m WilliamHerschel Telescope, the 2.6 m Nordic Optical Telescope, and the 3.6 m Telescopio Nazionale Galileo (TNG).

The total SDSS-II SN sample is composed of 16 SNe II of which 15 SNe II are from D'Andrea et al. (2010). I included an additional object (SN 2007ny) because González-Gaitán et al. (2015) managed to measure the explosion date using his rise model. From the SDSS-II sample, I exclude SN 2007nv due to its large *i*-band uncertainties (D'Andrea et al., 2010). Figure 2.5, taken from D'Andrea et al. (2010), shows the whole spectra sample from SDSS-II, and the observed photometry of three SNe, low, medium and high redshift in this sample. Note that the majority of spectra were taken early, soon after the explosion, and so they only exhibit clearly the H_α λ6563 and H_β λ4861 lines, but very weak Fe II λ5018 or Fe II λ5169 lines which are often used for the SCM. The uncertainties on the redshift measurement is about 0.0005 when the redshift is measured using the host galaxy spectra, and about 0.005 when the SN II spectral features are used.

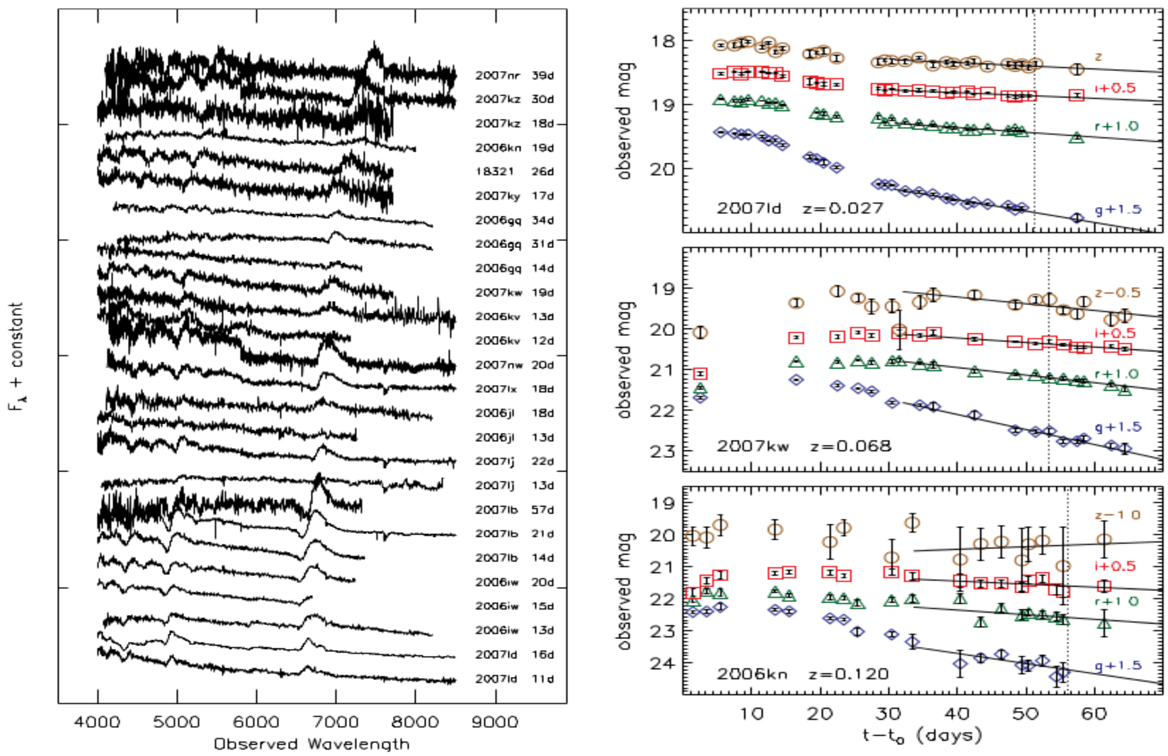

Figure 2.5: *Left*: Spectra for all the SNe in the SDSS-II sample. The date corresponds to epoch after the explosion and the spectra are shown in the observed frame. *Right*: Observed SDSS-II SN light curves for three typical SNe II are shown. Blue diamonds, green triangles, red squares, and brown circles are g, r, i, z-band magnitudes respectively. For clarity, each light curve has been offset by an amount indicated on each plot. Magnitudes have not been K- or S-corrected, nor have these light curves been corrected for extinction. These two figures were taken from D'Andrea et al. (2010)

2.3 Supernova Legacy Survey (SNLS)

In order to obtain a complete Hubble diagram, we also used high redshift SNe II from the SNLS. The SNLS was designed to discover SNe and to obtain a photometric follow-up using the MegaCam imager (Boulade et al., 2003) on the 3.6-m Canada-France-Hawaii Telescope. The observational strategy consisted of obtaining images of the same field every 4 nights during 5 years (between 2003 and 2008), thus, in total more than 470 nights were allocated to this project. Even if this sample was designed for SNe Ia cosmology and was very successful (Guy et al., 2010; Conley et al., 2011; Sullivan et al., 2011; Betoule et al., 2014), the observation of many SNe II with $0.1 \leq z \leq 0.5$ with good explosion date constraints and good photometric coverage allowed the use of this sample for SNe II cosmology (Nugent et al., 2006), to constrain SNe II rise-time (González-Gaitán et al., 2015) or to derive a precise measurement of the core-collapse SNe rate (Bazin et al., 2009).

Photometry was obtained in four pass-bands (g, r, i, z) similar to those used by the

SDSS-II and CSP (cf Figure 2.1; Regnault et al. 2009). After each run, the images are pre-processed using the Elixir pipeline (Magnier & Cuillandre, 2004), with flat-fielding and fringe subtraction. Then, sky background subtraction, astrometry, and photometric correction have been performed using two different and independent pipelines. These two pipelines do the same reduction steps but using different routines (IRAF). The description of all the data reduction steps can be found in Astier et al. (2006), Baumont et al. (2008), Regnault et al. (2009), Guy et al. (2010), Perrett et al. (2010), and Conley et al. (2011).

Due to the redshift of the SNe, and their faintness, spectroscopy observation requires 8-10 m telescopes. Spectroscopy was obtained using different large telescopes, such as the Very Large Telescope at Cerro Paranal, the 8-m Gemini-N telescope, and the 10-m Keck telescope at Mauna Kea in Hawaii. All spectra were reduced in a standard way as described in Howell et al. (2005), Bronder et al. (2008), Ellis et al. (2008), Balland et al. (2009), and Walker et al. (2011).

To be sure to select only SNe II from the full photometric sample (more than 6000 objects), as it was done by González-Gaitán et al. (2015) we selected only SNe II with spectroscopic redshift from the SN II or the host, a spectroscopic classification or a good photometric classification, and a well-defined explosion date. The total SNLS sample is composed of 28 SNe II, some of them were used in Nugent et al. (2006) to derive the first SNe II high redshift Hubble diagram. For this sample, 16 SNe II have a spectrum and could potentially be used for the SCM. We remove SN 07D2an identified as SN 1987A-like event by González-Gaitán et al. (2015). Figure 2.6 shows the spectral sequence for these 16 SNe II, we also show an example of three light curves obtained by the SNLS. As we can see, the explosion date are well defined thanks to the non detection photometric points. Also, as shown in Figure 2.6, some light-curves show a complete coverage during the plateau phase and a well defined plateau slope. From the spectral sequence we see that in general only one spectrum per SN II was obtained. The Fe II λ5018 or Fe II λ5169 lines are not always visible, which prevented us to measure the photospheric expansion velocity using these lines. Fortunately, we also see that many SNe exhibit a clear H_β absorption line (λ4861), which could be useful to use the SCM as shown in Chapter 5.

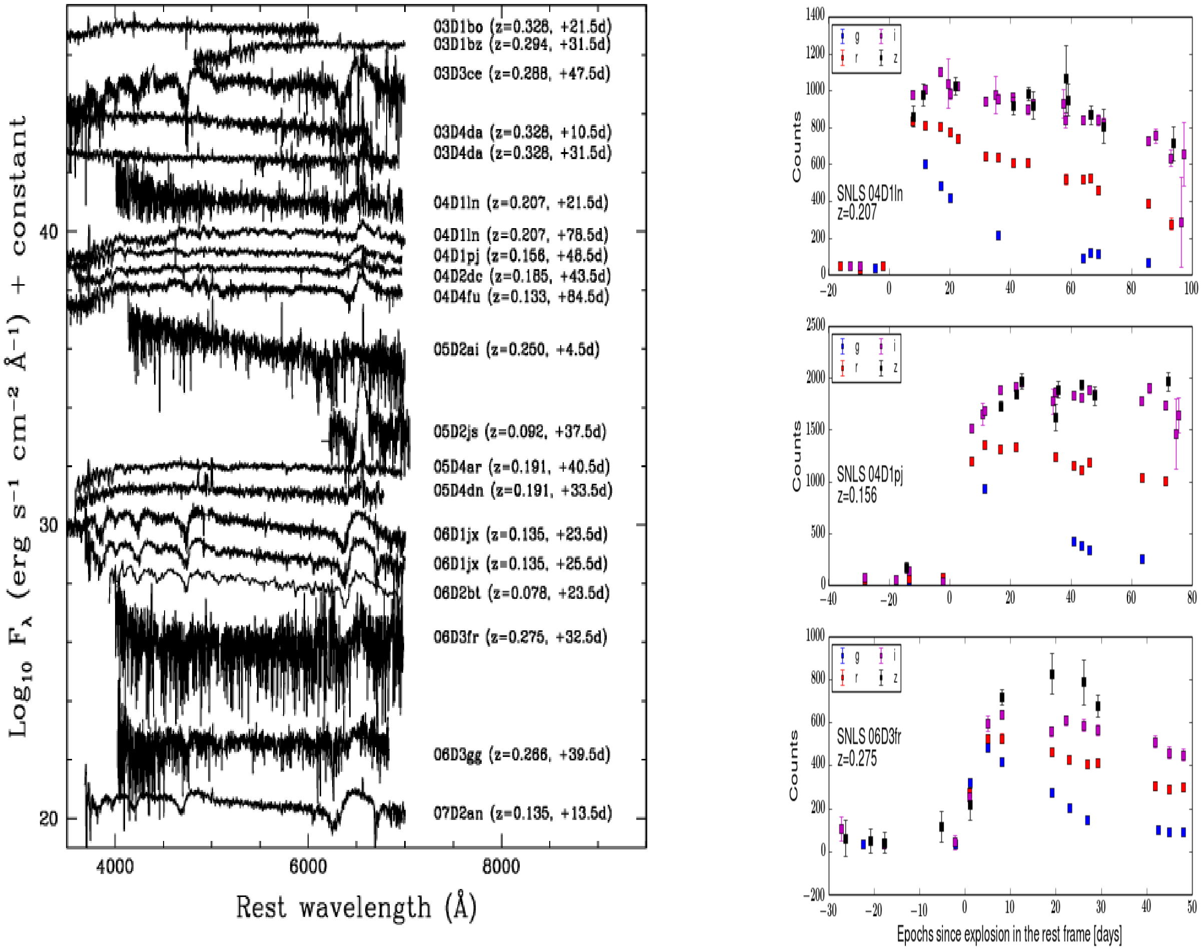

Figure 2.6: *Left*: Spectra of all the SNe II from the SNLS sample. The spectra are shown in the rest frame. The redshift and the date since the explosion is written for each SN II.*Right*: SNLS g, r, i, z light curves in counts for SNLS-04D1ln, SNLS-04D1pj, and SNLS-06D3fr (top to bottom) in the observer frame. Blue, red, magenta, and black squares are for $g, r, i,$ and z filters respectively.

The total SNe II sample for this thesis is composed of 105 SNe II, 61 SNe II from the CSP, 16 SNe II from SDSS-II, and 28 SNe II from SNLS. In Figure 2.7, I present the numerical proportion of each sub sample. The majority of the SNe II arises from the CSP sample ($\sim$ 60 %), following by the SNLS sample (25 %), and the SDSS-II sample (15 %)

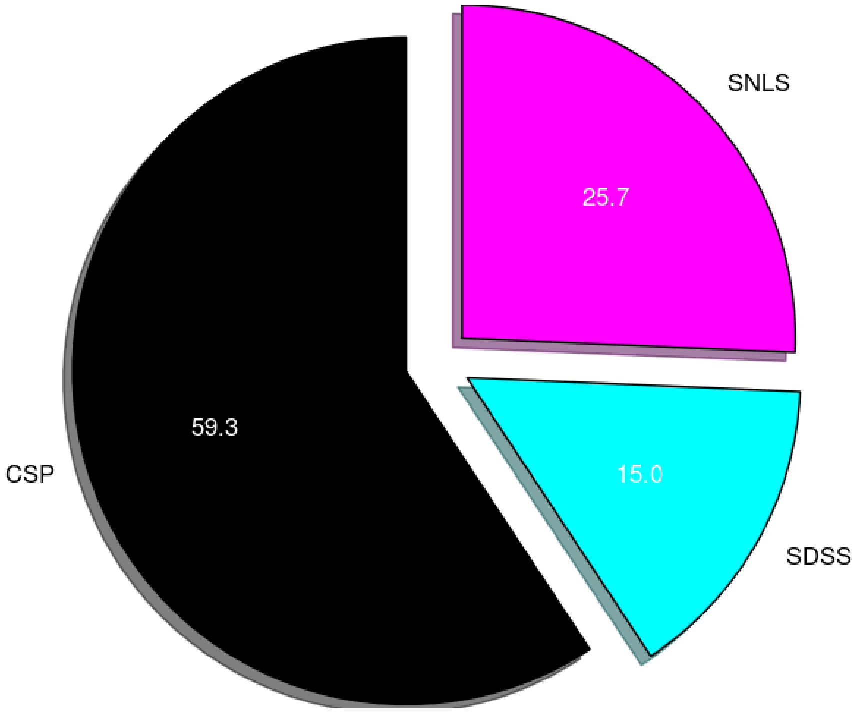

Figure 2.7: The proportion of each sample with respect to the total sample.

Table 2.1. Supernovae sample

SN	AvG mag	z_{helio}	z_{CMB} (err)	Explosion date MJD	s_2 mag 100d^{-1}	$v_{H\beta}$[2] km s^{-1}	μ_{PCM} mag	μ_{SCM} mag	Campaign[4]	Methods[4]
2004er[1]	0.070	0.0147	0.0139 (0.00011)	3271.8(4.0)	0.41(0.03)	8100(170)	33.37(0.06)	33.84(0.06)	CSP	PCM/SCM
2004fb	0.173	0.0203	0.0197 (0.00009)	3242.6(4.0)	0.47(0.10)	···	···	···	CSP	PCM/SCM
2004fc[1]	0.069	0.0061	0.0052 (0.00002)	3293.5(10.0)	-0.08(0.03)	···	···	···	CSP	PCM/SCM
2004fx[1]	0.282	0.0089	0.0089 (0.00001)	3303.5(4.0)	0.70(0.05)	···	···	···	CSP	PCM/SCM
2005J[1]	0.075	0.0139	0.0151 (0.00001)	3382.7(7.0)	0.59(0.01)	6160(160)	33.84(0.06)	33.98(0.07)	CSP	PCM/SCM
2005K	0.108	0.0273	0.0284 (0.00010)	3369.8(7.0)	1.06(0.08)	5490(260)	35.95(0.07)	35.64(0.10)	CSP	PCM/SCM
2005Z[1]	0.076	0.0192	0.0203 (0.00003)	3396.7(8.0)	1.30(0.02)	7510(160)	34.42(0.06)	34.62(0.07)	CSP	PCM/SCM
2005af	0.484	0.0019	0.0027 (0.00001)	3323.8(15.0)	-0.03(0.13)	···	···	···	CSP	PCM/SCM
2005an[1]	0.262	0.0107	0.0118 (0.00010)	3426.7(4.0)	1.82(0.05)	6650(170)	34.02(0.07)	33.88(0.07)	CSP	PCM/SCM
2005dk[1]	0.134	0.0157	0.0154 (0.00008)	3599.5(6.0)	0.86(0.03)	6900(170)	33.74(0.06)	33.94(0.07)	CSP	PCM/SCM
2005dn[1]	0.140	0.0094	0.0090 (0.00006)	3601.5(6.0)	1.22(0.04)	···	···	···	CSP	PCM/SCM
2005dt	0.079	0.0256	0.0570 (0.00008)	3605.6(9.0)	-0.01(0.07)	4500(190)	35.20(0.06)	35.03(0.08)	CSP	PCM/SCM
2005dw[1]	0.062	0.0176	0.0166 (0.00007)	3603.6(9.0)	0.76(0.03)	5040(310)	34.70(0.07)	34.41(0.11)	CSP	PCM/SCM
2005dx[1]	0.066	0.0267	0.0264 (0.00010)	3615.9(7.0)	0.58(0.04)	4660(190)	35.80(0.07)	35.47(0.08)	CSP	PCM/SCM
2005dz[1]	0.223	0.0190	0.0177 (0.00009)	3619.5(4.0)	0.33(0.02)	5965(170)	34.69(0.06)	34.73(0.07)	CSP	PCM/SCM
2005es[1]	0.228	0.0376	0.0364 (0.00018)	3638.7(10.0)	···	5055(190)	···	35.64(0.08)	CSP	PCM/SCM
2005gk[1]	0.154	0.0292	0.0286 (0.00010)	3647.8(1.0)	0.62(0.06)	···	35.41(0.06)	···	CSP	PCM/SCM
2005lw[1]	0.135	0.0257	0.0269 (0.00013)	3716.8(5.0)	1.27(0.05)	7375(180)	34.88(0.07)	35.01(0.07)	CSP	PCM/SCM
2005me	0.070	0.0224	0.0218 (0.00005)	3721.6(6.0)	0.99(0.10)	5700(240)	35.41(0.07)	35.23(0.08)	CSP	PCM/SCM
2006Y[1]	0.354	0.0336	0.0341 (0.00010)	3766.5(4.0)	0.90(0.14)	6890(160)	35.73(0.08)	35.92(0.07)	CSP	PCM/SCM
2006ai[1]	0.347	0.0152	0.0154 (0.00010)	3781.8(5.0)	1.15(0.05)	6430(160)	33.89(0.06)	33.87(0.06)	CSP	PCM/SCM
2006bc[1]	0.562	0.0045	0.0049 (0.00004)	3815.5(4.0)	···	···	···	···	CSP	PCM/SCM
2006be[1]	0.080	0.0071	0.0075 (0.00003)	3805.8(6.0)	0.11(0.03)	···	···	···	CSP	PCM/SCM
2006bl[1]	0.144	0.0324	0.0328 (0.00016)	3823.8(6.0)	1.13(0.09)	6550(180)	35.06(0.07)	35.30(0.07)	CSP	PCM/SCM
2006ee[1]	0.167	0.0154	0.0145 (0.00009)	3961.8(4.0)	-0.61(0.06)	3330(170)	33.96(0.06)	33.54(0.09)	CSP	PCM/SCM
2006it[1]	0.273	0.0155	0.0145 (0.00007)	4006.5(3.0)	···	···	···	···	CSP	PCM/SCM
2006ms[1]	0.095	0.0151	0.0147 (0.00007)	4034.0(12.0)	-0.53(0.06)	···	34.23(0.06)	···	CSP	PCM/SCM
2006qr[1]	0.126	0.0145	0.0155 (0.00007)	4062.8(7.0)	0.44(0.02)	5150(160)	34.82(0.05)	34.67(0.07)	CSP	PCM/SCM
2007P[1]	0.111	0.0407	0.0419 (0.00010)	4118.7(3.0)	0.28(0.12)	5710(220)	35.84(0.08)	35.87(0.08)	CSP	PCM/SCM
2007U[1]	0.145	0.0260	0.0260 (0.00003)	4134.6(6.0)	1.40(0.04)	7050(170)	34.91(0.06)	34.96(0.09)	CSP	PCM/SCM
2007W[1]	0.141	0.0097	0.0107 (0.00007)	4136.8(7.0)	-0.69(0.06)	3270(160)	33.78(0.06)	33.79(0.06)	CSP	PCM/SCM
2007aa[1]	0.072	0.0049	0.0061 (0.00008)	4135.8(5.0)	-0.09(0.09)	···	···	···	CSP	PCM/SCM
2007ab[1]	0.730	0.0235	0.0236 (0.00004)	4123.8(6.0)	2.87(0.05)	8580(190)	35.30(0.06)	35.08(0.07)	CSP	PCM/SCM
2007av[1]	0.099	0.0046	0.0058 (0.00008)	4175.7(5.0)	0.22(0.04)	···	···	···	CSP	PCM/SCM
2007hm[1]	0.172	0.0251	0.0241 (0.00008)	4335.6(6.0)	1.30(0.04)	6260(200)	35.92(0.06)	35.74(0.07)	CSP	PCM/SCM
2007il[1]	0.129	0.0215	0.0205 (0.00008)	4349.8(4.0)	-0.42(0.03)	6110(160)	34.81(0.06)	34.66(0.08)	CSP	PCM/SCM
2007it	0.316	0.0040	0.0047 (0.00050)	4348.5(1.0)	···	···	···	···	CSP	PCM/SCM
2007oc[1]	0.061	0.0048	0.0039 (0.00007)	4388.5(3.0)	1.31(0.03)	···	···	···	CSP	PCM/SCM
2007od[1]	0.100	0.0058	0.0045 (0.00006)	4402.6(5.0)	0.70(0.06)	···	···	···	CSP	PCM/SCM
2007sq[1]	0.567	0.0153	0.0162 (0.00007)	4421.8(3.0)	0.34(0.05)	7500(170)	34.28(0.06)	34.69(0.06)	CSP	PCM/SCM
2008F[1]	0.135	0.0183	0.0177 (0.00008)	4470.6(6.0)	-0.63(0.08)	4825(170)	34.77(0.07)	34.88(0.08)	CSP	PCM/SCM
2008M[1]	0.124	0.0076	0.0079 (0.00002)	4471.7(9.0)	0.23(0.05)	···	···	···	CSP	PCM/SCM
2008W[1]	0.267	0.0192	0.0201 (0.00016)	4485.8(6.0)	0.26(0.04)	5760(160)	34.92(0.06)	34.65(0.07)	CSP	PCM/SCM
2008ag[1]	0.229	0.0148	0.0147 (0.00002)	4479.8(6.0)	-0.32(0.03)	4760(160)	33.42(0.06)	33.42(0.07)	CSP	PCM/SCM
2008aw[1]	0.111	0.0104	0.0114 (0.00007)	4517.8(10.0)	1.49(0.05)	6900(160)	33.22(0.06)	33.19(0.06)	CSP	PCM/SCM
2008bh[1]	0.060	0.0145	0.0154 (0.00007)	4543.5(5.0)	0.65(0.04)	6470(180)	34.55(0.06)	34.67(0.07)	CSP	PCM/SCM
2008bk[1]	0.054	0.0008	-0.0001 (0.00006)	4542.9(6.0)	···	···	···	···	CSP	PCM/SCM
2008br	0.255	0.0101	0.0111 (0.00007)	4555.7(9.0)	-0.65(0.05)	2420(180)	34.19(0.06)	33.33(0.12)	CSP	PCM/SCM
2008bu[1]	1.149	0.0221	0.0222 (0.00003)	4566.8(5.0)	-0.07(0.33)	5930(200)	34.59(0.14)	34.96(0.09)	CSP	PCM/SCM
2008ga[1]	1.865	0.0155	0.0153 (0.00001)	4711.8(4.0)	1.01(0.05)	5550(270)	34.19(0.07)	34.03(0.09)	CSP	PCM/SCM
2008gi[1]	0.181	0.0244	0.0237 (0.00012)	4742.7(9.0)	1.31(0.05)	6420(220)	34.97(0.07)	34.95(0.07)	CSP	PCM/SCM
2008gr[1]	0.039	0.0229	0.0218 (0.00015)	4766.5(4.0)	0.91(0.06)	7540(170)	34.42(0.06)	34.73(0.06)	CSP	PCM/SCM
2008hg[1]	0.050	0.0190	0.0182 (0.00006)	4779.7(5.0)	-1.32(0.56)	4300(180)	34.70(0.20)	34.82(0.08)	CSP	PCM/SCM
2008ho	0.052	0.0103	0.0096 (0.00050)	4792.7(5.0)	-0.72(0.07)	···	···	···	CSP	PCM/SCM
2008if	0.090	0.0115	0.0125 (0.00008)	4807.8(5.0)	1.27(0.04)	7100(160)	33.61(0.06)	33.74(0.06)	CSP	PCM/SCM
2008il	0.045	0.0210	0.0203 (0.00005)	4825.6(3.0)	-0.07(0.07)	···	34.90(0.07)	···	CSP	PCM/SCM
2008in	0.061	0.0050	0.0064 (0.00008)	4822.8(6.0)	0.03(0.04)	···	···	···	CSP	PCM/SCM
2009N[1]	0.057	0.0034	0.0046 (0.00008)	4846.7(5.0)	-0.73(0.03)	···	···	···	CSP	PCM/SCM
2009ao[1]	0.106	0.0111	0.0122 (0.00007)	4890.6(4.0)	0.93(0.10)	5570(160)	33.61(0.07)	33.42(0.07)	CSP	PCM/SCM
2009au	0.250	0.0094	0.0104 (0.00007)	4897.5(4.0)	2.33(0.06)	···	···	···	CSP	PCM/SCM
2009bu[1]	0.070	0.0116	0.0112 (0.00004)	4907.9(6.0)	-0.31(0.03)	5670(160)	33.40(0.07)	33.61(0.07)	CSP	PCM/SCM
2009bz[1]	0.110	0.0108	0.0113 (0.00004)	4915.8(4.0)	0.07(0.04)	6030(160)	33.67(0.08)	33.92(0.07)	CSP	PCM/SCM
8321	0.080	0.1041	0.1065 (0.00050)	4353.6(5.0)	1.34(0.03)	6690(180)	38.09(0.28)	38.93(0.23)	SDSS-II	PCM/SCM
2006gq	0.096	0.0697	0.0687 (0.00050)	3992.4(3.0)	0.28(0.03)	4890(230)	37.34(0.10)	37.56(0.12)	SDSS-II	PCM/SCM
2006iw	0.137	0.0308	0.0295 (0.00050)	4010.7(1.0)	0.14(0.03)	6900(510)	35.44(0.08)	35.70(0.12)	SDSS-II	PCM/SCM
2006jl	0.504	0.0555	0.0554 (0.00050)	4006.8(15.0)	0.52(0.03)	8640(700)	···	36.81(0.15)	SDSS-II	PCM/SCM
2006kn	0.194	0.1199	0.1190 (0.00050)	4007.0(1.5)	1.55(0.03)	6330(200)	38.43(0.29)	38.48(0.25)	SDSS-II	PCM/SCM
2006kv	0.080	0.0619	0.0620 (0.00050)	4016.5(4.0)	1.60(0.03)	5590(190)	37.26(0.14)	37.08(0.14)	SDSS-II	PCM/SCM
2007kw	0.074	0.0681	0.0672 (0.00050)	4361.6(2.5)	1.00(0.03)	6610(250)	37.02(0.09)	37.10(0.09)	SDSS-II	PCM/SCM
2007ky	0.105	0.0737	0.0727 (0.00050)	4363.5(3.0)	0.38(0.03)	5170(170)	37.62(0.16)	37.17(0.14)	SDSS-II	PCM/SCM
2007kz	0.320	0.1275	0.1270 (0.00050)	4362.6(3.5)	1.44(0.03)	6060(200)	38.71(0.25)	39.02(0.33)	SDSS-II	PCM/SCM
2007lb	0.496	0.0379	0.0375 (0.00050)	4368.8(7.0)	0.22(0.03)	7350(370)	35.31(0.07)	35.77(0.10)	SDSS-II	PCM/SCM
2007ld	0.255	0.0270	0.0267 (0.00500)	4369.6(5.5)	0.53(0.03)	6620(420)	35.07(0.07)	35.24(0.42)	SDSS-II	PCM/SCM
2007lj	0.118	0.0500	0.0489 (0.00500)	4370.2(3.5)	0.84(0.03)	5610(300)	36.72(0.07)	36.43(0.25)	SDSS-II	PCM/SCM
2007lx	0.120	0.0571	0.0559 (0.00050)	4374.5(8.0)	0.47(0.03)	5520(200)	37.07(0.22)	37.10(0.11)	SDSS-II	PCM/SCM
2007nr	0.079	0.1400	0.1389 (0.00050)	4353.5(5.0)	1.25(0.03)	5230(190)	39.53(0.40)	39.27(0.30)	SDSS-II	PCM/SCM
2007nw	0.204	0.0571	0.0555 (0.00050)	4372.2(7.0)	-0.06(0.03)	5810(200)	37.17(0.12)	36.96(0.12)	SDSS-II	PCM/SCM
2007ny	0.080	0.1429	0.1419 (0.00050)	4367.7(7.0)	1.39(1.44)	6860(190)	39.43(0.64)	39.14(0.45)	SDSS-II	PCM/SCM
03D1bo	0.066	0.3279	0.3271 (0.00100)	2888.0(4.0)	···	···	···	···	SNLS	PCM/SCM

Table 2.1 (cont'd)

SN	AvG mag	z_{helio}	z_{CMB} (err)	Explosion date MJD	s_2 mag $100d^{-1}$	$v_{H\beta}{}^2$ km s^{-1}	μ_{PCM} mag	μ_{SCM} mag	Campaign[4]	Methods[4]
03D1bz	0.066	0.2939	0.2931 (0.00100)	2914.0(4.0)	0.16(0.23)	···	···	···	SNLS	PCM/SCM
03D3ce	0.026	0.2880	0.2884 (0.00100)	2780.0(10.0)	···	···	···	···	SNLS	PCM/SCM
03D4az	0.076	0.4079	0.4069 (0.00100)	2808.0(4.0)	-0.47(1.49)	···	···	···	SNLS	PCM
03D4bl	0.072	0.3179	0.3169 (0.00100)	2822.0(3.0)	1.32(1.46)	···	41.43(0.57)	···	SNLS	PCM
03D4da	0.078	0.3279	0.3269 (0.00100)	2874.0(7.0)	···	···	···	···	SNLS	PCM/SCM
04D1ha	0.073	0.4839	0.4831 (0.00100)	3233.0(3.0)	0.11(0.42)	···	42.13(0.44)	···	SNLS	PCM
04D1ln	0.071	0.2069	0.2062 (0.00100)	3274.0(5.0)	0.32(0.12)	···	40.28(0.11)	···	SNLS	PCM/SCM
04D1nz	0.072	0.2629	0.2621 (0.00100)	3264.0(4.0)	0.13(0.37)	···	40.74(0.30)	···	SNLS	PCM
04D1pj	0.076	0.1559	0.1552 (0.00100)	3304.0(8.0)	0.02(0.14)	5975(230)	39.13(0.09)	39.37(0.10)	SNLS	PCM/SCM
04D1qa	0.072	0.1719	0.1711 (0.00100)	3300.0(3.0)	-0.10(0.40)	···	39.65(0.19)	···	SNLS	PCM
04D2dc	0.053	0.1849	0.1861 (0.00100)	3040.0(25.0)	0.14(0.19)	···	···	···	SNLS	PCM/SCM
04D4fu	0.072	0.1329	0.1319 (0.00100)	3213.0(6.0)	0.23(0.60)	4785(200)	39.21(0.23)	39.02(0.10)	SNLS	PCM/SCM
04D4hg	0.073	0.5169	0.5159 (0.00100)	3233.0(3.0)	···	···	···	···	SNLS	PCM
05D1je	0.071	0.3089	0.3081 (0.00100)	3647.0(5.0)	-0.22(0.80)	···	41.46(0.36)	···	SNLS	PCM
05D2ai	0.052	0.2489	0.2501 (0.00100)	3377.0(9.0)	···	···	···	···	SNLS	PCM/SCM
05D2ed	0.051	0.1959	0.1971 (0.00100)	3417.0(5.0)	-0.08(0.34)	···	39.50(0.16)	···	SNLS	PCM
05D2js	0.051	0.0926	0.0934 (0.00100)	3670.0(17.0)	···	···	···	···	SNLS	PCM/SCM
05D2or	0.051	0.2470	0.2480 (0.00100)	3731.0(3.0)	0.77(0.46)	···	···	···	SNLS	PCM
05D4ar	0.072	0.1909	0.1889 (0.00100)	3520.0(25.0)	0.80(0.50)	···	40.16(0.24)	···	SNLS	PCM/SCM
05D4cb	0.073	0.1999	0.1989 (0.00100)	3563.0(3.0)	0.41(0.13)	···	39.66(0.11)	···	SNLS	PCM
05D4dn	0.073	0.1909	0.1889 (0.00100)	3605.0(7.0)	0.55(0.42)	4970(210)	40.19(0.23)	39.90(0.22)	SNLS	PCM/SCM
05D4du	0.072	0.3099	0.3089 (0.00100)	3585.0(5.0)	0.01(0.30)	···	41.15(0.25)	···	SNLS	PCM
06D1jx	0.079	0.1349	0.1342 (0.00100)	4068.0(6.0)	-0.39(0.14)	6110(190)	38.82(0.08)	39.23(0.10)	SNLS	PCM/SCM
06D2bt	0.051	0.0779	0.0791 (0.00100)	3745.0(10.0)	-0.02(0.23)	5965(200)	37.69(0.10)	37.90(0.08)	SNLS	PCM/SCM
06D2ci	0.053	0.2199	0.2211 (0.00100)	3768.0(4.0)	1.08(0.25)	···	40.46(0.16)	···	SNLS	PCM
06D3fr	0.025	0.2749	0.2754 (0.00100)	3883.0(4.0)	···	···	···	···	SNLS	PCM/SCM
06D3gg	0.024	0.2659	0.2663 (0.00100)	3897.0(6.0)	···	···	···	···	SNLS	PCM/SCM

[1] SN II with optical and near-infrared photometry

[2] 45 days post-explosion

[3] CSP=Carnegie Supernova Project, SDSS-II=Sloan Digital Sky Survey, SNLS= Supernova Legacy Survey

[4] PCM=Photometric color Method, SCM=Standard Candle Method

Note. — In the first column the SN II name, followed by its reddening due to dust in our Galaxy (Schlafly & Finkbeiner, 2011) are listed. In column 3 I list host-galaxy heliocentric recession velocities. These are taken from the NASA Extragalactic Database (NED: `http://ned.ipac.caltech.edu/`). In column 4 I list the host-galaxy velocity in the CMB frame using the CMB dipole model presented by Fixsen et al. (1996). In column 5 the explosion epochs is presented. In column 6, I list the survey from which the SN II originates. In column 7 and column 8, I list the survey that the SN II belongs, the s_2 value (defined in Section 4) and the Hβ velocity at an epoch of 45 days after the explosion Finally, in the last column I show for each the SN II the method available, i.e., whether a spectrum is available or not.

Chapter 3

Methodology and Procedure

Contents

In this chapter, I explain my routine to correct the apparent magnitudes for Milky Way extinction, S-correction (Stritzinger et al., 2002) and K-correction (Hubble, 1936) in order to be able to construct the SNe II Hubble diagram from three different photometric systems.

3.1 Methodology

The photon flux observed in one photometric system is affected by four different sources: the dust in our Milky Way (AvG), the expansion of the Universe (K-correction; Oke & Sandage 1968; Hamuy et al. 1993; Kim et al. 1996; Nugent et al. 2002), the host-galaxy extinction (Avh), and by the difference between the natural photometric system used to obtain observations and the standard photometric system (S-correction; Stritzinger et al. 2002).

In this paragraph I describe the four sources, but then, I correct the apparent magnitudes only for Milky Way extinction, K and S-corrections due to the difficulty in applying the host galaxy extinction correction as explained later and in the Appendix. Collectively, we call the AvG+K-correction+S-correction the AKS correction.

- Dust extinction in our Galaxy is due to the small and solid grains of heavy elements formed in the core of massive stars and ejected in the ISM by stellar winds and SN explosions (Draine, 2003). Dust scatters and absorbs more blue light than red light, and therefore SNe with strong AvG will be characterised by a redder continuum. To correct for AvG, I used the value derived by Schlafly & Finkbeiner (2011).

- After having corrected the observed magnitudes by the AvG, one needs to apply the K-correction (KC). The KC first introduced by Hubble (1936) allows us to correct the observed magnitude by a factor imputable to the redshift caused by the expansion of space (see the short pedagogical paper by Hogg et al. 2002 but also Oke & Sandage 1968; Hamuy et al. 1993; Kim et al. 1996; Nugent et al. 2002). In Figure 3.1 we see a spectrum of a SN in the rest frame and the B band pass. In the bottom, the same spectrum is represented but this time redshifted (z=0.45). We clearly see that a photon emitted by a SN at z=0.45 in the B band will be observed on the Earth in the R band. The more distant is the object the more important this effect will be.

- In this thesis, I use three different samples with similar but different photometric systems. To combine all these samples we need to put all the data in the same standard system in order to minimize systematic effects (S-correction; Stritzinger et al. 2002). The CSP natural system is chosen as reference due to the fact that it is the best understood system and because $\sim$ 60% of the total SNe II arises from the CSP sample.

- Correcting for Avh is more complicated. To date, no accurate methods exist. For example, the equivalent width of the Na I line (Turatto et al., 2003) is a bad proxy for extinction (Poznanski et al., 2011). For the colour-colour diagram, and multi-band fit methods (Folatelli et al., 2013; Rodríguez et al., 2014) a better understanding and estimation of the SNe II intrinsic colours is necessary to derive a good approximation to Avh. These two methods are detailed in the Appendix. Due to the lack of robust methods to compute Avh, this correction is not included in the AKS routine. Instead, and similarly to what has been done in SNe Ia cosmology, I add a colour term correction in the standardisation method, a $\beta_{\lambda 1}$(m$_{\lambda 2}$-m$_{\lambda 3}$) which is related to the host galaxy extinction if we assume that the colour-magnitude relation is due to extrinsic factors and than the intrinsic colour is constant:

$$\begin{aligned} A_{\lambda 1} =& \beta_{\lambda 1} \times E(m_{\lambda 2} - m_{\lambda 3}) \\ =& \beta_{\lambda 1} \left[(m_{\lambda 2} - m_{\lambda 3}) - (m_{\lambda 2} - m_{\lambda 3})_0 \right] \\ =& \beta_{\lambda 1} (m_{\lambda 2} - m_{\lambda 3}) - constant, \end{aligned} \tag{3.1}$$

where $A_{\lambda 1}$ is the host-galaxy extinction in the $\lambda 1$ filter, E the colour excess, and $(m_{\lambda 2} - m_{\lambda 3})_0$ the intrinsic colour.

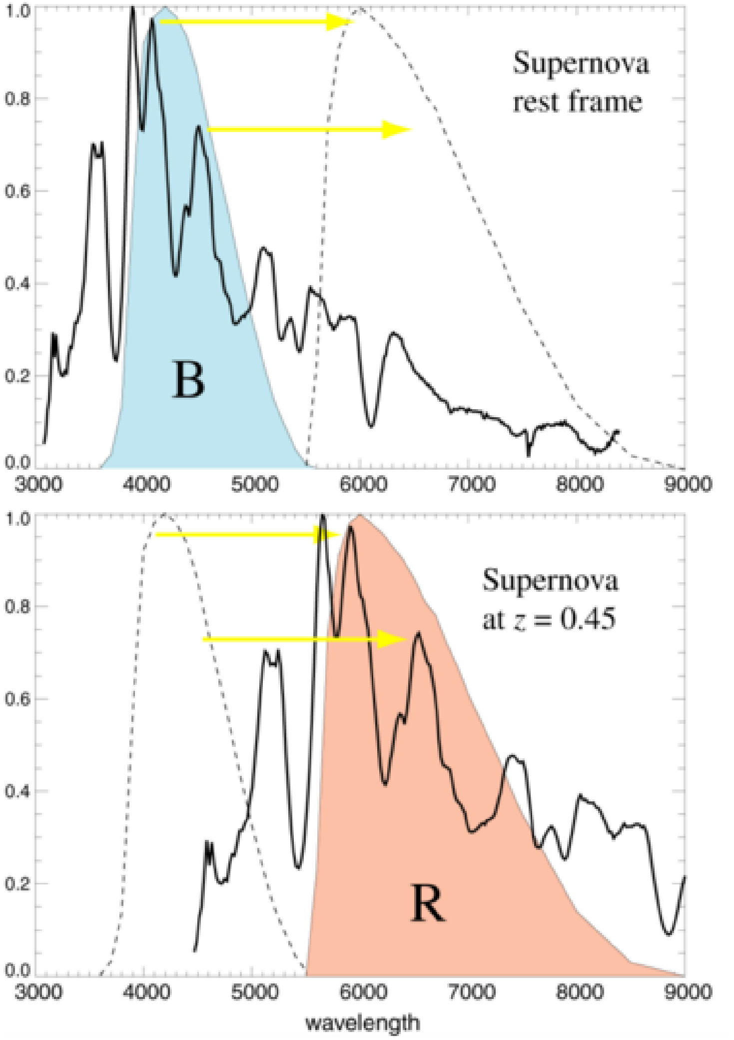

Figure 3.1: *Top figure:* A supernova spectrum is represented in the rest frame in black. Filled blue curve represents the band pass of the B filter. *Bottom figure:* The same spectrum is represented but at redshift 0.45. Filled pink curve represents the band pass of the R filter.

3.2 Theoretical derivation

The AKS_{XY} correction converting the apparent magnitude in the Y filter, m$_Y$, to the absolute magnitude in filter X, M$_X$ is defined as:

$$m_Y = M_X + \mu + AKS_{XY}. \tag{3.2}$$

where μ, the distance modulus is defined as:

$$\mu = 5\ log_{10}(\frac{d_L}{10pc}) \tag{3.3}$$

First we will derive the absolute magnitude and then the observed magnitude. In this notation, the observed wavelength is λ and the rest frame wavelength is $\lambda^{'}$, both quantities related by $\lambda = \lambda^{'}(1+z)$. In these equations I do not take into account the host galaxy extinction, only the Milky Way extinction is represented.

The energy flux density emitted in d$\lambda^{'}$ bin of a SN 10 pc away is:

$$f_\lambda(\lambda^{'})d\lambda^{'}. \tag{3.4}$$

In term of photons, this can be rewritten as:

$$\begin{aligned} N_\lambda d\lambda^{'} =& \frac{\lambda^{'}}{hc} f_\lambda(\lambda^{'})d\lambda^{'} \\ =& \frac{\lambda^{'}}{hc}\frac{L_\lambda(\lambda^{'})}{4\pi 10^2}d\lambda^{'} \end{aligned} \tag{3.5}$$

with L_λ in erg s^{-1} Å^{-1} and N_λ in photons s^{-1} Å^{-1}.

From this equation we can obtain the absolute magnitude in the standard system (i.e. CSP) defined as:

$$\begin{aligned} M_X^{CSP} =& -2.5\ log_{10}\int N_\lambda(\lambda^{'})S_X^{CSP}(\lambda^{'})d\lambda^{'} + ZP_X^{CSP} \\ M_X^{CSP} =& -2.5\ log_{10}\int \frac{\lambda^{'}}{hc}\frac{L_\lambda(\lambda^{'})}{4\pi 10^2} S_X^{CSP}(\lambda^{'})d\lambda^{'} + ZP_X^{CSP}, \end{aligned} \tag{3.6}$$

where ZP$_X^{CSP}$ is the zero point of filter X and S_X^{CSP} effective transmission of the X bandpass.

Now we can derive the observed magnitude. In a time and wavelength interval, the number of photons emitted is $N_\lambda(\lambda^{'})d\lambda^{'}dt^{'}$. The radiation emitted by the SN is distributed uniformly across a sphere of coordinate r and the observer would receive the photons across an area A$_p$(t$^{'}$)=$4\pi d_p^2$ where d_p is the proper distance (see 1.2.1.3).

Thus, the number of photons received (n_λ, in photons s^{-1} Å^{-1} cm^{-2}) during a time and wavelength interval as measured by the observer is:

$$
\begin{aligned}
n_\lambda d\lambda dt =& \frac{N_\lambda(\lambda^{'})d\lambda^{'}dt^{'}}{A_p(t^{'})}10^{-0.4(AvG(\lambda))} && \text{(3.7a)}\\
n_\lambda =& N_\lambda(\lambda^{'})\frac{d\lambda^{'}}{d\lambda}\frac{dt^{'}}{dt}\frac{1}{A_p(t^{'})}10^{-0.4(AvG(\lambda))} && \text{(3.7b)}
\end{aligned}
$$

where $AvG(\lambda)$ is added because the number of photons received is affected by the Milky Way extinction. We know also that $d\lambda = d\lambda^{'}(1+z)$, $dt = dt^{'}(1+z)$ and d_L=(1+z)d_p, so finally we obtain:

$$
\begin{aligned}
n_\lambda =& N_\lambda(\lambda^{'})\frac{1}{(1+z)}\frac{1}{(1+z)}\frac{1}{4\pi d_p^2}10^{-0.4(AvG(\lambda))} && \text{(3.8a)}\\
n_\lambda =& N_\lambda(\lambda^{'})\frac{1}{4\pi d_L^2}10^{-0.4(AvG(\lambda))} && \text{(3.8b)}\\
n_\lambda =& L_\lambda(\lambda^{'})\frac{\lambda^{'}/hc}{4\pi d_L^2}10^{-0.4(AvG(\lambda))} && \text{(3.8c)}
\end{aligned}
$$

The magnitude observed (CSP, SDSS, or SNLS) in bandpass Y is:

$$
\begin{aligned}
m_Y^{obs} =& -2.5\ log_{10}\int n_\lambda(\lambda)S_Y^{obs}(\lambda)d\lambda + ZP_Y^{obs}\\
=& -2.5\ log_{10}\int L_\lambda(\lambda^{'})\frac{\lambda^{'}/hc}{4\pi d_L^2}10^{-0.4(AvG(\lambda))}S_Y^{obs}(\lambda)d\lambda + ZP_Y^{obs}
\end{aligned} \tag{3.9}
$$

where ZP$_Y^{obs}$ is the zero point and S_Y^{obs} effective transmission of the Y bandpass.

Finally using equations 3.6, 3.9 , and 3.2 we can derive the AKS_{XY}:

$$
\begin{aligned}
AKS_{XY} =& m_Y^{obs} - M_X^{CSP} - \mu\\
=& -2.5\ log_{10} + \frac{\int L_\lambda(\lambda^{'})\frac{\lambda^{'}/hc}{4\pi d_L^2}10^{-0.4(AvG(\lambda))}S_Y^{obs}(\lambda)d\lambda}{\int \frac{\lambda^{'}}{hc}\frac{L_\lambda(\lambda^{'})}{4\pi 10^2}S_X^{CSP}(\lambda^{'})d\lambda^{'}} + (ZP_Y^{obs} - ZP_X^{CSP}) - 5\ log_{10}(\frac{d_L}{10pc})\\
=& -2.5\ log_{10} + \frac{\int \lambda^{'}L_\lambda(\lambda^{'})10^{-0.4(AvG(\lambda))}S_Y^{obs}(\lambda)d\lambda}{\int \lambda^{'}L_\lambda(\lambda^{'})S_X^{CSP}(\lambda^{'})d\lambda^{'}} + (ZP_Y^{obs} - ZP_X^{CSP})\\
=& 2.5\ log_{10}(1+z) - 2.5\ log_{10}\frac{\int \lambda L_\lambda(\frac{\lambda}{(1+z)})10^{-0.4(AvG(\lambda))}S_Y^{obs}(\lambda)d\lambda}{\int \lambda^{'}L_\lambda(\lambda^{'})S_X^{CSP}(\lambda^{'})d\lambda^{'}} + (ZP_Y^{obs} - ZP_X^{CSP})
\end{aligned} \tag{3.10}
$$

The AKS_{XY} is the cross-filter K correction as defined by Kim et al. (1996) and allows us to transform the magnitude in the observed filter Y (CSP, SDSS, SNLS), to the magnitude in the standard system (filter X; CSP).

3.3 Procedure

In practice, to apply the equation 3.10 to each magnitude a spectral energy distribution (SED) template series is needed. In this work, I adopt as SED the theoretical model from Dessart et al. (2013). This sequence of theoretical spectral models from Dessart et al. (2013) consist of a SN progenitor with a main-sequence mass of 15 $M_\odot$, solar metallicity Z =0.02, zero rotation and a mixing-length parameter of 3[1]. Note the model covers a limited range of epochs from 12.2 to 133 days relative to explosion. The choice of the model was motivated by the very good match of the theoretical model to the data of the prototypical SNe II (SN 1999em). Here, for one epoch and one filter , I describe step by step, the method to transform an observed magnitude to the CSP photometric system. For this illustration, I use SN 2005J at one specific epoch (39 days after explosion, i.e., during the plateau phase) in V-band and show the figures in Figure 3.2.

1. Step 1: From our model spectral library (Dessart et al., 2013), I choose the theoretical spectrum (rest frame) closest to the photometric epoch since explosion time (corrected for time dilatation, 1/(1+z)), with a rest-frame SED, $f^{rest}(\lambda_{rest})$. Because our library covers a limited range of epochs from 12.2 to 133 days relative to explosion, observations outside these limits are ignored. This step is represented in Figure 3.2 (a). The red spectrum corresponds to the theoretical spectrum in the rest frame with the epoch closest to 38.31 days after the explosion (39 days/(1+z)).

2. Step 2: I bring the rest-frame theoretical spectrum to the observer's frame using the (1+z_{hel}) correction, where z_{hel} is the heliocentric redshift[2] of the SN, $f^{obs}(\lambda) = f^{rest}(\lambda_{rest}(1 + z_{hel})) \times 1/(1 + z_{hel})$, where λ is the wavelength in the observer's frame. The black spectrum shown in Figure 3.2 (a) represents this step.

---

[1] More information about this model (named m15mlt3) can be found in Dessart et al. (2013)

[2] the rotation of Earth and orbital motions have been removed from the measured velocity

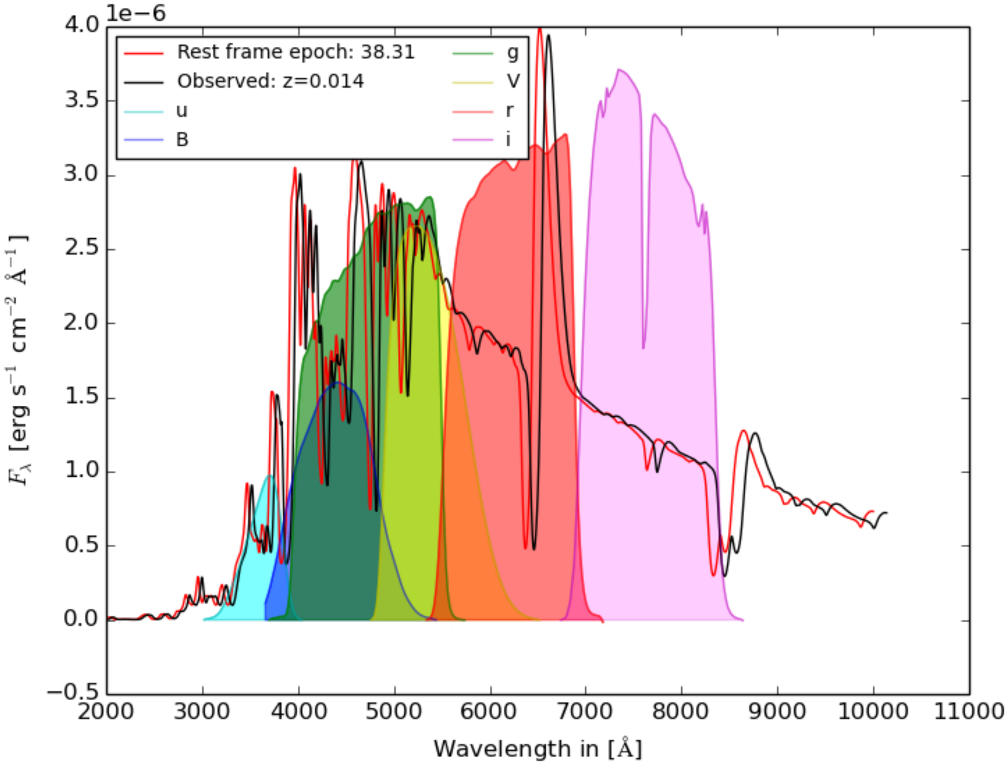

Figure 3.2 (a): The red spectrum shows the theoretical model in the rest frame while the black spectrum is in the observed frame. The $uBgVri$ filter bandpasses are also represented.

3. Step 3: The AKS correction depends on anything that could affect the SED continuum such as for example the host or the Milky Way extinctions. For this reason, the continuum needs to be adjusted to have the same colours as the SN (Hsiao et al., 2007). This step is called Colour-match and it is described below. To match the theoretical spectrum to the observed photometric magnitudes from the SN, I calculate synthetic colours using the theoretical model in the observed frame ($f^{obs}(\lambda)$), and compare them to the observed colours as it is shown in Figure 3.2 (b).

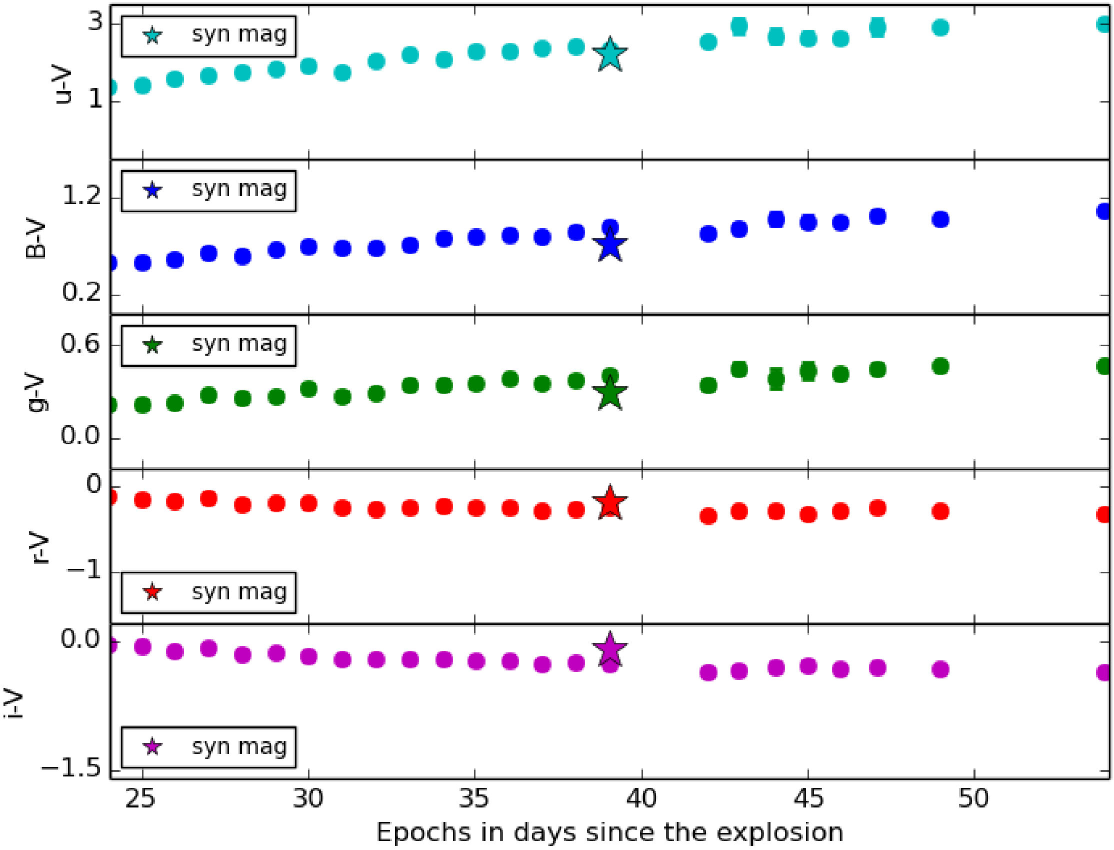

Figure 3.2 (b). Difference between the synthetic colours represented by stars and the observed colours represented by squares.

4. Step 4: In Figure 3.2 (c) we see the correction factors needed to correct the theoretical spectrum in order to match the observed colour. In this figure, the factors are represented for each filter in flux scale. However, because we need to describe the difference between the synthetic colours and the observed colours at every wavelength an analytical function is needed. This analytical function called color-matching (CM) function is shown in black in Figure 3.2 (c) and corresponds to a cubic polynomial interpolation. For the wavelengths outside of the range of filters used I do a constant extrapolation. Then, I apply this CM function to correct the entire theoretical spectrum ($f^{obs}(\lambda)$) and obtain a new spectrum $f^{obs}_{CM}(\lambda) = CM(\lambda) \times f^{obs}(\lambda)$. This correction is done in an iterative way until the difference between the observed colours and the synthetic colours is less than 0.01 mag. As we can see in Figure 3.2 (d), as the end of the matching colour procedure, the observed and the synthetic colours are consistent.

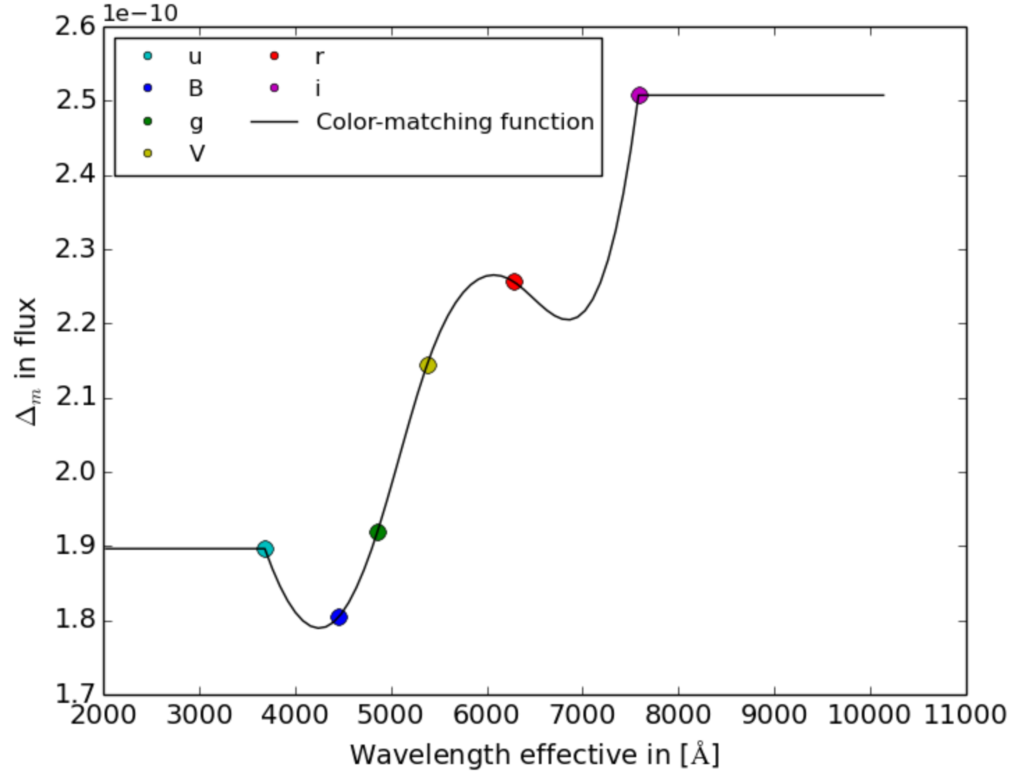

Figure 3.2 (c):

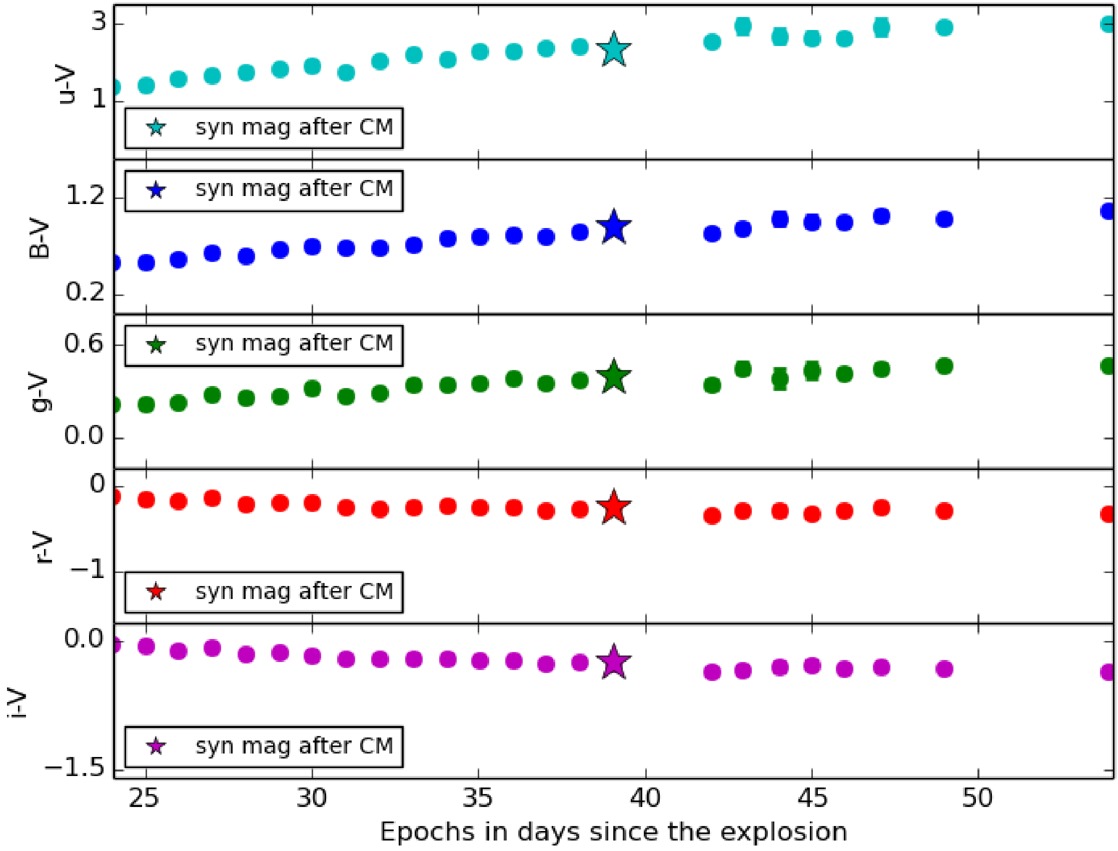

Figure 3.2 (d): Difference between the synthetic colours represented by stars and the observed colours represented by squares after correcting the model continuum using the color-matching function (CM).

5. Step 5: The magnitude in the observer's frame (m_Y^{obs}) can be now computed using the spectrum corrected for the color-matching function. This spectrum is represented in green in Figure 3.2 (e).

$$m_Y^{obs} = -2.5log_{10}\left[\int f_{CM}^{obs}(\lambda)S_Y\lambda d\lambda\right] + ZP_Y \tag{3.11}$$

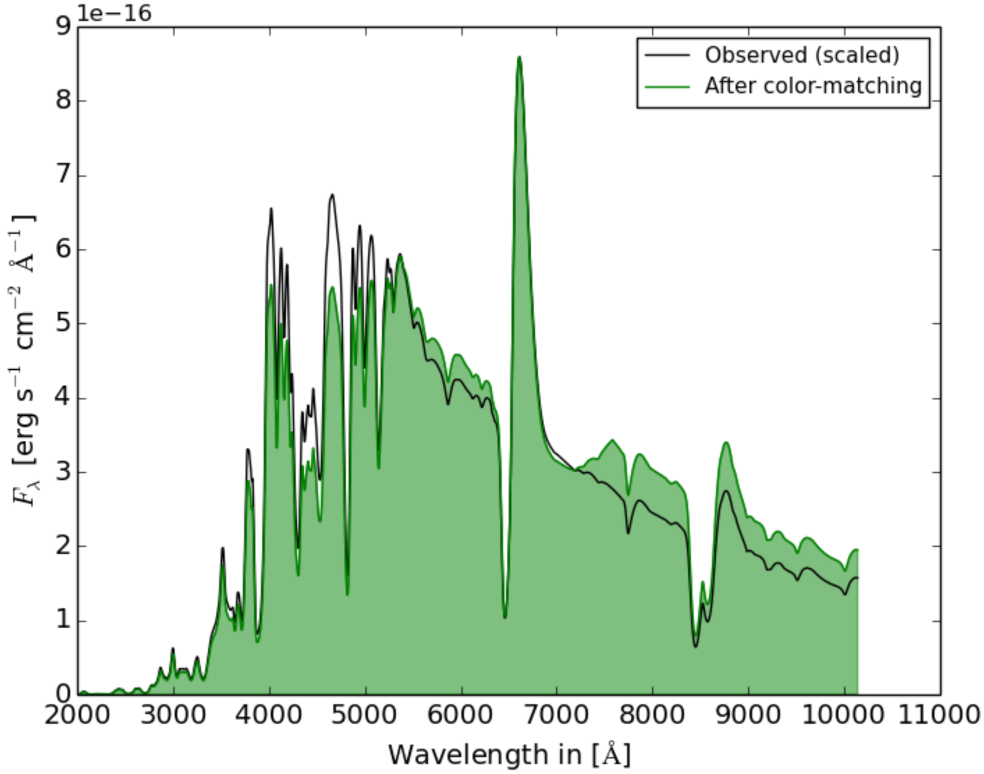

Figure 3.2 (e): Black and green spectra show the theoretical model before and after applying the CM function respectively.

6. Step 6: To derive the AKS we need to derive the magnitude in the rest frame without AvG (M_X^{CSP}). From the green spectrum represented above (f_{CM}^{obs}) and using the CCM89 law, I remove the AvG and bring the unreddened spectrum to the rest frame $f_{CM}^{rest,AvG}(\lambda')$. In Figure 3.2 (f), I show in green the spectrum after colour matching (see step 5) and in magenta the same spectrum but corrected for AvG and redshift. The spectrum in magenta will be used as the SED to derive M_X^{CSP}. The AKS is obtained by taking the magnitude difference obtained with the filled green spectrum and the filled magenta spectrum. I repeat this procedure for all the photometric points and for each band and all the SNe.

The magnitude X in the rest-frame is computed as:

$$M_X^{CSP} = -2.5log_{10} \int f_{CM}^{rest,AvG}(\lambda')S_X^{CSP}\lambda' d\lambda' + ZP_X^{CSP} \tag{3.12}$$

The choice of the filter X depends on the redshift. At low redshift the K-correction is not so important, so X and Y are the same filters, but at higher redshift it is not the case. We need to know in which filter a photon received in the Y filter was emitted. For this, I calculate the effective wavelength of the CSP filters and the one of the filter Y divided by (1+z$_{hel}$). From all the CSP filters (u, g, r, i), the one with the closest effective wavelength will be chosen as the X filters.

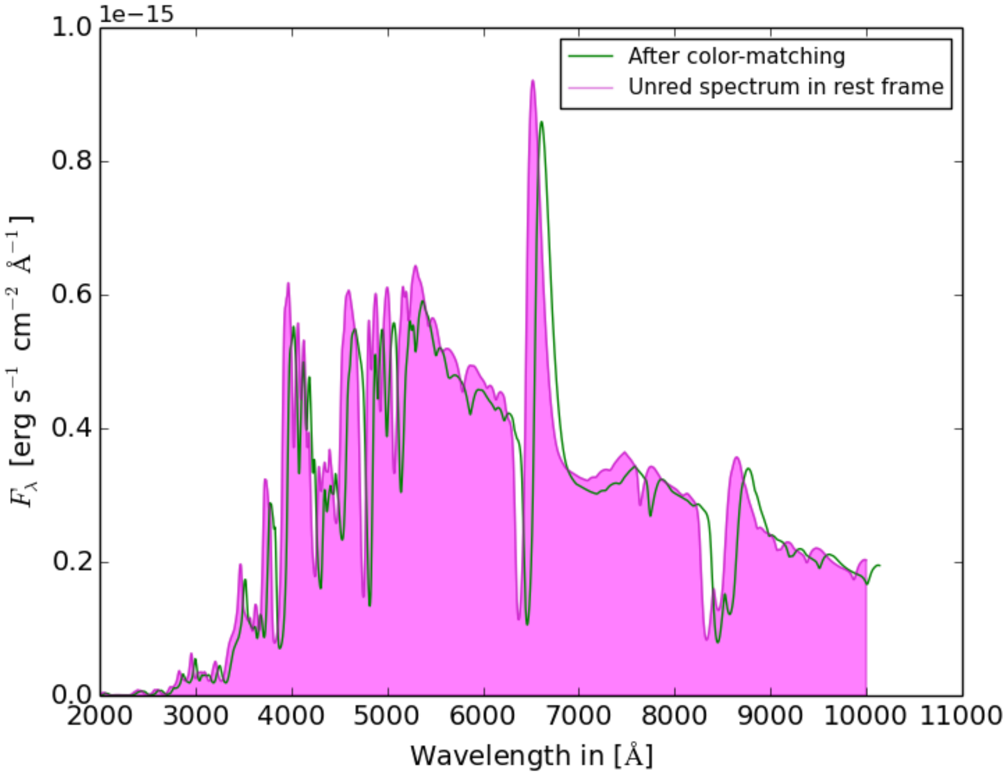

Figure 3.2 (f): Green and magenta spectra show respectively the theoretical model after applying the CM function and the unreddened rest frame spectrum.

Figure 3.2: Procedure to correct for AKS: step by step

Ideally, the AKS correction should be computed using observational spectra and not theoretical models. The advantage of using observed spectra is that we can take into account the differences between the observed SN and the model (SN 1999em). However there are two advantages of using theoretical models. First, we can obtain the AKS for NIR filters (Y, J, H), and secondly, this method does not require observed spectra which are expensive to obtain in terms of telescope time, and virtually impossible to get at higher redshifts.

As a complementary work on the AKS and to validate the method described above I did a comparison between the AKS values obtained using the Dessart et al. (2013) model to those computed from the observed spectra database. In both cases, we use exactly the same procedure described previously. In Figure 3.3 we can see that the AKS values calculated with both methods are very consistent. Both SNe II show peculiar light-curves and spectra.This exercise validates the choice of using the Dessart et al. (2013) models to calculate the AKS.

The AKS corrections are sensitive to the choice of spectral template, thus, in order to estimate the systematic errors, we tried another model: Nugent's templates[3]. These templates are based on the models from Baron et al. (2004).The comparison between Nugent's templates and Dessart's model (Dessart et al., 2013), leads to a mean difference of 0.004 mag in r band (with a standard deviation of 0.02 mag) and 0.03 mag (with a standard deviation of ± 0.06 mag) in i band. It is important to note that both models were created to fit the same observed data (SN 1999em spectra) and a comparison between Dessart's model.

---

[3] `https://c3.lbl.gov/nugent/index.html`

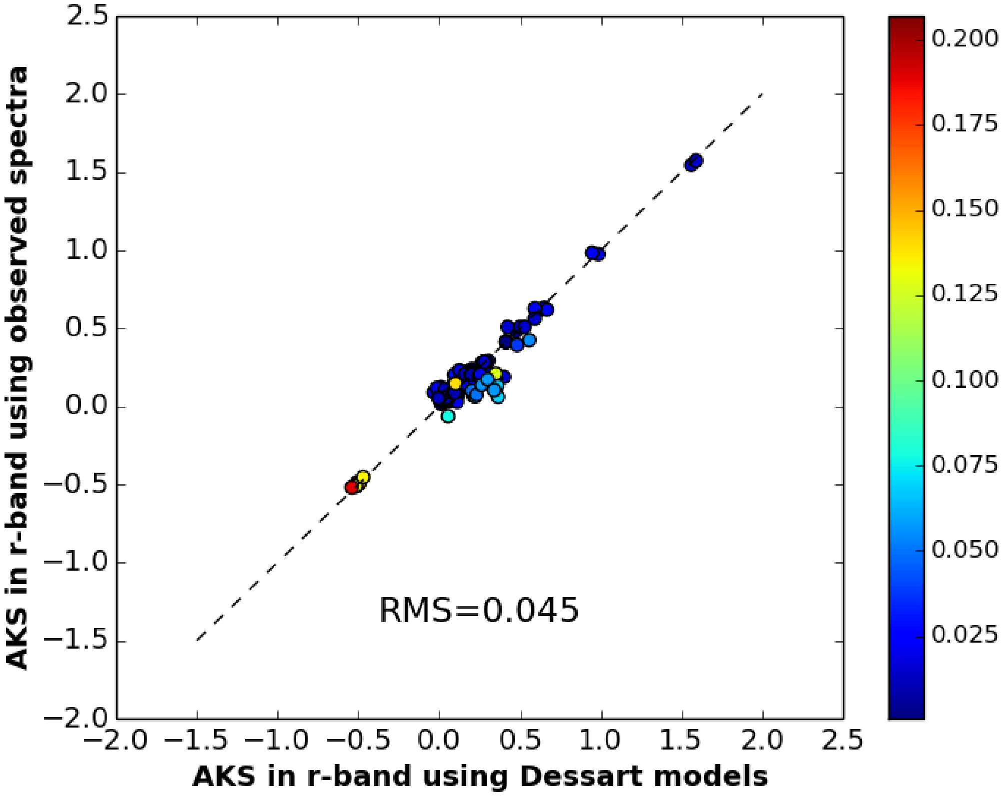

Figure 3.3: Comparison between the AKS calculated using the theoretical models and the observed spectra in the r band for the whole sample. The black dotted line represents x=y. Each circle represents one observed spectrum of our database. The colour bar represents the redshift of the different SNe.

Chapter 4

The Photometric Color Method

Contents

Two years ago, Anderson et al. (2014b) found a correlation between the absolute magnitude at maximum and the second, shallower slope in the light curve after maximum, s_2, which corresponds to the plateau for the SNe IIP (Anderson et al., 2014b). Anderson et al. (2014b) found that more luminous SNe II have higher s_2 (steeper decline) confirming previous studies finding that SNe IIL are more luminous than SNe IIP (Patat et al., 1994; Richardson et al., 2014). To derive the relation between the luminosity and decline rate, Anderson et al. (2014b) used the same SNe II CSP sample used by myself expanded with SNe II from the Carnegie Type II Supernova Program (CATS; PI: Hamuy, 2002-2003, Galbany et al. 2016). In their work, s_2 is measured from the V-band light curves. In Figure 4.1, we show the original relation found by those authors between the absolute magnitude at peak magnitude and s_2. Note that for this relation, the Pearson correlation factor derived is -0.57.

The discovery of this correlation opens up the new possibility to standardise the SNe II using only photometric parameters. In this section, I present a new method to standardise the SNe II called the Photometric Colour Method (PCM): first, in Section 4.2 I calibrate this new method using only the CSP sample de Jaeger et al. (2015b) and second, I extend the Hubble diagram to higher redshift (see Section 4.3 and de Jaeger et al. 2016 submitted). Roughly the same methodology is used for both samples which is explained in Section 4.1.

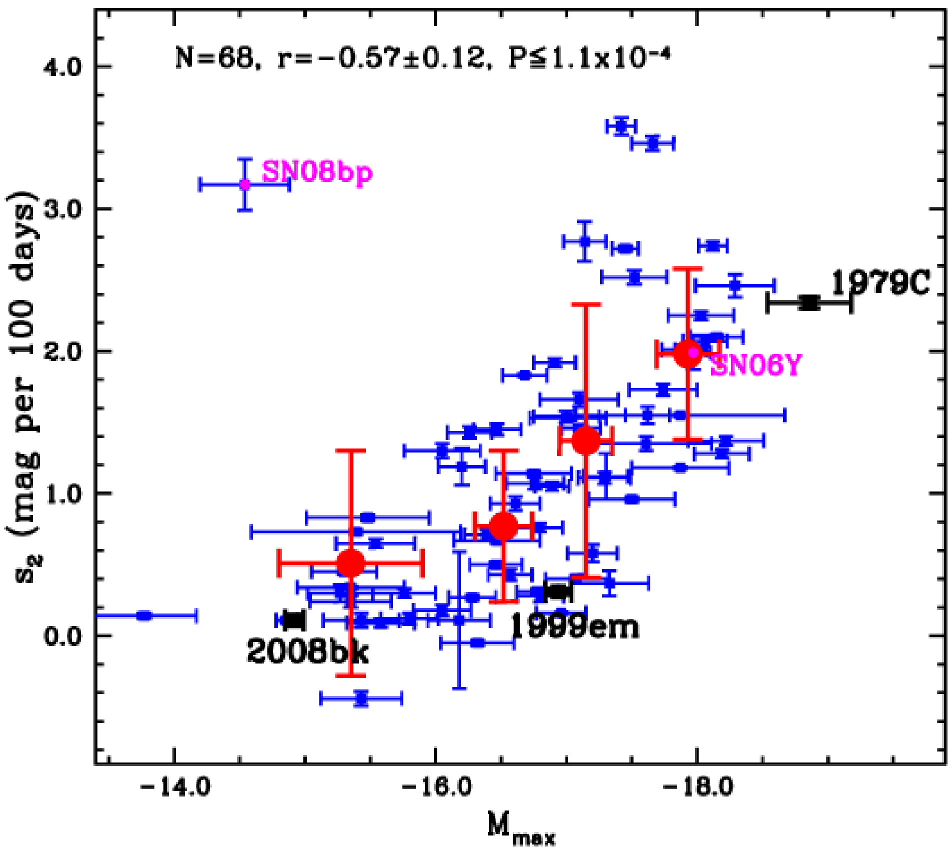

Figure 4.1: Decline rate during the plateau: s_2 plotted against absolute magnitudes at maximum. Individual data points are shown as blue squares. Additionally, a sub-luminous (SN 2008bk), a prototype SNe IIP (SN 1999em) and a prototype SNe IIL (1979C) are noted. Binned data are shown in red circles which its 1 sigma uncertainies.

4.1 Methodology

The basic idea behind this method is to correct and standardise the apparent magnitude using two photometric parameters: the slope of the plateau, and a colour term at a specific epoch (de Jaeger et al., 2015b). As it was described in Section 3, the colour term is mainly used to take into account the dispersion caused by the host-galaxy extinction: redder SNe are fainter. For my work at low redshift (CSP sample only), I first use the s_2 measured by Anderson et al. (2014b) in the V band and try to calibrate the method. Then, for the total sample (CSP+SDSS+SNLS) since I do not have the V band data for all the SNe II (only g, r, and i bands in common) I need to measure the slope in another band. To be consistent and to avoid systematic errors, I decided to measure s_2 for all the SNe II in the same way. To measure s_2 in all the bands I use a Python program, which performs a least-squares fitting of the light-curve correcting for AKS, with one or two slopes (sometimes the first decline called s_1 after the maximum is not visible). To choose between one or two slopes, a statistical F-test is performed. If the best fit is achieved using two slopes, we use the second slope to correct the observed magnitude. The slope is measured in each band (g, r, and i) but only the values used in this work (i band) are listed Table 2.1. In Figure 4.3, I show an example of the fit of the i band light curve with one and two slopes for SN 2006ai. In this case, the best fit is achieved with two slopes. In Figure 4.2, I show the same correlation found by Anderson et al. (2014b) but using my whole sample with low and higher redshift SNe. In this figure, I use the value of s_2 measured using the i-band light-curves. The absolute magnitudes (40 days after explosion in rest frame) were obtained after AKS correction and corrected for the luminosity distances using the ΛCMD model (Ω_M=0.3 and Ω_Λ=0.70). 73 SNe II were available at this specific epoch and filter. I find a similar correlation as that found by Anderson et al. (2014b) with a similar Pearson factor, −0.6.

Using only the CSP sample we derive the V-band light curve slopes and perform a sanity check. By comparing these values with those found by Anderson et al. (2014b) we obtain a very good agreement. Also, an independent work done by Galbany et al. (2016) with 51 SNe II has confirmed the relation found by Anderson et al. (2014b) between s_2 and the absolute magnitude in different bands.

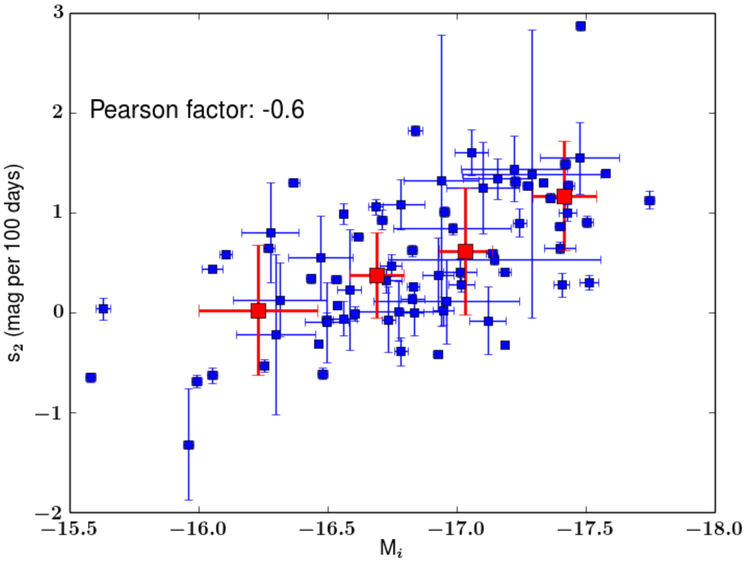

Figure 4.2: Absolute magnitude (i band) 40 days after explosion (rest frame), plotted against the decline rate during the plateau: s_2. 73 SNe from CSP, SDSS and SNLS are represented. Binned data are shown in red squares.

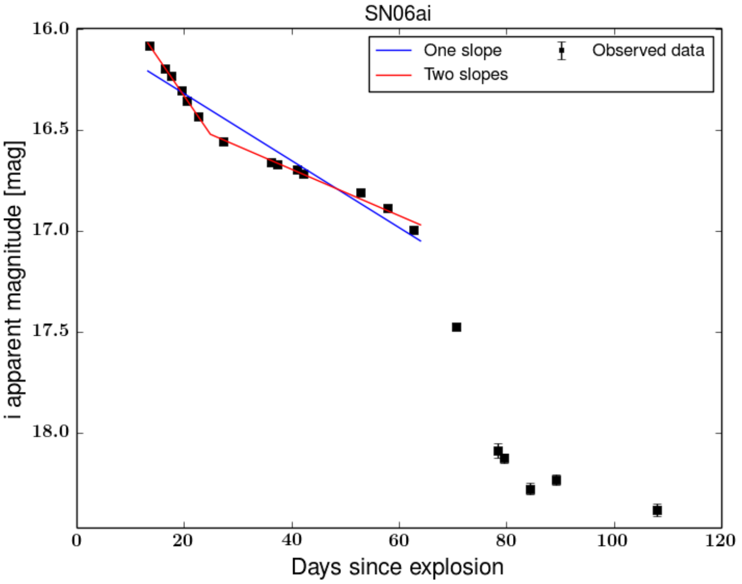

Figure 4.3: Fit of the slope s$_2$. The observed magnitudes in the *i* band for SN 2006ai are shown as black dot. The blue line represents the one line fit, whereas in red we use two lines.

Due to the correlation between the absolute magnitude and these two variables (s$_2$ and colour), the observed magnitudes can be modelled as:

$$\begin{aligned} m_{\lambda 1}^{model} =& M_{\lambda 1} - \alpha s_2 + \beta_{\lambda 1}(m_{\lambda 2} - m_{\lambda 3}) \\ &+ 5log_{10}(d_L(z_{CMB}|\Omega_m, \Omega_\Lambda)) + 25, \end{aligned} \tag{4.1}$$

where $d_L(z_{CMB}|\Omega_m, \Omega_\Lambda)$ is the luminosity distance for a cosmological model depending on: the cosmological parameters Ω_m, Ω_Λ, the CMB redshift z_{CMB}, and the Hubble constant. Note that at low redshift, the luminosity distance is equal to $\frac{cz}{H_0}$. α, β_{λ_1}, and M_{λ_1} are also free parameters with M_{λ_1} corresponding to the absolute magnitude in the filter λ_1 at the same epoch as m_{λ_1}.

Since we do not have in our sample any SN with an accurate distance estimation (e.g. from Cepheid measurements), we only measure relative distances and define the "Hubble Constant free" absolute magnitude as $\mathcal{M}_{\lambda 1}$=M$_{\lambda 1}$-5 log$_{10}$(H$_0$) + 25 and $\mathcal{D}_L$=H$_0 d_L$ as done in many previous works (Perlmutter et al., 1999; Nugent et al., 2006; Poznanski et al., 2009; D'Andrea et al., 2010). The apparent magnitude is finally written as:

$$\begin{aligned} m_{\lambda 1}^{model} =& \mathcal{M}_{\lambda 1} - \alpha s_2 + \beta_{\lambda 1}(m_{\lambda 2} - m_{\lambda 3}) \\ &+ 5log_{10}(\mathcal{D}_{lum}(z_{CMB}|\Omega_m, \Omega_\Lambda)), \end{aligned} \tag{4.2}$$

From this equation, one can derive by fitting, α, β_{λ_1} and $\mathcal{M}_{\lambda 1}$ and the cosmological parameters Ω_m, Ω_Λ. In order to take into account our imperfect knowledge of the SNe II physics and the intrinsic scatter, another free parameters named σ_{int} needs to be added. This free parameter represents the intrinsic scatter not accounted for measurement errors and it is the minimum statistical uncertainty in any distance determination using PCM.

In cosmology, when we compare observations to predictions of a parameter-dependent model, Bayesian inference is the standard procedure. The Bayes theorem is defined as:

$$p(\vec{\theta})|d) \propto p(\vec{\theta})p(d|\vec{\theta}) \tag{4.3}$$

where $p(\vec{\theta}|d)$ is the posterior probability distribution function (PDF) for $\vec{\theta}$ the set of parameters and d the observed data. $p(d|\vec{\theta})$ is the likelihood of the data given the parameters, $p(\vec{\theta})$ is the prior PDF. Explicitly, this approach tells us how to update our knowledge from a prior distribution to a new probability density called posterior. Thus, to define the posterior probability distribution one needs to define a likelihood function and a prior function.

We assume that each measured distance modulus has a probability distribution described by a Gaussian. If the distance observations are independent after calibration (no correlated uncertainties) we can simply multiply the likelihood of each observation together and take the logarithm to write the likelihood as it was defined by D'Andrea et al. (2010):

$$-2ln(\mathcal{L}) = \sum_{SN} \left\{ \frac{\left[m_{\lambda 1}^{obs} - m_{\lambda 1}^{model}\right]^2}{\sigma_{tot}^2} + ln(\sigma_{tot}^2) \right\}, \tag{4.4}$$

where we sum over all the SNe available for one specific epoch, $\mathrm{m}_{\lambda 1}^{obs}$ is the observed magnitude corrected for AKS, $\mathrm{m}_{\lambda 1}^{model}$ the model defined in equation 4.2 and the total uncertainty σ_{tot} is defined as:

$$\begin{aligned} \sigma_{tot}^2 =& \sigma_{m_{\lambda 1}}^2 + (\alpha\sigma_{s2})^2 + (\beta\sigma_{(m_{\lambda 2} - m_{\lambda 3})})^2 \\ &+ \left(\sigma_z \frac{5(1+z)}{z(1+z/2)ln(10)}\right)^2 + \sigma_{int}^2 \end{aligned} \tag{4.5}$$

For the relation between the redshift uncertainty and the associated magnitude uncertainties, we use the empty Universe approximation (Conley et al., 2011). The second logarithmic term comes from the Gaussian distribution normalisation factor and it is useful in order to not obtain large values of α, β, and $\mathcal{M}_{\lambda 1}$ which could be favoured by the first part of the log-likelihood. Note that this term does not significantly change the resulting best-fit parameters (Poznanski et al., 2009).

The prior function could be broad or informative depending on the constraints on the free parameters. I decided to put some limits for our prior and defined it to have uniform probability for $0 \leq \Omega_m \leq 1$, $0.1 \leq \sigma_{int} \leq 0.9$, α, β, $\mathcal{M}_{\lambda 1} \neq 0$, but otherwise has zero probability.

For exploring the posterior probability density, a Monte Carlo Markov Chain simulation (MCMC) is performed. The MCMC calculation is run using a Python package called EMCEE developed by Foreman-Mackey et al. (2013). This method is very powerful and allows us to quantify the uncertainties of the underlying set of model parameters when we do not necessarily know the shape or scale of their respective distributions. A random-walk algorithm is used to perturb all the parameters a bit from a initial state and then determine whether this new model is better or worse. Through this acceptance process, we build a "chain" of states that can be used to create parameter distributions. Two approaches can be used. The walkers could start in a reasonable range in parameters or they start in a very tight N-dimensional ball in a parameter space around one point, point chosen to be close to the maximum probability point. Here, I choose the second option, walkers start a position close to the values obtained by the likelihood minimisation. First I will derive the fitting parameters by minimising the likelihood function and find the maximum probability point and then I will run a MCMC to explore the space parameter starting very close from the maximum probability point. Even if the first option looks more objective, there is more chance that the walkers get stuck in low probability modes of a multi-modal probability landscape, that is why we privileged the second option (Foreman-Mackey et al., 2013). An important input in the MCMC simulations is the number of walkers and the number of steps. The more walkers used the better the simulation is, but if we double the number of walkers, each step takes twice as much computing time. Taking into account this, I decided to use 500 walkers and 1000 steps. Note that the EMCEE package uses an ensemble of walkers which can be moved in parallel and not a single iterative random walker (Goodman-Weare algorithm versus Metropolis-Hastings algorithm).

4.2 Low redshift Hubble diagram

In this Section, I show the first part of my thesis. The main goal of this first part is to deal only with the CSP data and to calibrate the PCM. I start with this sample because the majority of the SNe arises from the CSP sample and are high quality data. Finally, one of the most important advantages of the CSP sample is the NIR photometry. In the literature, there is not such a sample of NIR light curves. This allows us to compare the optical and NIR Hubble diagram and see the effects of host galaxy extinction which are normally more important at shorter wavelengths. In this part, I only use the SNe in Table 2.1 with photometry data in g, r, i , Y, J, H, B, and V filters (SNe II with a note mark). Thus, the sample for this part is composed of 50 SNe II.

The net motions of galaxies are comprised of the Hubble flow, the local flow, and the motion of the galaxy within its own cluster and/or group environment. The Hubble flow describes the motion of galaxies due solely to the expansion of the Universe, for this reason, in order to avoid peculiar host galaxy motions, I select only SNe II located in the Hubble flow, i.e., with $cz_{CMB} \geq 3000$ km s^{-1} . Our available sample is composed of 39 SNe II. Due to the high data quality, we have a large set of combinations (magnitudes, colours, epoch) to derive the Hubble diagram using the PCM. Thus, the first step is to define the best epoch, the best colour, and the best magnitude, i.e., those which minimise σ_{int} or the Root Mean Square in the Hubble diagram. In this part I do not perform a MCMC simulation, but only a likelihood minimisation where the likelihood is the same defined in equation 4.4 but the model differs from 4.2. At low redshift the luminosity distance is cosmological parameters independent, that is why I approximate the luminosity distance by cz in equation 4.2. Note that the RMS is thus derived around this straight line.

First, to explore different epochs I start by linearly interpolating colours on a daily basis from colours observed at epochs around the epoch of interest. Using the same procedure, I also interpolate the observed magnitudes. Both quantities are interpolated after AKS corrections. SNe II are supposedly under similar physical conditions (e.g. temperature) when they arrive towards the end of the plateau (Hamuy & Pinto, 2002) that is why I use the end of the optically thick phase measured in the V band (as defined by Anderson et al. 2014b) as the time origin in order to bring all SNe II to the same time scale. Note that, when the end of the plateau is not available I choose 80 days post explosion, which is the average value for the CSP sample. Given that SNe II show a significant dispersion in the plateau duration driven by different evolution speeds, we decide to take a fraction of the plateau duration and not an absolute time, to ensure that we compare SNe II at the same evolutionary phase. Thus, in the following analysis, I adopt OPTd*X% as the time variable where OPTd is the optically thick phase duration and X is a percentage ranging between 1-100%.

Second, I use the minimisation of dispersion in the Hubble diagram as my figure of merit to find the best combination of possible colour and epoch. To achieve this, I will firstly fix the colour and vary the epoch from OPTd*20% to OPTd*100% for all the filters available. In Figure 4.4, I present the variation with evolutionary phase of the dispersion in the Hubble diagram using the filters available and the $(V-i)$ colour. The lowest root mean square (RMS) values in the optical is found for the r band, and in the NIR part for the Y/J band. Note that the coverage in the Y band is better than in the J band hence, hereafter I use the Y band.

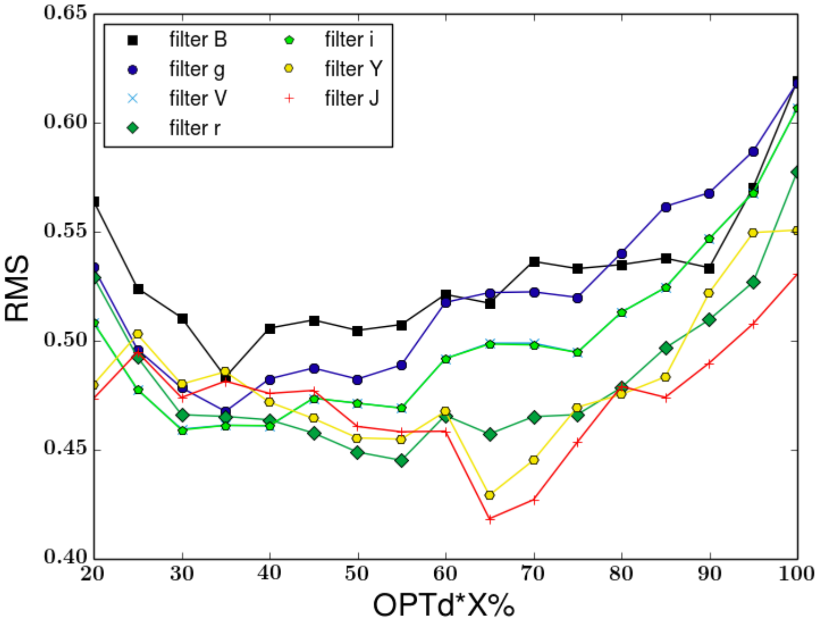

Figure 4.4: Variation in phase of the dispersion in the Hubble diagram for different filters and using a colour term $(V-i)$. In the x-axis we present the time as (explosion time+OPTd*X%). The black squares present the B band, dark blue circle the g band, blue cross the V band, dark green diamonds the r band, green hexagons for the i band, yellow pentagons for the Y band, red plus symbol for the J band. The H band is not presented because the sampling is as good as it is in the other bands.

Now that we find the best filter for the optical and for the near-infrared, we need to find the best colour. As achieved previously, this time I fix the filter and vary the colour. In Figure 4.5, I show variation with evolutionary phase of the dispersion in the Hubble diagram for a fixed magnitude (r band) using different colours. This figure shows that the colour that minimises the RMS is $(V - i)$ ($(r - J)$ yields a lower dispersion but the time coverage is significantly lower). For this reason, I decide to combine the r band and the $(V - i)$ colour for the Hubble diagram. Note also that the best epoch for the r band is close to the middle of the plateau, 55% of the time from the explosion to the end of the plateau, whereas in the Y band is later in phase post explosion, around 65%. In general the best epoch to standardise the magnitude is between 60–70% of the OPTd for NIR filters and for optical filters between 50–60% of OPTd. Physically these epochs correspond in both cases approximately to the middle of the plateau. Note that I tried another time origin such as the epoch of maximum magnitude instead of the end of the plateau but changing the reference does not lower the RMS.

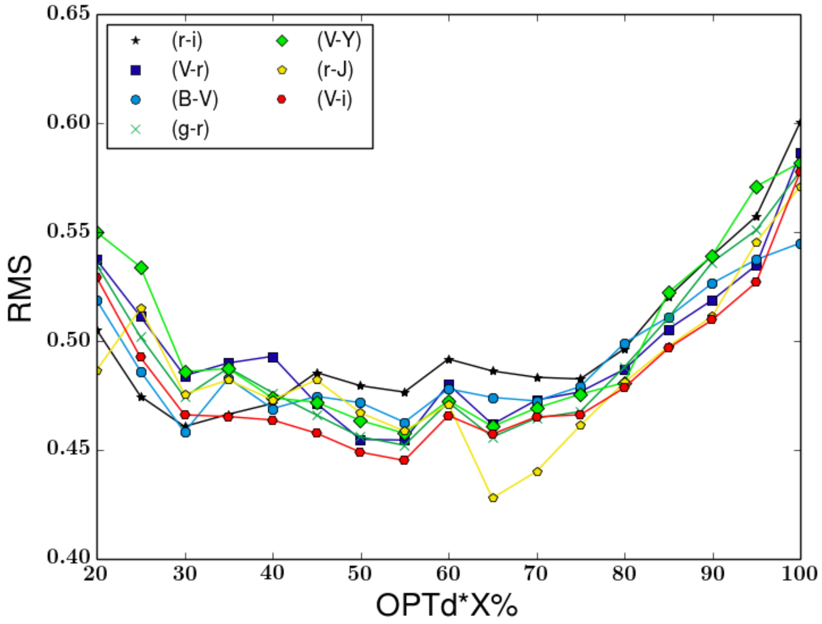

Figure 4.5: Variation in phase of the dispersion in the Hubble diagram using the r band and different colours. In the x-axis we present the time as the OPTd*X%. The black stars present $(r-i)$ colour, dark blue squares are for $(V-r)$, blue circle $(B-V)$, cyan cross $(g-r)$, green diamonds $(V-Y)$, yellow pentagons for $(r-J)$, and red hexagons for $(V-i)$.

Now that we have defined the best combination of colour, filter, and epoch we are prepared to derive the SNe II Hubble diagram. For this, we minimise the likelihood defined in equation 4.4 in order to derive the fitting parameters. In Figure 4.6 and Figure 4.7, I present the first Hubble diagram based entirely on photometric data using s_2 (measured in the V band by Anderson et al. 2014b) and colour term for two filters, r band and Y band respectively.

For the r band and the specific epoch OPTd*0.55, 37 SNe II were available. The intrinsic dispersion with only AKS correction is 0.56 mag. Thanks to the s_2 correction, the scatter drops to 0.46 mag and then adding the colour term drops to 0.41 mag. This dispersion allows us to derive distances with an accuracy of $\sim$ 20%. If I do not select only the SNe II in the Hubble flow (48 SNe available), the scatter drops from 0.64 mag to 0.45 mag after correction.

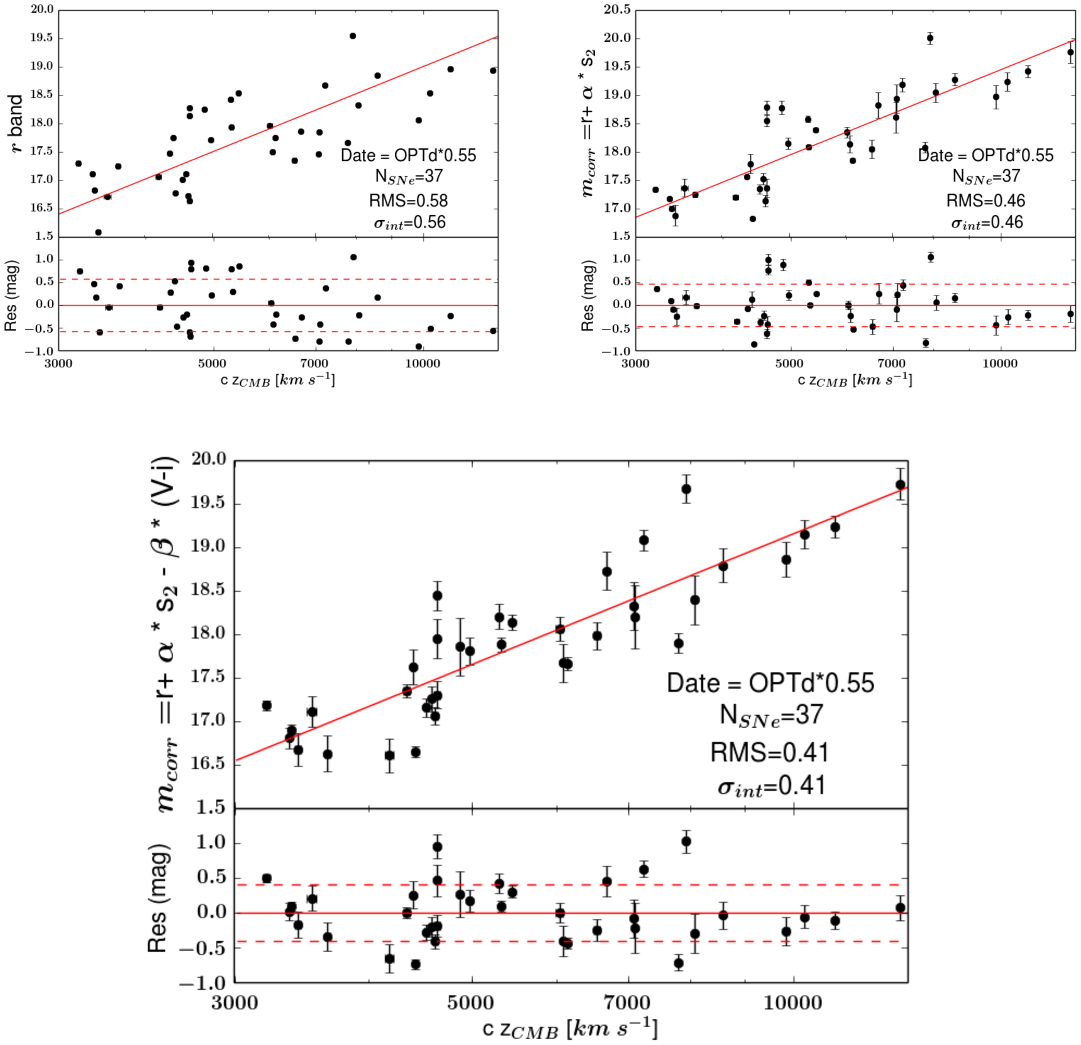

Figure 4.6: In the figures, we present the dispersion (RMS) using the PCM, the number of SNe (N_{SNe}), the epoch chosen with respect to OPTd (OPTd*X%) and the intrinsic dispersion (σ_{int}) for our Hubble flow sample. On the bottom of each plot, the residuals are shown. In all the residual plots, the dashed line corresponds to σ_{int}. *Top Left panel:* Apparent magnitude corrected for AKS in the r band plotted against cz_{CMB}; *Top Right panel:* Apparent magnitude corrected for AKS and s_2 term in the r band plotted against cz_{CMB}. *Center panel:* Apparent magnitude corrected for AKS, s_2 term in the r band, and by colour term, $(V-i)$ plotted against cz_{CMB}.

Using the Y band at an epoch of OPTd*0.65 only 30 SNe II in the Hubble flow were available. The intrinsic dispersion ends up to be 0.40 mag after all the corrections. As we can see, the colour term is more important for the optical filter than for the NIR filter as expected. Indeed, for the r band the RMS decreases from 0.46 to 0.41 mag when the colour term is added whereas for the NIR filter the improvement is only of 0.01 mag. This is not surprising because this term is probably related to host-galaxy extinction which is more prevalent at optical wavelengths than in the NIR, so adding a colour term for NIR filters does not significantly influence the dispersion.

In SNe II cosmology, in general the authors used slow-declining SNe II (SNe IIP), that it why I did some analysis of the SNe II to see if any of the higher residuals arise from intrinsic SNe II properties. The overall conclusion is that at least to first order, SNe II intrinsic differences (s_2, OPTd,...) are not contributing significantly to the dispersion, so this suggests that SNe within the full range of s_2 values should be included in Hubble diagrams produced with SNe II.

Following the work of Folatelli et al. (2010) for SNe Ia, I also investigated the combined Hubble diagram using all the filters available. For each band, i.e., $BgVriYJ$, I derive a Hubble diagram running the procedure described above and then, I average the distance moduli derived in each filter. In Figure 4.8 the top panel shows this combined Hubble diagram in black versus a r-band Hubble diagram in red. The dispersion obtained using this combined Hubble diagram is not much better than the dispersion derived in the individual filters. The explanation of this is found in the bottom panel of Figure 4.8. In the bottom panel, I show the distance modulus residual in B band versus the others bands (g, V, i, i, Y, and J). A significant correlation is observed between the residual in one band versus those in another bands, with a dispersion $\sim$ 0.2 mag on average. For this reason, the combined Hubble diagram do not reduce the intrinsic scatter in the diagram as compared with the Hubble diagram using the individual band. Note that the residual is derived using the colour $(V-i)$.

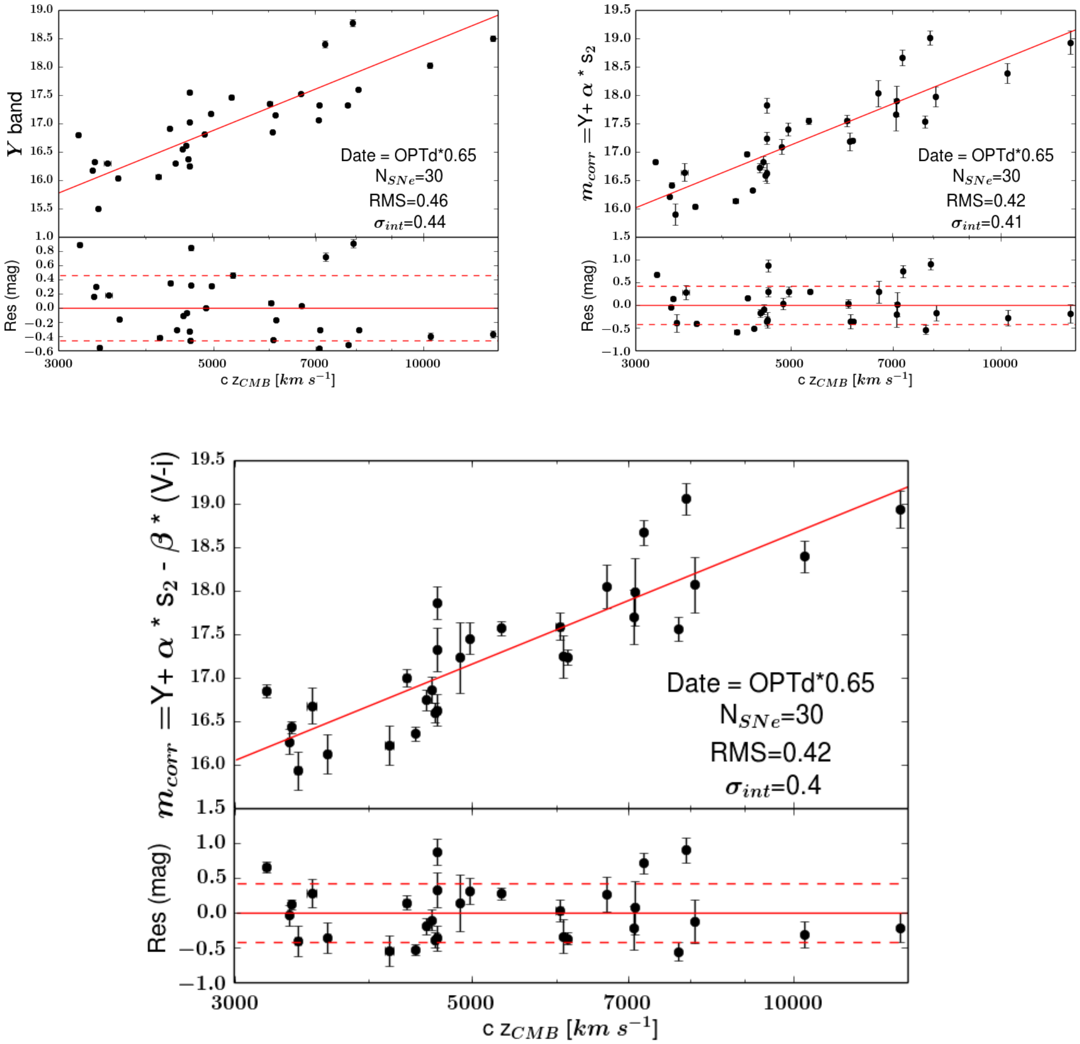

Figure 4.7: In the figures, we present the dispersion (RMS) using the PCM, the number of SNe (N_{SNe}), the epoch chosen with respect to OPTd (OPTd*X%) and the intrinsic dispersion (σ_{int}) for our Hubble flow sample. On the bottom of each plot, the residuals are shown. In all the residual plots, the dashed line corresponds to the σ_{int}. *Top Left panel:* Apparent magnitude corrected for AKS in the Y band plotted against cz_{CMB}; *Top Right panel:* Apparent magnitude corrected for AKS and s_2 term in the Y band plotted against cz_{CMB}. *Center panel:* Apparent magnitude corrected for AKS, s_2 term in the Y band, and by colour term, $(V-i)$ plotted against cz_{CMB}.

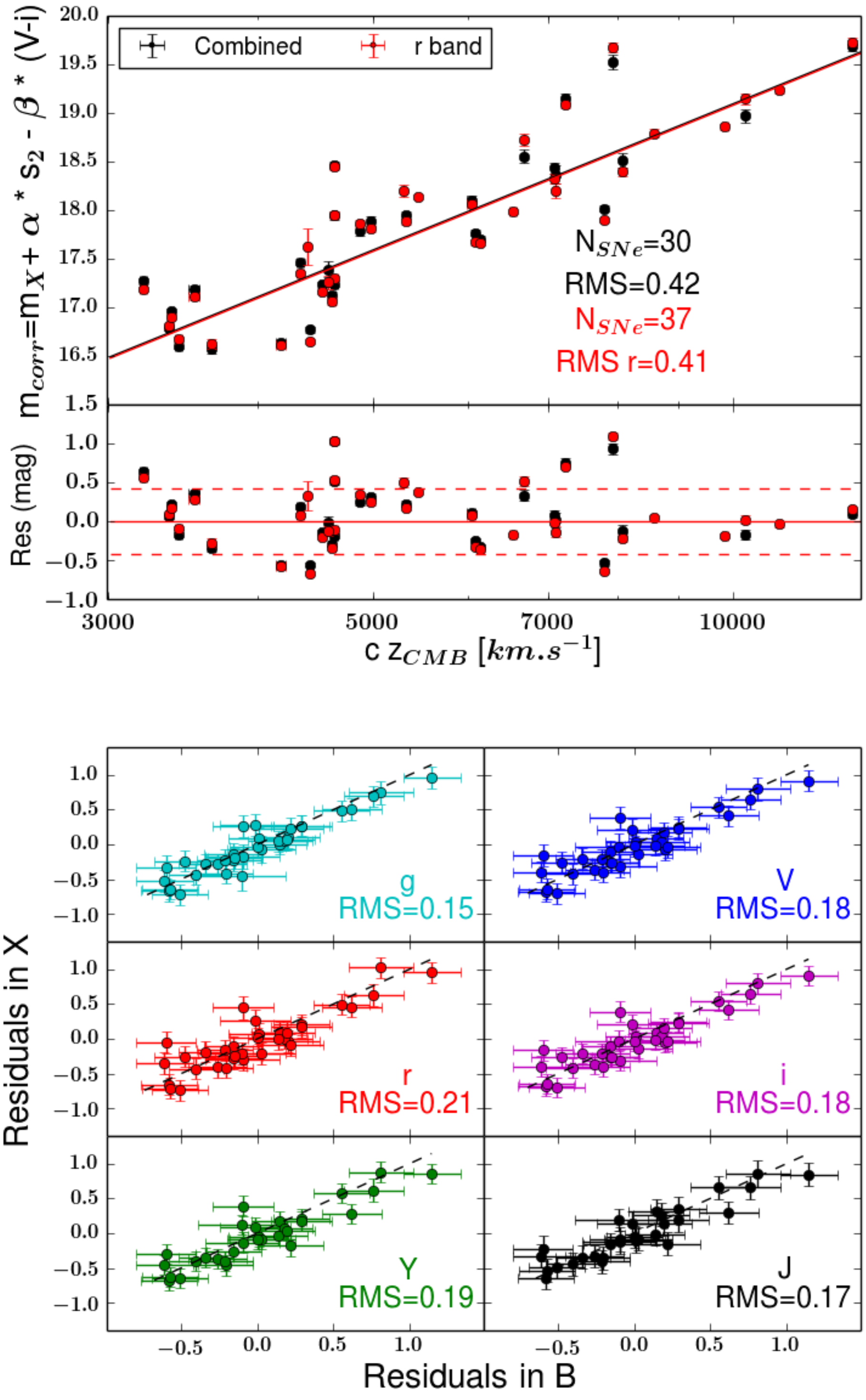

Figure 4.8: *Top panel:* Combined Hubble diagram obtained by averaging the distance moduli derived in each filter ($BgVriYJ$). Red dots represent one single filter (r) Hubble diagram whereas the black dots are for the combined Hubble diagram. *Bottom panel:* Residuals in the distance moduli calculated in band X, where X=u, g, r, i, Y, J, plotted versus the residuals in the B-band distance moduli. The black dashed line represents x=y.

We also tried to use two different epochs, one for the magnitude and another one for the colour but, again, this does not improve the RMS. Note that if we use the weighted root mean square (WRMS) as defined by Blondin et al. (2011) we find 0.39 mag and 0.38 mag for the r band and Y band, respectively, after s_2 and colour corrections.

Finally, I tried to use a golden sample to reduce the scatter. A significant fraction (60 %) of values from Anderson et al. (2014b) does not correspond to the slope of the plateau but sometimes to a combination of s_1 (initial decline) and s_2. Indeed, for some SNe, it was impossible to distinguish two slopes and the best fit was only one slope. For this reason, I defined a new sample composed only of 11 SNe with values of s_1 and s_2 available and with $cz_{CMB} \geq 3000$ km s^{-1}. From this sample and using the $r/(V-i)$ combination I obtain a dispersion of 0.32 mag, which compares to 0.41 mag from the entire sample. From the Y band the scatter decreases to a final dispersion of 0.18 mag for only 8 SNe II. However, these low values should be taken with caution due to possible statistical effects which are discussed later (see Section 6.1.3).

To conclude the low redshift part, I want to highlight the importance of this sample. The low redshift SNe II sample is primordial in SNe cosmology. At low redshifts the cosmological models depend solely on the Hubble constant, and the luminosity distance can be written as:

$$D_{lum}(z_{CMB}) = \frac{v}{H_0} = \frac{cz}{H_0} \tag{4.6}$$

If at least in the SNe II sample, one SN II has a known modulus distance from Cepheid (μ), we can derive/calibrate the Hubble constant which is defined as:

$$\begin{aligned}
&General\ formula: \\
m - M &= \mu = 5log_{10}(cz) - 5log_{10}(H_0) + 25 \\
&Applying\ the\ PCM: \\
m + \alpha s_2 - \beta \times Colour &= 5log_{10}(cz) + \mathcal{M} \quad (\mathcal{M} = M - 5log_{10}(H_0) + 25) \\
m + \alpha s_2 - \beta \times Colour + 5log_{10}(H_0) &= 5log_{10}(cz) + \mathcal{M} + 5log_{10}(H_0) \\
5log_{10}(H_0) &= m + \alpha s_2 - \beta \times Colour - 5log_{10}(cz) + 5log_{10}(H_0) - \mathcal{M} \\
-\mu + 25 &= -5log_{10}(cz) + 5log_{10}(H_0) \\
5log_{10}(H_0) &= m + \alpha s_2 - \beta \times Colour - \mu + 25 - \mathcal{M} \\
H_0 &= 0.2 \times 10^{[m + \alpha s_2 - \beta \times Colour - \mu + 25 - \mathcal{M}]}
\end{aligned} \tag{4.7}$$

where, α, β, and $\mathcal{M}$ are the free parameters derived using the likelihood minimisation. m and μ are known values, so it is easy to derive the Hubble constant. Unfortunately, in my low redshift sample none of the SN II had exploded in a galaxy with Cepheid measurements, thus in this thesis I am not able to estimate the Hubble constant. Note that we cannot use the Tully-Fisher relation (luminosity strongly correlated with the maximum rotation velocity of the galaxy) to derive distance because the Tully-Fisher distances show a significant scale-error with the Cepheid distances being underestimated by 22 ±5.2% (Shanks et al., 2002). In Figure 4.9, I show the comparison between both distances. We clearly see the mismatch between the two methods which prevents the use of the Tully-Fisher distances for the Hubble constant determination.

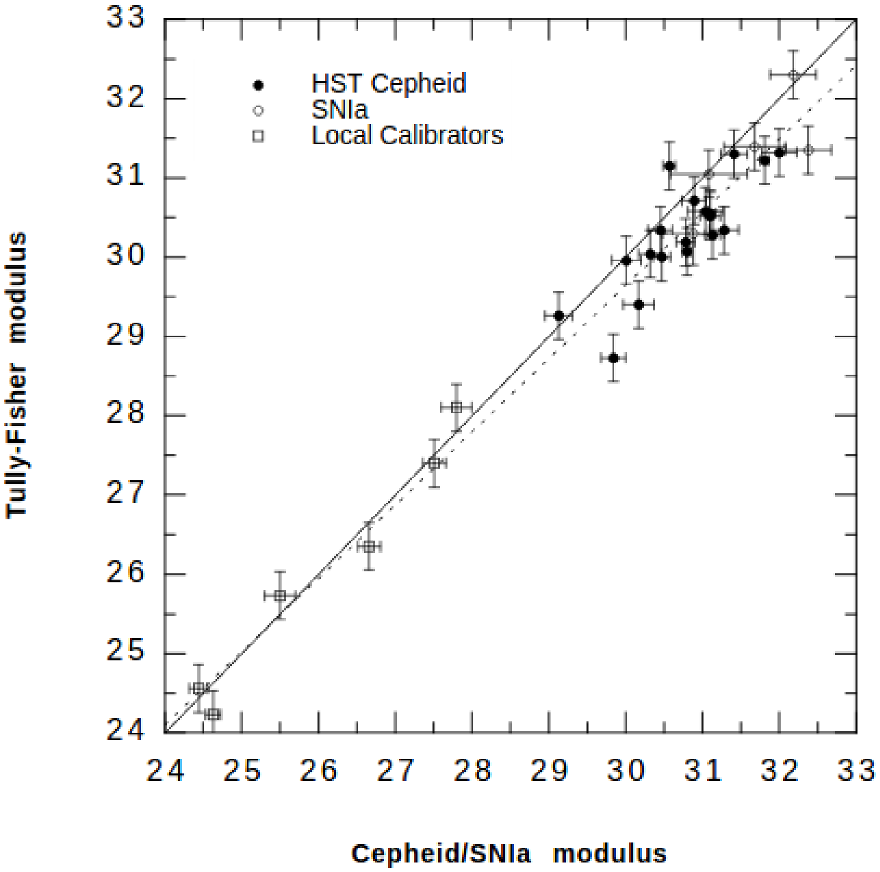

Figure 4.9: Comparison of I-band Tully-Fisher distances with HST Cepheid distances from Shanks et al. (2002).

4.3 High redshift Hubble diagram using the PCM

The estimation of cosmological parameters passes through the observation of more distant SNe II. The predicted differences between cosmological models are extremely small. To discriminate among them will require observed data extending far back in time. In this section, I propose to extend the Hubble diagram derived above to higher redshifts using my entire SNe II sample available, i.e., CSP+SDSS+SNLS samples and then to estimate the cosmological parameters.

In this entire sample, I have 105 SNe II but as mentioned in the previous section, I select only the SNe II in the Hubble flow: $cz_{CMB} \geq 3000$ km s^{-1}. After this cut, the SNe II number drops to 89 SNe II. Thus, the sample used for the high redshift Hubble diagram is composed of 45 SNe II from CSP, 16 SNe II from SDSS and 28 SNe II from SNLS.

The major difference between the low and the higher redshift methods is the reference epoch. Unlike in the previous section, we cannot choose the end of the plateau as reference, due the difficulty to define the OPTd for the higher redshift SNe II. Hence, I decide to use the explosion date as the reference as it will be done with the SCM.

4.3.1 Fixed cosmology

First, before deriving cosmological parameters we want to see if my technique can be extended at higher redshifts. So, as a first step, I attempted to derive the best Hubble diagram (less scatter) for a fixed cosmology and compare the intrinsic scatter with that obtained at low redshifts. For this, I assume a fiducial ΛCDM model, i.e., a flat Universe (Ω_m+Ω_Λ=1) with $\Omega_m = 0.3$ and $\Omega_\Lambda = 0.7$. I also assume a Hubble constant of 70 km s^{-1} Mpc^{-1}.

For the entire sample we have only three filters in common, g, r, and i. Following the same procedure used at low redshifts, I obtained the best Hubble diagram using the combination of the (r-i) colour associated with the i band for an epoch of rest-frame day 40 after explosion. In Figure 4.10, I present the final Hubble diagram using the PCM. For the 73 SNe in the Hubble flow available at this epoch and filters combination, I obtain an intrinsic scatter of 0.35 mag, i.e., 16% in distance errors. The use of the PCM allows us to reduce the intrinsic scatter from 0.57 mag (raw magnitudes) to 0.35 mag. This scatter is somewhat better than that found by de Jaeger et al. (2015b) especially for the higher redshift SNe II (0.4-0.44 mag). The Bayesian inference procedure using the likelihood defined in equation 4.4 gives $\alpha = 0.35^{+0.07}_{-0.06}$, $\beta = 0.83^{+0.29}_{-0.30}$, $\mathcal{M}_{\lambda 1} = -0.89^{+0.05}_{-0.05}$. Using only the CSP sample as done in de Jaeger et al. (2015b) we find $\alpha = 0.39^{+0.08}_{-0.07}$, $\beta = 0.80^{+0.47}_{-0.48}$, $\mathcal{M}_{\lambda 1} = -0.84^{+0.08}_{-0.08}$. From $\mathcal{M}_{\lambda 1}$ and with H_0=70 km s^{-1} Mpc^{-1} an absolute magnitude M$_i$ of -16.66$^{+0.06}_{-0.05}$ mag is obtained. This value is relatively low compared to the absolute magnitude published in Richardson et al. (2014), but can be explained by the fact that we did not correct the colour for the intrinsic colour $(m_{\lambda 2} - m_{\lambda 3})_{int}$. In the following equations, we show the relation between Avh, the colour excess and the intrinsic colour:

Table 4.1. PCM-fit Parameters

Data Set	α	β	M_i	σ_{int}	SNe
CSP	$0.39^{+0.08}_{-0.07}$	$0.80^{+0.47}_{-0.48}$	$-16.58^{+0.06}_{-0.05}$	$0.40^{+0.05}_{-0.04}$	42
CSP+SDSS-II	$0.37^{+0.07}_{-0.07}$	$0.81^{+0.38}_{-0.38}$	$-16.62^{+0.06}_{-0.07}$	$0.38^{+0.04}_{-0.03}$	57
CSP+SNLS	$0.33^{+0.06}_{-0.07}$	$0.87^{+0.35}_{-0.36}$	$-16.61^{+0.06}_{-0.06}$	$0.37^{+0.04}_{-0.03}$	58
SDSS-II+SNLS	$0.23^{+0.09}_{-0.09}$	$0.67^{+0.38}_{-0.37}$	$-16.75^{+0.07}_{-0.06}$	$0.26^{+0.05}_{-0.04}$	31
CSP+SDSS-II+SNLS	$0.35^{+0.07}_{-0.06}$	$0.83^{+0.29}_{-0.30}$	$-16.66^{+0.06}_{-0.05}$	$0.36^{+0.03}_{-0.03}$	73

Note. — Best-fit values and the associated errors for each parameter of the PCM fit and using different samples.

$$\begin{aligned} A_{\lambda 1} =& \beta_{\lambda 1} \times E(m_{\lambda 2} - m_{\lambda 3}) \\ &= \beta_{\lambda 1} \times (m_{\lambda 2} - m_{\lambda 3}) - \beta_{\lambda 1}(m_{\lambda 2} - m_{\lambda 3})_{int} \\ &= \beta_{\lambda 1} \times (m_{\lambda 2} - m_{\lambda 3}) + constant. \end{aligned} \tag{4.8}$$

Thus, the intrinsic colour is degenerate with $\mathcal{M}_{\lambda 1}$ ($\mathcal{M}_{\lambda 1}$=$\mathrm{M}_{\lambda 1}$-5 $\log_{10}(\mathrm{H}_0)$ + 25), so any approximation (we assume that the intrinsic colour is zero) on this value has consequences in the absolute magnitude determination. Note that the β_{λ_1} colour term found lead to lower total-to-selective extinction ratio than for the Milky Way (see Section 6.1.4).

Systematic errors coming from the SN II sample at different redshift are investigated by looking at the evolution of fitted parameters evolution for the different samples, i.e., CSP, CSP+SDSS-II, CSP+SNLS, SDSS-II+SNLS, and CSP+SDSS-II+SNLS. In table 4.1 a summary of these values is shown. As it is seen in this table, the fitting parameters remain similar within the uncertainties for the different samples, which means that there does not seem to be a systematic effect caused by redshift or SNe II sample evolution. We can also study how the parameters are affected by photometric errors. If we arbitrarily increase the color by an offset (0.01 mag and 0.5 mag) almost all the fitting parameters remain similar. Only the Hubble constant free absolute magnitude $\mathcal{M}_{\lambda 1}$ changes from to -0.83 to -1.23 but is explained by the fact that $\mathcal{M}_{\lambda 1}$ and the intrinsic colour are degenerate.

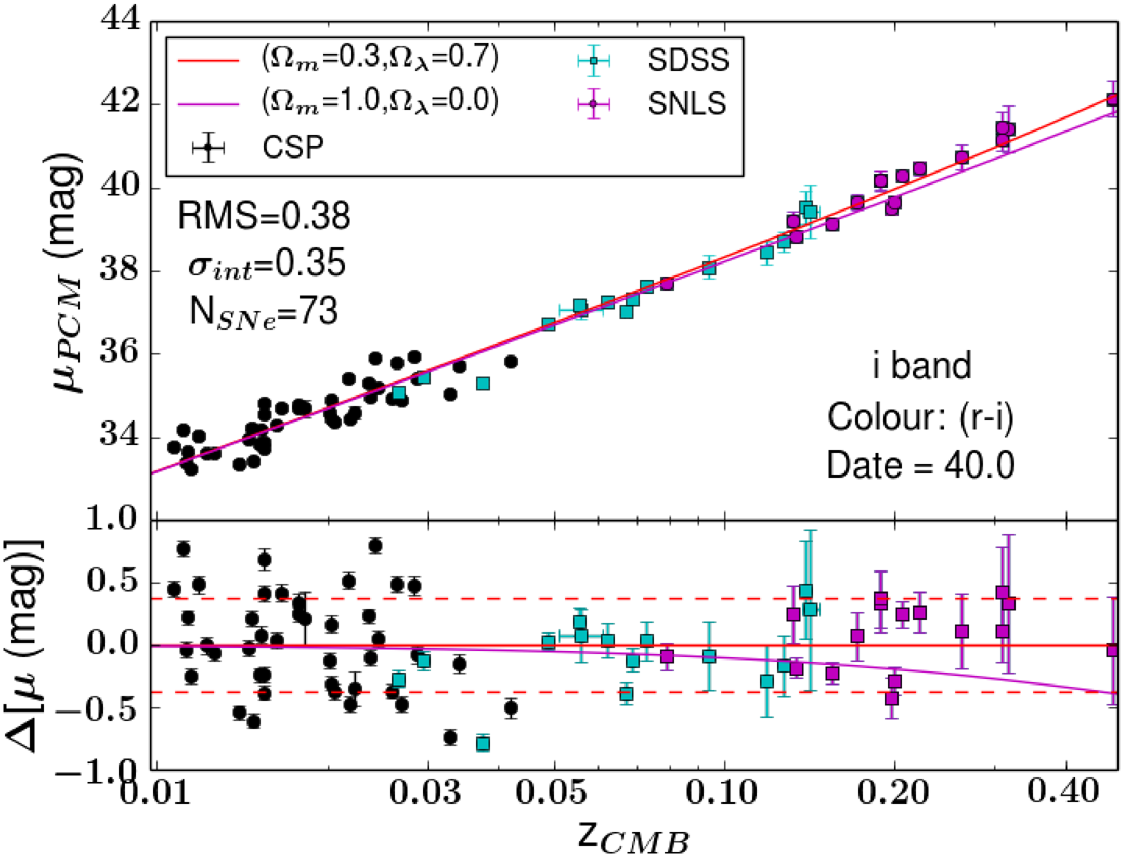

Figure 4.10: Hubble diagram for SNe II, using the PCM and all the SNe available at this epoch from the CSP, SDSS, and SNLS sample. Black dots represent the SNe from the CSP whereas the cyan and magenta squares are used for the SDSS and the SNLS sample respectively. We also plot in red line the Hubble law for the ΛCMB (Ω_m=0.3 and Ω_Λ=0.7) and in magenta line an Einstein-de Sitter cosmological model (Ω_m=1.0 and Ω_Λ=0.0). In both models, we assume a Hubble constant of 70 km s^{-1} Mpc^{-1}. In the bottom panel, the residuals from the Hubble diagram are shown. We also present the number of SNe available at this epoch (N$_{SNe}$), the epoch after the explosion (Date), the Root Mean Square (RMS) and the intrinsic dispersion (σ_{int}).

4.3.2 Ω_m derivation

We know that we are able to derive a Hubble diagram using the PCM at higher redshifts but can we put some constraints on the cosmological parameters?

In this section, I try to answer this question. First, I use the same methodology and procedure as done in the Section 4.3.1 but leave Ω_m, Ω_Λ as free parameters in equation 4.2. Due to the lack of higher redshift SNe II (only one with z $\geq$ 0.4), it was difficult to differentiate between the cosmological models, and so, to derive a meaningful constraint on cosmology when both are free parameters.

We can lower the number of free parameters by assuming a flat Universe. For a flat Universe, Ω_m+Ω_Λ=1 and so, we only have one free cosmological parameter: Ω_m can be left as free fitting parameter. To derive the Hubble diagram, I use the same combination of filters and epoch used for a fixed cosmology (Section 4.3.1), i.e., $(r-i)$, i and 40 days after the explosion. In Figure 4.11, I present a corner plot with all the one and two dimensional projections for the five free parameters α, β, $\mathcal{M}_{\lambda 1}$, σ_{int}, and Ω_m. As we can see, the four first parameters are defined by a Gaussian distribution (top figure of each column) with small error bars. I find values very consistent with that found with a fixed cosmology: $\alpha = 0.36^{+0.06}_{-0.06}$, $\beta = 0.70^{+0.29}_{-0.28}$, $\mathcal{M}_{\lambda 1} = -0.88^{+0.06}_{-0.06}$, and $\sigma_{int} = -0.36^{+0.04}_{-0.03}$.

For the matter density, the distribution does not look like a Gaussian distribution but the distribution width decreases as the matter density value increases. A value for the matter density of $\Omega_m = 0.33^{+0.29}_{-0.21}$ is derived which gives a density of dark energy of $\Omega_\lambda = 0.67^{+0.21}_{-0.30}$. These values are consistent with the ΛCDM cosmological model with uncertainties far from the precision achieved recently using SNe Ia, Ω_m=0.295 $\pm$ 0.034 (Betoule et al., 2014). However, these errors are comparable to those found by Perlmutter et al. (1997) for which the authors using $\sim$ 20 SNe Ia (7 SNe Ia with z between 0.3-0.5) derived $\Delta\Omega_m \sim 0.30$. Note that if only one likelihood minimisation is run (without MCMC simulation), I obtain Ω_m= 0.17 $\pm$ 0.28 (blue line in Figure 4.11). This result implies a new and independent evidence for the dark energy at two sigmas. Ω_m and its uncertainty are sensitive to systematic errors. To test, if we double the errors on s_2 with one likelihood simulation, the Universe's matter density varies from 0.17 to 0.28 and the precision from 0.26 to 0.38. On the other hand, the other fitting parameters (α, β, and $\mathcal{M}_{\lambda 1}$) do not show any evolution. The fitting parameters remain similar within the uncertainties (variation only of $\sim$ 0.04 on average for each parameter). Using the MCMC simulation, we derive $\Omega_m = 0.38^{+0.32}_{-0.24}$.

The drop in the matter density distribution and the relatively low intrinsic dispersion in the Hubble diagram obtained is very encouraging for future surveys. Indeed, with this method, we could add in the Hubble diagram more SNe II without spectral information and mostly at higher redshifts. In this section, I show that the strength of the PCM at higher redshifts will be an asset for the next generation telescopes.

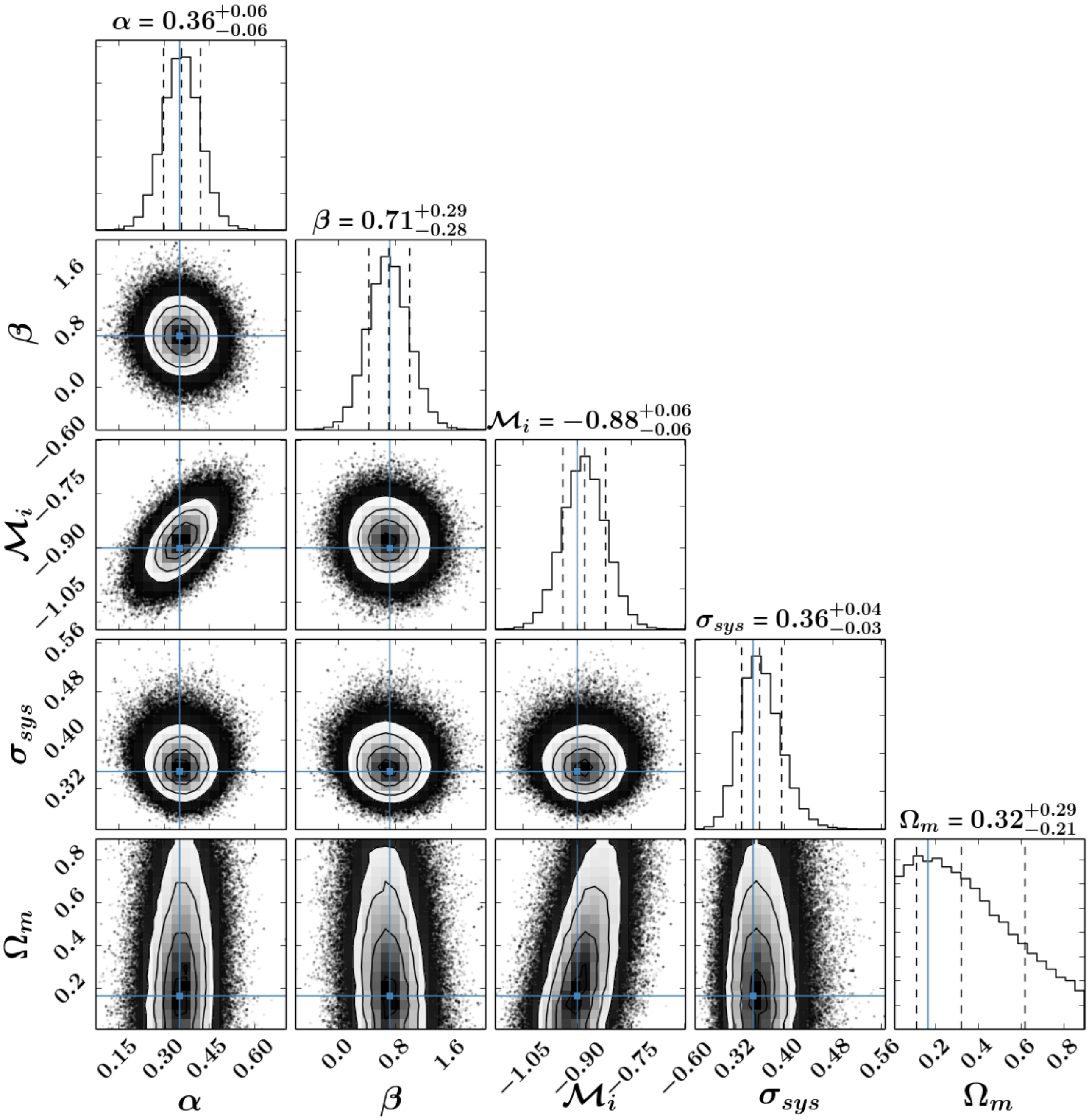

Figure 4.11: PCM: Corner plot showing all the one and two dimensional projections. The blue lines are the values obtained using only one likelihood minimisation. Contours are shown at 1, 2, and 3 sigmas. The five free parameters are plotted: α, β, $\mathcal{M}_{\lambda 1}$, σ_{int}, and Ω_m

Chapter 5

The Standard Candle Method

Contents

In this chapter, I use the SCM to standardise the SNe II. First, as done with the PCM, I use only my low redshift sample (CSP) to calibrate the method and to find a robust method to derive the photospheric expansion velocity. I also take advantage of the NIR data to see if it is possible to reduce the scatter in the Hubble diagram to 0.1–0.15 mag as suggested by Maguire et al. (2010). Finally, I extend the Hubble diagram using the entire sample.

5.1 Photospheric expansion velocities

The SCM is the most used method to standardise SNe II. This method is based on the correlation between the photospheric expansion velocities (v_{phot}) and the intrinsic luminosity and so requires at least one SN spectrum, unlike the PCM. A precise measurement of v_{phot} is not possible because no spectral line is directly connected to this velocity. However, an estimate of v_{phot} (5-10% of accuracy, Dessart & Hillier 2005) can be obtained through the minimum flux of the absorption component of the P-Cygni line profile of an optically thin line formed by pure scatter, such as Fe II λ5018 or Fe II λ5169.

Measuring the Fe II absorption line for noisy or early ($\leq$20 days) SN spectra can be very difficult, this is why some authors attempt to use stronger features. Nugent et al. (2006) proposed to use the Hβ λ4861 absorption which is stronger than the Fe II absorption line and it is also present in the early SN spectrum. Even if the Hβ line is less tightly connected to v_{phot} than the Fe II line (Dessart & Hillier, 2005), a strong relation between the two velocities was found. The original correlation between the Hβ λ4861 and Fe II velocities found by Nugent et al. (2006) was revisited recently by Poznanski et al. (2010) and Takáts & Vinkó (2012). Using 28 spectra ranging between 5 to 40 days, Poznanski et al. (2010) found $\mathrm{v}_{Fe_{II}}$= 0.84 ±0.05 $\mathrm{v}_{H\beta}$, relation confirmed by Takáts & Vinkó (2012) who found using the same range $\mathrm{v}_{Fe_{II}}$=0.823 ±0.015 $\mathrm{v}_{H\beta}$. Using the spectral library at low redshifts (CSP sample), and $\sim$ 100 spectra between 0 and 40 days after the explosion, I derive a very consistent relation. As we can see in Figure 5.1 where I present the Fe II λ5018 velocity versus Hβ λ4861 velocity, I obtain a strong correlation with a Pearson factor of 0.92 and a relation between both velocities defined as $\mathrm{v}_{Fe_{II}}$= 0.83 ± 0.04 $\mathrm{v}_{H\beta}$, consistent with previous works. Note that in this work, we use Fe II λ5018 line instead of Fe II λ5169 because the second line can be blended by other elements such as the Fe triplet or Sc I. In Figure 5.1 we also present the correlation between the two velocities, without any phase cut.

Expansion velocities are measured from the minimum flux of the absorption component of P-Cygni line profile after correcting the spectra for the heliocentric redshifts of the host-galaxies. In both cases, the errors on the velocities were obtained by measuring many times the minimum of the absorption changing the continuum. To find the best epoch to use the SCM we need the velocities at different epochs. As proposed by (Hamuy, 2001) and used in all the SNe II cosmology works Nugent et al. (2006); Poznanski et al. (2009); D'Andrea et al. (2010); Poznanski et al. (2010); Olivares et al. (2010); Rodríguez et al. (2014); de Jaeger et al. (2015b) we do an interpolation/extrapolation using a power law of the form:

$$V(t) = A \times t^{\gamma}, \tag{5.1}$$

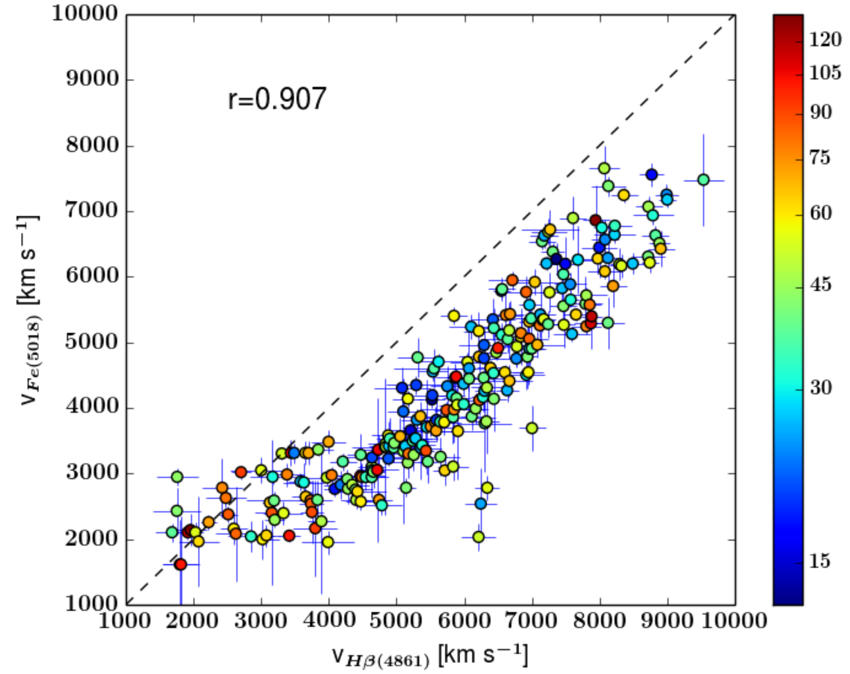

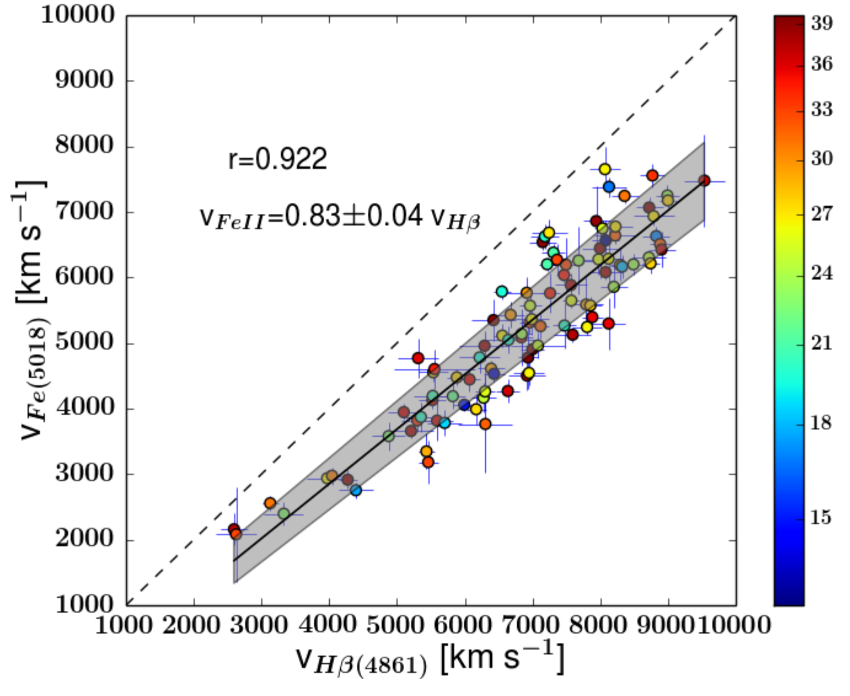

Figure 5.1: In both figures we represent the velocities determined from the absorption minima of Fe II λ5018 and Hβ λ4861. The dashed line represent x=y. *Top figure:* For this figure we used 242 spectra of SNe II at phases between 0 and 120 days after the explosion. The color bar represents the different epoch after the explosion for the spectra. The pearson factor is also represented. *Bottom figure:* In this figure we plot only the spectra of SNe II at phases of 0-40 days after the explosion, i.e., 98 spectra. The shaded area is the 1σ region for the derived correlation written is the plot.

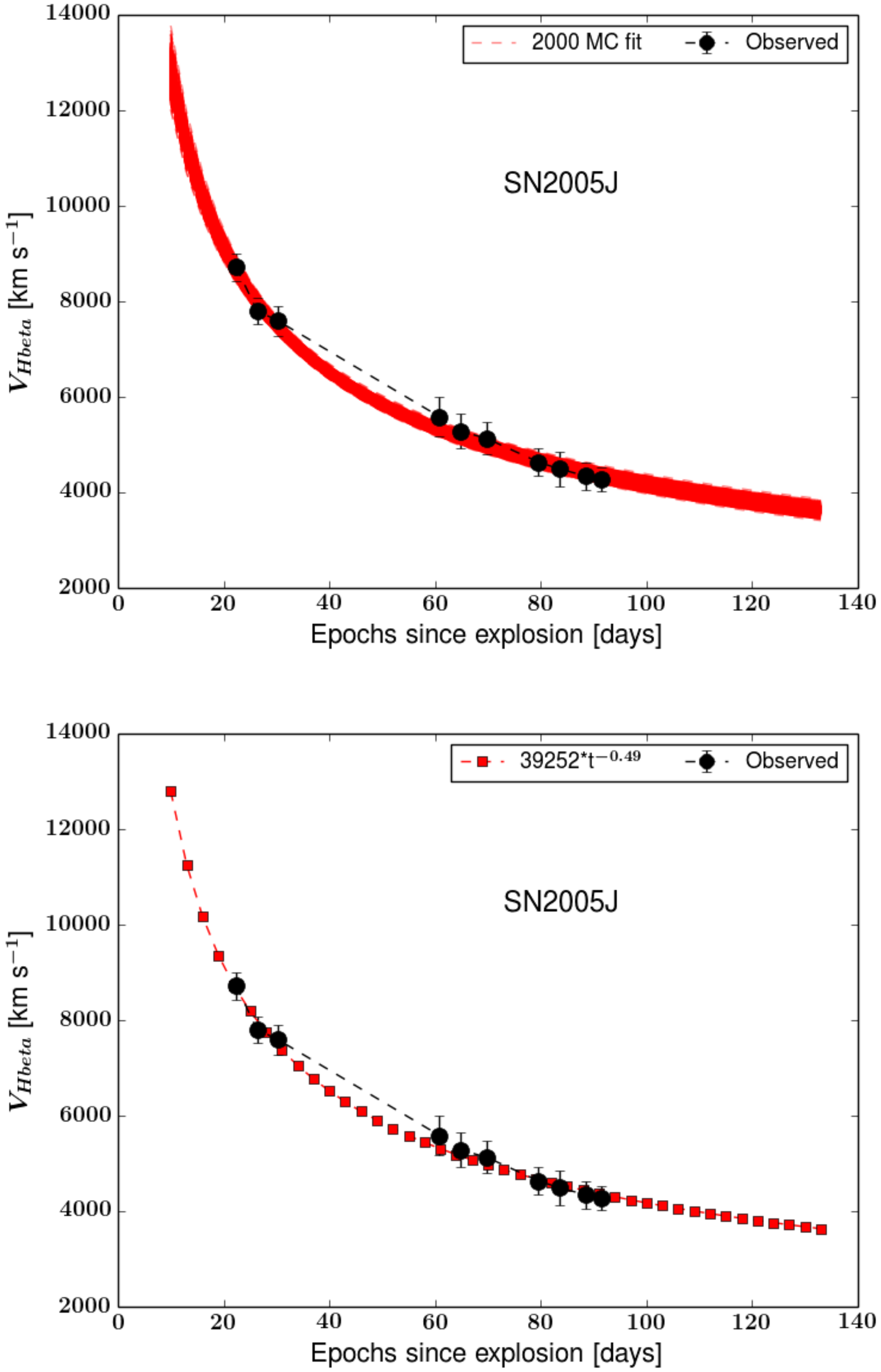

Figure 5.2: *Top panel:* The black dots represent the measured Hβ velocities (y-axis) for different epochs (x-axis). The red lines show the 2000 MC fit achieved using a power law. *Bottom panel:* The black dots represent the measured Hβ velocities (y-axis) for different epochs (x-axis) whereas the red squares represent the power law chosen (median of the 2000 fits) for this specific SN.

For the low redshift sample, I use the Fe II $\lambda5018$ absorption because due to the high quality of the data this line is visible in the spectra. Unfortunately, for some SNe only one spectrum was obtained and thus it is impossible to constrain both unknowns A and γ. I decide for these SNe to fix the γ and leave only A as a free parameter. For γ I use the median value of all SNe with at least three spectra. The median value derived is $-0.55\pm$ 0.25. This value is comparable to that found by other authors (-0.5 for Olivares et al. 2010 and -0.464 by Nugent et al. 2006 and -0.546 by Takáts & Vinkó (2012)) despite the fact that they used the Fe II $\lambda5169$ lines. Note that, as found by Faran et al. (2014a), the iron velocity for the fast-decliners (SNe IIL) also follow a power law but with more scatter. Indeed for the slow-decliners ($s_2 \leq 1.5$) we find a median value, $\gamma = -0.55 \pm 0.18$ whereas for the fast-decliners ($s_2 \geq 1.5$) we obtain $\gamma = -0.56 \pm 0.35$.

At higher redshifts the quality of the spectra does not allow us to distinguish the Fe II $\lambda5018$ line unlike the Hβ $\lambda4861$ absorption which is easily seen in all the spectra. To be consistent between the lower and higher redshifts, in Section 5.4, all the SNe II will be corrected for the expansion velocity using the same line, i.e., Hβ $\lambda4861$. As for the low redshifts, and especially for the SNLS sample, I have many SNe II for which only one spectrum was acquired. For these SNe, I use a power law with a fixed γ. Using the Hβ line and the SNe II with at least 3 spectra, I derived a median value of $\gamma = -0.407\pm$ 0.173.

It is important to note that the difference of methodology from this thesis and the SN II cosmology works found in the literature. The majority of the works used the same power law for all the SNe II whereas in my work, γ is different for all SNe. This has an impact on the velocity values derived. For example, if we assume that A is equal to 20 000 km s^{-1}, a difference of 0.1 in γ (e.g. -0.407 and -0.507) leads to a difference of $\sim$ 67% in distances. Additionally, in Section 6.2.4, I show the possibility of using a new relation between A and γ in order to derive the velocity when only one spectrum is acquired, without assuming the same power-law exponent.

5.2 Methodology

As for the PCM (Section 5.3), the same methodology is applied to derive the Hubble diagram. Again, I run a MCMC and minimise the negative log of the same likelihood function (equation 4.4) but now correcting the magnitude for the photospheric expansion velocity. Thus, the observed magnitudes are modelled as:

$$
\begin{aligned}
m_{\lambda 1}^{model} =& \mathcal{M}_{\lambda 1} - \alpha log_{10}\left(\frac{v_{H\beta}/v_{Fe}}{5000\ km\ s^{-1}}\right) + \beta_{\lambda 1}(m_{\lambda 2} - m_{\lambda 3}) \\
&+ 5log_{10}(\mathcal{D}_{lum}(z_{CMB}|\Omega_m, \Omega_\Lambda)),
\end{aligned}
\tag{5.2}
$$

where $\mathcal{D}_{lum}(z|\Omega_m, \Omega_\Lambda)$, z_{CMB}, $\mathcal{M}_{\lambda 1}$, α, and β_{λ_1} are defined in the previous section and as σ_{tot}^2 is defined as:

$$
\begin{aligned}
\sigma_{tot}^2 =& \sigma_{m_{\lambda 1}}^2 + (\frac{\alpha}{ln10}\frac{\sigma_{v_{H\beta}}}{v_{H\beta}})^2 + (\beta\sigma_{(m_{\lambda 2}-m_{\lambda 3})})^2 \\
&+ \left(\sigma_z \frac{5(1+z)}{z(1+z/2)ln(10)}\right)^2 + \sigma_{int}^2
\end{aligned}
\tag{5.3}
$$

Following Poznanski et al. (2009), I add to the velocity uncertainty of every SN II a value of 150 km s^{-1}, in quadrature, to account for unknown peculiar velocities.

5.3 Low redshift Hubble diagram

As done in 4.2, I first apply the SCM to my low redshift sample in order to refine the method used by the others works. To compare with the PCM, I use the same colour, $(V - i)$, and the same filters (r, Y bands). For the SCM, the photospheric expansion velocity is very dependent on the explosion date. Due to this, and after trying different epochs and references, I find that the best reference is the explosion time as used by Nugent et al. (2006), Poznanski et al. (2009), Rodríguez et al. (2014). The same epoch for the magnitude, the colour and the iron velocity is employed. Again, I select only the SNe in the Hubble flow and thus, the sample at low redshift available is composed of 24 SNe II (some SNe do not have colour at this epoch).

In Figure 5.3, I present the Hubble diagram sequence at epoch of 31 days after the explosion in the r band. The top left panel shows the Hubble diagram without any additional correction (only AKS) for which I derive an intrinsic dispersion of 0.56 mag. Then, thanks to the photospheric expansion velocity correction, the scatter drops to 0.34 mag as it is shown in the top right. Finally, using the SCM, i.e., adding the colour term for the Avh, the dispersion drops to 0.26 mag. This dispersion allows us to derive distances with an accuracy of $\sim$ 12%. If I do not select only the SNe II in the Hubble flow (37 SNe available), the scatter drops from 0.61 mag to 0.31 mag.

In Figure 5.4, I present the NIR Hubble diagram using the Y band. For the NIR filters, the epoch chosen is 44 days after the explosion. This figure shows the same sequence as above, i.e., the top left panel shows the Hubble diagram without any

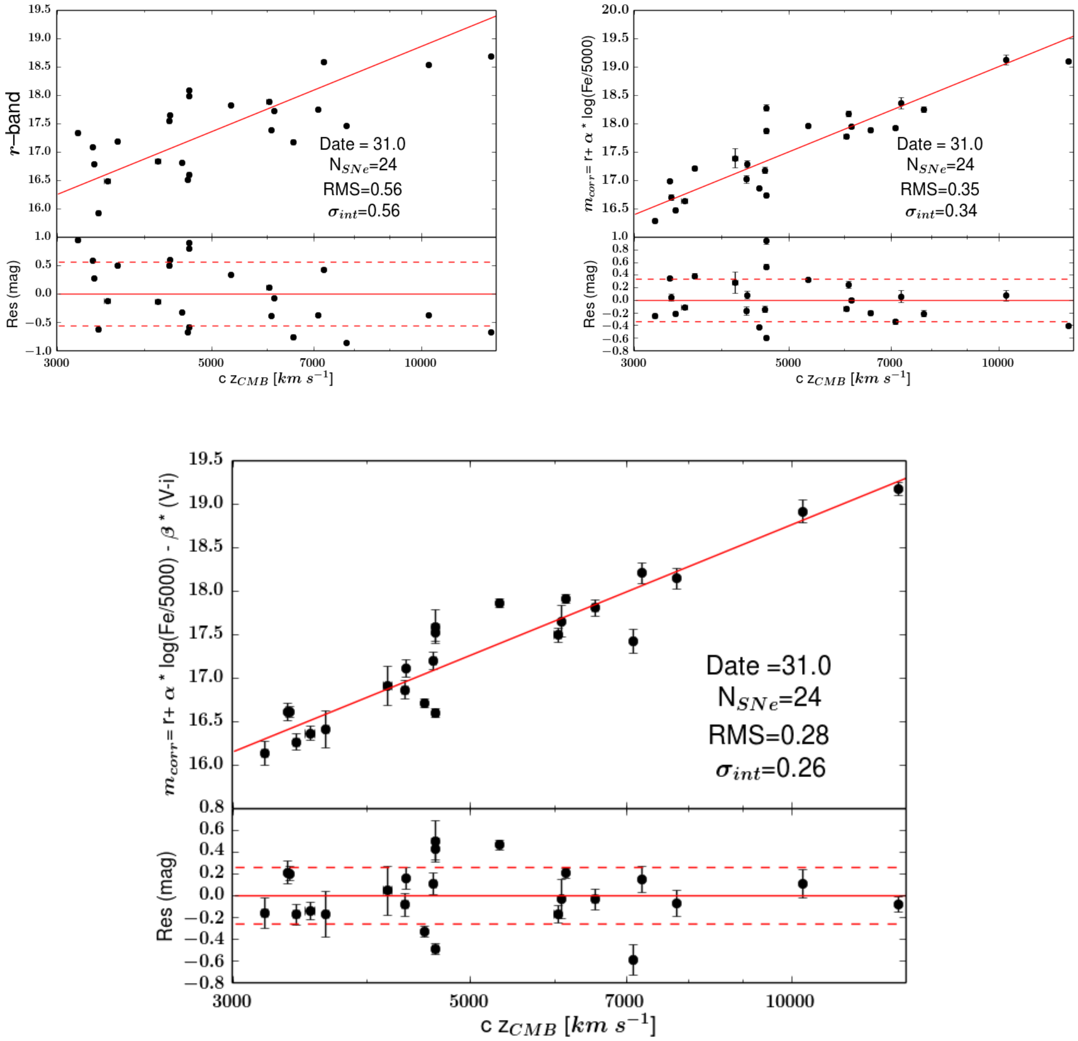

Figure 5.3: In the figures, we present the dispersion (RMS) using the SCM, the number of SNe (N_{SNe}), the epoch chosen with respect to the explosion and the intrinsic dispersion (σ_{int}) for our Hubble flow sample. On the bottom of each plot, the residuals are shown. In all the residual plots, the dashed line corresponds to the σ_{int}. *Top Left panel:* Apparent magnitude corrected for AKS in the r band plotted against cz_{CMB}; *Top Right panel:* Apparent magnitude corrected for AKS and the photospheric expansion velocity term in the r band plotted against cz_{CMB}. *Bottom panel:* Apparent magnitude corrected for the SCM using the colour term $(V-i)$.

additional correction. For this Hubble diagram I derive an intrinsic dispersion of 0.44 mag. The raw dispersion is smaller than the one found in the optical band due to the host galaxy extinction which is bigger at smaller wavelength. In the top right panel, I present the Hubble diagram with the v$_{phot}$ correction where the scatter drops to 0.27 mag. Finally, the Hubble diagram after the SCM is shown in the bottom panel and I derive a dispersion of 0.26 mag, which is a quite smaller than the one derived without colour correction, again essentially due to the host galaxy extinction. Using all the SNe II at any redshift (35 SNe), the scatter drops from 0.52 mag without correction to 0.30 mag after applying the SCM.

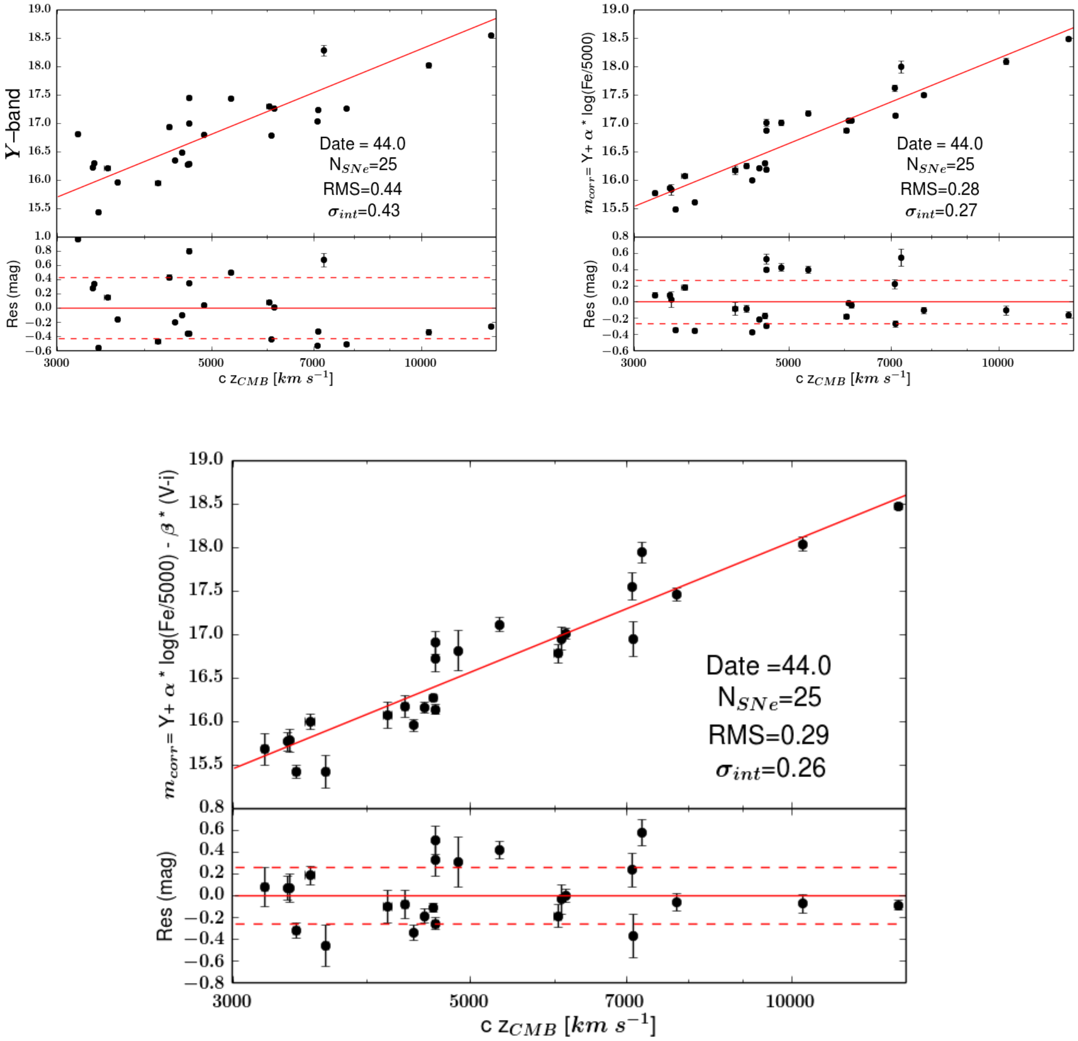

Figure 5.4: In the figures, we present the dispersion (RMS) using the SCM, the number of SNe (N_{SNe}), the epoch chosen with respect to the explosion and the intrinsic dispersion (σ_{int}) for our Hubble flow sample. On the bottom of each plot, the residuals are shown. In all the residual plots, the dashed line corresponds to the σ_{int}. *Top Left panel:* Apparent magnitude corrected for AKS in the Y band plotted against cz_{CMB}; *Top Right panel:* Apparent magnitude corrected for AKS and the photospheric expansion velocity term in the r band plotted against cz_{CMB}. *Bottom panel:* Apparent magnitude corrected for the SCM using the colour term $(V-i)$.

The values found using optical or NIR filters, are somewhat better than previous studies (Hamuy & Pinto, 2002; Nugent et al., 2006; Poznanski et al., 2009; Olivares et al., 2010; D'Andrea et al., 2010) where the authors found dispersions around 0.30

mag with 30 SNe (more details in Section 6.1.2). Note the major differences between my study and theirs is that they included SNe outside the Hubble flow, only slow-declining SNe II (SNe II with low s_2, historically referred to as SNe IIP), did not calculate a power-law for each SN as I do, and I use a different epoch. Note also the work done by Maguire et al. (2010) where they applied the SCM to NIR filters (J-band and $(V-J)$ colour) using nearby SNe (92% of their sample with $cz \leq 3000$ km s^{-1}), finding a dispersion of 0.39 mag with 12 SNe (see Section 6.1.2). To finish we tried a combination of the PCM and SCM, i.e., adding a s_2 term to the SCM but this does not improve the dispersion.

5.4 All sample Hubble diagram

5.4.1 Fixed cosmology

In this section I propose to derive the most complete SNe II Hubble diagram using the three surveys. For this, I use the same filters combination used with the PCM, i.e., $i/(r-i)$ and I plot the Hubble diagram at an epoch of 45 days in the rest frame post-explosion. This epoch is chosen by minimising the intrinsic scatter. Note that the epoch corresponds to the plateau phase and it is very consistent to that used in other works (50 days in rest frame post-explosion). The total sample available for these combinations and epoch is composed of 61 SNe II, 40 SNe II from CSP, 16 SNe II from SDSS, and 5 SNe II from SNLS.

The intrinsic dispersion derived in the Hubble diagram is 0.27 mag, i.e, 12% in distance errors. The use of the SCM allows us to reduce the intrinsic scatter from 0.55 mag (raw magnitudes) to 0.27 mag, i.e., an improvment of 13% in distance errors. I derive $\alpha = 3.18^{+0.40}_{-0.40}$, $\beta = 0.97^{+0.26}_{-0.25}$, and $\mathcal{M}_{\lambda 1} = -0.87^{+0.05}_{-0.05}$. Assuming a Hubble constant of H_0=70 km s^{-1} Mpc^{-1}, an absolute magnitude $M_i = -16.63^{+0.05}_{-0.05}$ is obtained from $\mathcal{M}_{\lambda 1}$. The Hubble diagram and its associated Hubble residual are plotted in Figure 5.5. As we can see using this method we are only able to reach redshift around 0.2 where the difference between cosmological models is very small.

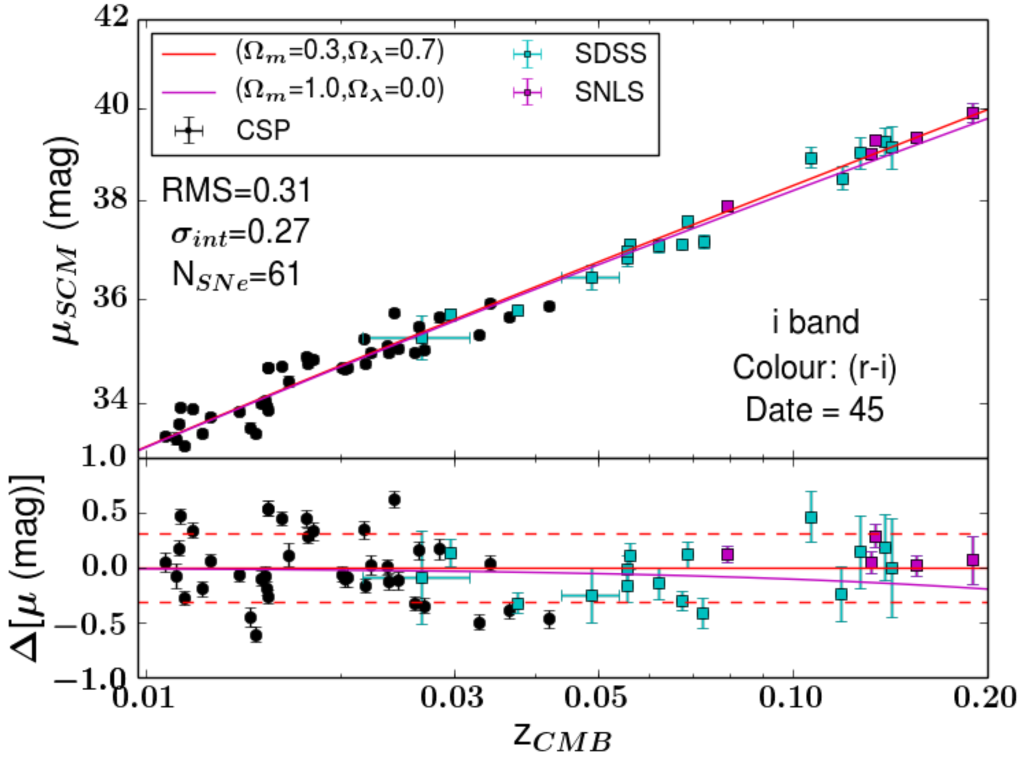

Figure 5.5: Hubble diagram for SNe II, using the SCM and all the SNe available at this epoch from the CSP, SDSS, and SNLS sample. Black dots represent the SNe from the CSP whereas the cyan and magenta squares are used the SDSS and the SNLS sample respectively. We also plot in red line the Hubble law for the ΛCMB (Ω_m=0.3 and Ω_Λ=0.7) and in magenta line a Einstein-de Sitter cosmological model (Ω_m=1.0 and Ω_Λ=0.0). In both models, we assume a Hubble constant of 70 km s^{-1} Mpc^{-1}. In the bottom panel, the residuals from the Hubble diagram are shown. We also represent the number of SNe available at this epoch (N$_{SNe}$), the epoch after the explosion (Date), the Root Mean Square (RMS) and the intrinsic dispersion (σ_{int}).

5.4.2 Ω_m derivation

As done in Section 4.3.2, in this section, I try to derive cosmological parameters. For the SCM the highest redshift used is too small to set constraints on the dark energy density and matter density. Despite this, the same MCMC calculation done in the Section 4.3.2 for a flat Universe is performed. Figure 5.6 presents the same as Figure 4.11 but this time using the SCM. I find values consistent with that found with a fixed cosmology: $\alpha = 3.19^{+0.39}_{-0.40}$, $\beta = 0.96^{+0.26}_{-0.25}$, and $\mathcal{M}_{\lambda 1} = -0.86^{+0.05}_{-0.05}$, and $\sigma_{int} = 0.29^{+0.03}_{-0.03}$.

For the matter density we see a less pronounced drop than that obtained using the PCM. The value derived for the matter density is $\Omega_m = 0.39^{+0.31}_{-0.26}$, which corresponds to $\Omega_\lambda = 0.61^{+0.26}_{-0.31}$. In Figure 5.6 the blue lines represent the value derived using a simple likelihood minimisation (without MCMC), e.g. for the density matter we obtain Ω_m= 0.16 ± 0.57 (error bigger than using PCM). We clearly see in this figure the need of higher redshift SNe II ($z \geq 0.4$) to derive cosmological parameters and to place better constraints on the matter and dark matter densities.

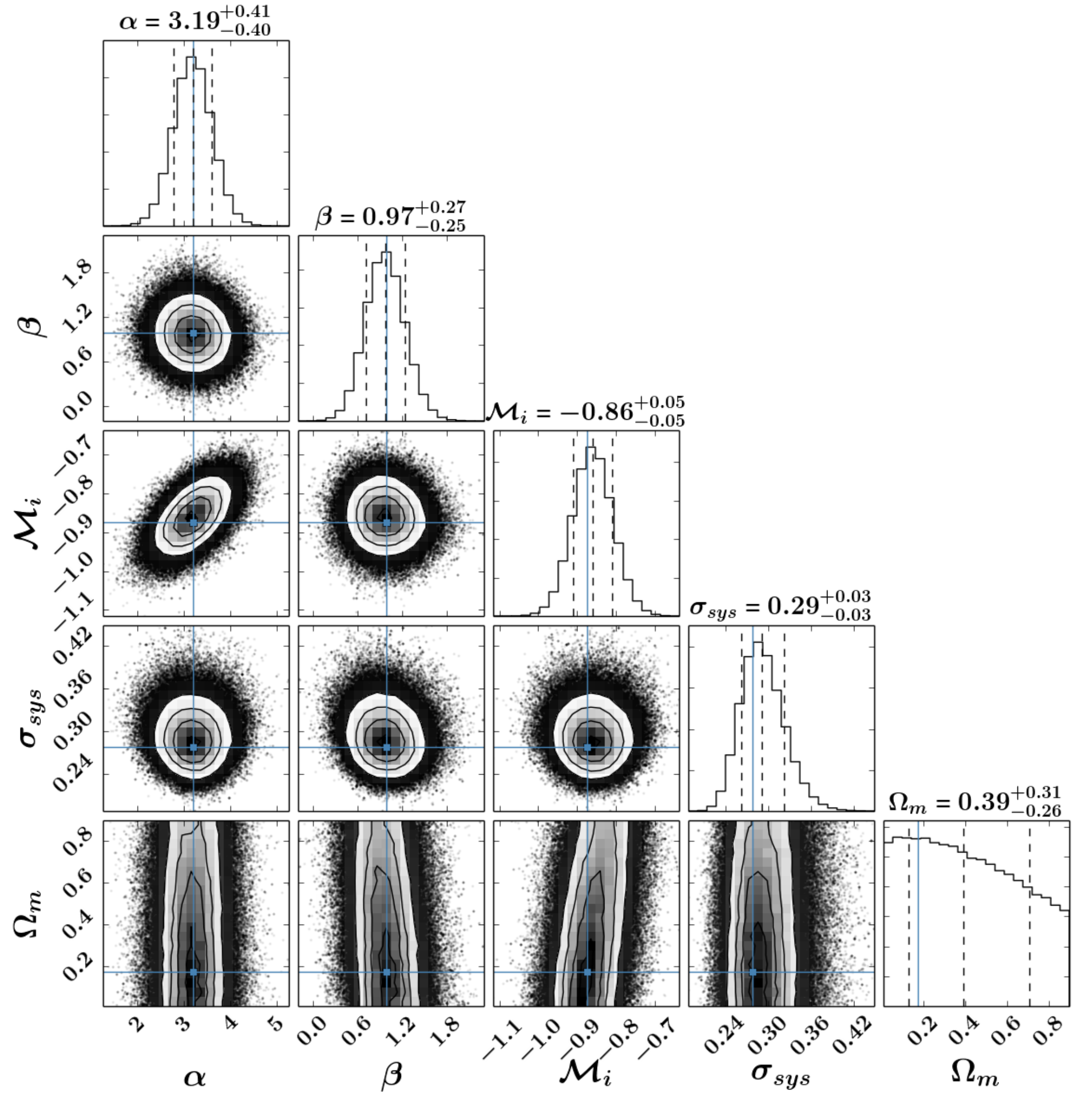

Figure 5.6: SCM: Corner plot showing all the one and two dimensional projections. The blue lines are the values obtained using only one likelihood minimisation. Contours are shown at 1, 2, and 3 sigmas. The five free parameters are plotted: α, β, $\mathcal{M}_{\lambda 1}$, σ_{int}, and Ω_m

Chapter 6

Discussion

Contents

6.1 Low redshift

6.1.1 Methods comparison

In this section, I compare the PCM and SCM. To achieve this, I use the same SNe II (Hubble flow), and the same set of magnitude-colour for the two methods. In Figure 6.1, I show the Hubble diagram obtained with the r band using the SCM and the PCM, on the left and right panel respectively. For the PCM, I obtain an intrisic dispersion of 0.41 mag whereas for the SCM I have less scatter, 0.24 mag. In Figure 6.2

I present the same figure but this time using the Y band. The same trend is found with similar dispersion.

In general the SCM is more precise than the PCM but the dispersion found with the PCM is consistent with the results found by the theoretical studies done by Kasen & Woosley (2009) (distances accurate to $\sim 20\%$) although those authors used other photometric correlations (plateau duration). As suggested by Anderson et al. (2014b) using this parameter the prediction is not seen in the observations. I try to use the OPTd values as an input instead of the s_2 but I do not see any improvement on the dispersion. Note also the recent work of Faran et al. (2014b), in which the authors found a correlation between the Fe II $\lambda5018$ velocity and the I-band total decline rate. Using our low redshift sample, I look first for a correlation between the total decline rate in V–band and s_2 parameter. A strong correlation is found with a Pearson factor of 0.9. Then I check the relation between the s_2 and the Fe II $\lambda5018$ velocity and I derive also a correlation with Pearson factor about 0.65.

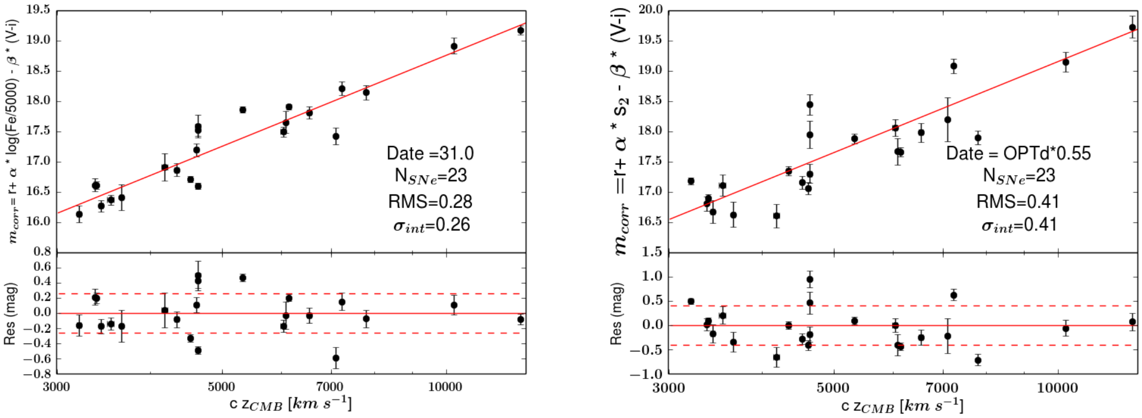

Figure 6.1: Plotted on the left is the SCM whereas in the right is for the PCM. In all the figures, we present the RMS, the intrinsic scatter (σ_{int}),the number of SNe (N_{SNe}), the epoch chosen with respect to the end of the plateau (OPTd*X%) for the PCM and with respect to the explosion date for the SCM. On the bottom of each plot, the residuals are shown. In all the residual plots, the dashed line corresponds to the RMS. For both methods we use the Hubble flow sample, $cz_{CMB} \geq 3000$ km s^{-1}, the r band and the colour $(V - i)$.

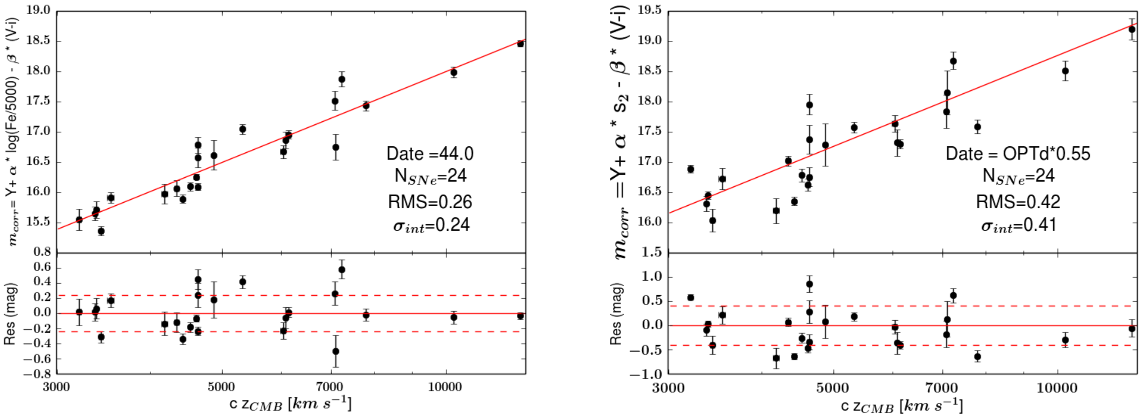

Figure 6.2: Plotted on the left is the SCM whereas in the right is for the PCM. In all the figures, we present the RMS, the intrinsic scatter (σ_{int}),the number of SNe (N_{SNe}), the epoch chosen with respect to the end of the plateau (OPTd*X%) for the PCM and with respect to the explosion date for the SCM. On the bottom of each plot, the residuals are shown. In all the residual plots, the dashed line corresponds to the RMS. For both methods we use the Hubble flow sample, $cz_{CMB} \geq 3000$ km s^{-1}, the Y band and the colour $(V - i)$.

6.1.2 SCM comparison

In this section, I compare the SCM at low redshift with other studies. First, I use only optical filters to compare with Poznanski et al. (2009) and Olivares et al. (2010). Both studies used the $(V - I)$ colour and also the I band. Note that Olivares et al. (2010) also used the B and V band but here we consider only the I band for consistency. Poznanski et al. (2009) found a dispersion of 0.38 mag using 40 slow-decliners. In our sample instead of using the I band I use the sloan filter, i band and $(V - i)$ colour. Using our entire sample, i.e., SNe in and outside the Hubble flow (36 SNe in total) I derive a dispersion similar to Poznanski et al. (2009) of 0.32 mag (epoch: 35 days after explosion). We can also compare the parameter α derived from the fit. Again I obtain a consistent value, $\alpha = 4.48 \pm 0.51$ whereas Poznanski et al. (2009) found $\alpha = 4.6 \pm 0.70$. The other parameters are not directly comparable due to the fact that the authors assumed an intrinsic colour which is not the case in the current work. Using a Hubble constant of 70 km s^{-1} Mpc^{-1} we can translate the ZP to an absolute magnitude ($ZP = M_{corr} - 5log(H_0) + 25$) M$_i$ $= -17.08 \pm 0.10$ mag that it is lower than the results obtained by Poznanski et al. (2009) (M$_I$ $= -17.43 \pm 0.10$ mag). This difference is probably due to the fact that the corrected magnitude has not been corrected for the intrinsic colour.

Using 30 slow-declining SNe II in and outside the Hubble flow Olivares et al. (2010) derived a dispersion of 0.32 mag which is the same that I obtained. However the parameters derived by Olivares et al. (2010) are different. Indeed using the same equation (5), and the entire sample they obtained $\alpha = 2.62 \pm 0.21$, $\beta = 0.60 \pm 0.09$ and

$ZP = -2.23 \pm 0.07$ instead of $\alpha = 4.48 \pm 0.51$, $\beta = 0.89 \pm 0.25$ and $ZP = -1.30 \pm 0.10$ in this work. From their ZP (H_0=70 km s^{-1} Mpc^{-1}) I derive M$_I$ = -18.00 ± 0.07 mag (M$_i$ = -17.08 ± 0.10 mag for us). When the authors restrict the sample to objects in the Hubble flow, they end up with 20 SNe II and a dispersion of 0.30 mag. If I do the same cut, I find a RMS of 0.28 mag for 24 SNe II. I obtain consistent dispersion for both samples using similar filters. Note that reducing our sample to slow-decliners alone ($s_2 \leq 1.5$, the classical SNe IIP in other studies) in the Hubble flow does not improve the dispersion. The difference in dispersion between Olivares et al. (2010) and my study can be due, among other things, to the difference in epoch used, or that I calculate a power-law for each SN for the velocity.

With respect to the NIR filters Maguire et al. (2010) suggested that it may be possible to reduce the scatter in the Hubble diagram to 0.1–0.15 mag and should be confirmed with a larger sample and more SNe II in the Hubble flow. The authors used 12 slow-decliners but only one SN II in the Hubble flow. Using the J band and the colour $(V - J)$ they found a dispersion of 0.39 mag against 0.50 mag using the I band. From this drop in the NIR, the authors suggested that using this filter and more SNe II in the Hubble flow could reduce the scatter from 0.25-0.3 mag (optical studies) to 0.1–0.15 mag. With the same filters used by Maguire et al. (2010), and using the Hubble flow sample, I find a dispersion of 0.27 mag with 23 SNe II. This dispersion is 0.1 mag higher than that predicted by Maguire et al. (2010) (0.1–0.15 mag). To derive the fit parameters, the authors assumed an intrinsic colour and chose $(V - J)_0 = 1$ mag. They obtained $\alpha = 6.33 \pm 1.20$ and an absolute magnitude M$_J$=−18.06 ± 0.25 mag (H_0=70 km s^{-1} Mpc^{-1}). If I use only the SNe II with $cz_{CMB} \geq 3000$ km s^{-1} (23 SNe), I find $\alpha = 4.68 \pm 0.65$ and ZP = −1.76 ± 0.10 which corresponds to M$_J$=−17.54 ± 0.10 mag assuming H$_0$ = 70 km s^{-1} Mpc^{-1}. If I include all SNe II at any redshift, the sample goes up to 34 SNe II and the dispersion to 0.30 mag. From all SNe II I derive $\alpha = 4.36 \pm 0.51$ and ZP =−2.04 ± 0.20 which corresponds to M$_J$=-17.81 ± 0.2. To conclude, the Hubble diagram derived from the CSP sample using the SCM is consistent and somewhat better with those found in the literature.

More recently, Rodríguez et al. (2014) proposed another method to derive a Hubble diagram from SNe II. The PMM corresponds to the generalisation of the SCM, i.e., the distances are obtained using the SCM at different epochs and then averaged. Using the $(V - I)$ colour, and the filter V, the authors found an intrinsic scatter of 0.19 mag. Using the V band and the $(V - i)$ colour and doing an average over several epochs we found a dispersion of 0.26 mag which is similar to the value found from the SCM but higher than the value derived by Rodríguez et al. (2014).

6.1.3 Low number effects

In supernova cosmology, the figure of merit is the RMS or the σ_{int} and the holy grail for everyone is to obtain very low dispersion in the Hubble diagram (i.e. low distance errors). In this work I show that in the Y band I can derive a RMS around 0.40–0.45 mag using the Hubble flow sample (30 SNe II) and the entire sample (40 SNe II), whereas using the golden sample (8 SNe II) I obtain a dispersion of 0.18 mag. It is important to know if this decrease in RMS is due to the fact that I used well-studied SNe II within the golden sample or if it is due to the low number of SNe II. For this purpose I do a test using the Monte Carlo bootstrapping method.

From the Hubble flow sample, I remove randomly one SN II and compute the dispersion. I do that for 30000 simulations and the final RMS corresponds to the median, and the errors to the standard deviation. Then after removing one SN II, I remove randomly two SNe II and again estimate the RMS and the dispersion over 30000 simulations. I repeat this process until I have only 4 SNe II, i.e., I remove from one SN II to (size available sample - 4 SNe II). For each simulation I compute a new model, i.e., new fit parameters (α, β, and ZP).

Figure 6.3 (Top panel) presents the evolution of the RMS versus the number of SNe II for both methods (PCM and SCM) using the Y band. For both methods, after a constant median value the RMS decreases when the number of SNe II is lower than 10 SNe II because the model starts diverging. Indeed if we look at Figure 6.3 on the bottom panel where the evolution of the fit parameters versus the number of SNe for one single epoch (OPTD*0.65) and the Y band are presented, we see that for the PCM, α, β and ZP change significantly when the number of SNe II is around 10. The values start diverging for a number of SNe II smaller around 10, so this implies that the RMS is driven by the reduced number objects and therefore it will be difficult to conclude between the fact that β and ZP are better because we have a better RMS or because it is due to a statistical effect. Note that the figure does not present directly the value of the fit parameters but a fraction of the value, i.e., the value divided by the first value plus an offset corresponding to the first value.

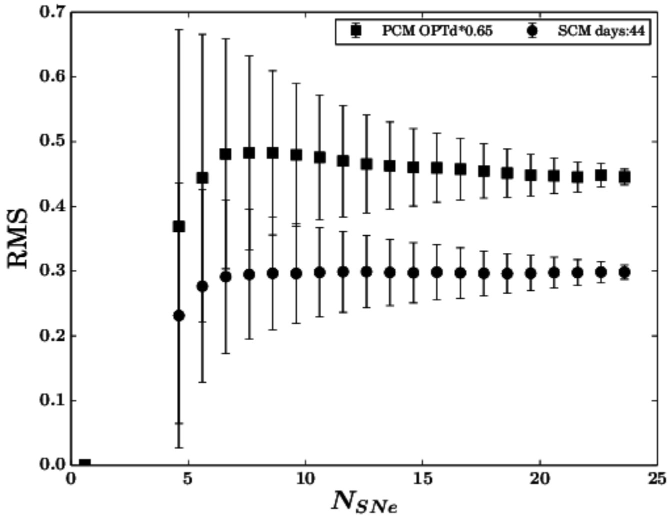

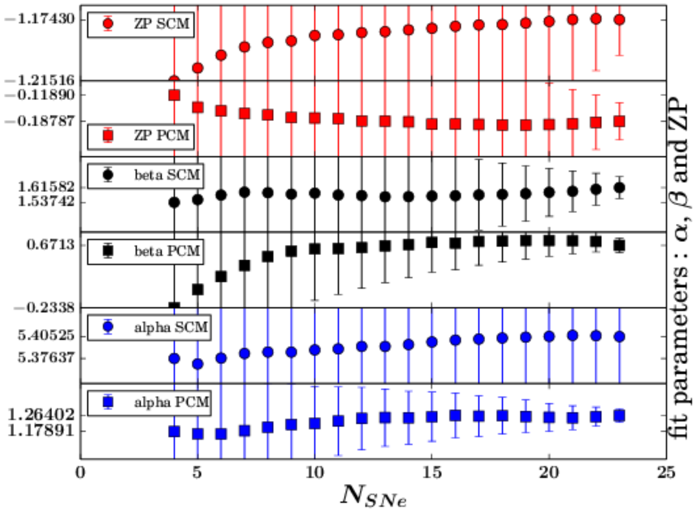

Figure 6.3: *Top figure:* We present the evolution of the σ_{int} versus the number of SNe for one single epoch, OPTD*0.65 for the PCM and 44 days post explosion for the SCM. We use the Y band and the $(V-i)$ colour. The black squares represent the evolution for the PCM whereas the black circles are used for the SCM. *Bottom figure:* We present the evolution of our fit parameters (α, β, and ZP) versus the number of SNe. The black colour represents the β, the red is for ZP, and the blue for α. The circles are used for the SCM and the squares for the PCM.

6.1.4 Low R_V

As stated in Chapter 4, the β_{λ_1} colour term is related to the total-to-selective extinction ratio if the colour-magnitude relation is due to extrinsic factors (dust). In the literature, for the MW, R_V is known to vary from one line of sight to another, from values as low as 2.1 (Welty & Fowler, 1992) to values as large as 5.6-5.8 (Cardelli et al., 1989; Fitzpatrick, 1999; Draine, 2003). In general for the MW, a value of 3.1 is used which corresponds to an average of the Galactic extinction curve for diffuse interstellar medium (ISM). Using the minimisation of the Hubble diagram with a colour term, in the past decade the SNe Ia community was surprised by deriving lower R_V for host-galaxy dust than that for the MW. Indeed they found R_V between 1.5–2.5 (Krisciunas et al., 2007; Elias-Rosa et al., 2008; Goobar, 2008; Folatelli et al., 2010; Phillips et al., 2013). This trend was also seen more recently using SNe II (Poznanski et al., 2009; Olivares et al., 2010; Rodríguez et al., 2014). This could be due to unmodeled effects (e.g. Scolnic et al. 2014).

I follow previous work in using the minimisation of the Hubble diagram to obtain constraints on R_V for host-galaxy dust. Using the PCM, the Hubble flow sample and the r band, I find β_r close to 0.85. Using a Cardelli et al. (1989) law I can transform this value into total-to-selective extinction ratio, and I obtain, $R_V = 1.01^{+0.53}_{-0.41}$. Following the same procedure but using the SCM, I also derive low R_V values, consistent with those derived using the PCM.

At first sight, this analysis would suggest a significantly different nature of dust in our Galaxy and other spiral galaxies, as previously seen in the analysis of SNe Ia and SNe II. However, I caution the reader that the low R_V values could reflect instead intrinsic magnitude-colour for SNe II not properly modelled. Disentangling both effects would require to know the intrinsic colours of our SNe II sample. In a forthcoming paper I will address this issue through different dereddening techniques that I am currently investigating. I also do this for other combinations of filters and colours. Figure 6.4 presents the R_V values for all the apparent magnitudes (B, g, V, r, i, Y, J) and different colour term corrections. As seen previously from the $r/(V-i)$ and $Y/(V-i)$ magnitude/colour combinations, again I obtain very low R_V values around 0.8 and always ≤ 1.5, with typical uncertainties (estimated by propagation of the error in the β through the Cardelli et al. 1989 law) of 0.2.

6.2 High redshift

6.2.1 Sample comparison

In this part, we will compare the three samples used for this work: CSP, SDSS-II, and SNLS. In Figure 6.5 (top), we compare the absolute magnitude uncorrected for velocity or host extinction and assuming a standard cosmology ($\Omega_m = 0.3$, and $\Omega_\Lambda = 0.7$). Even if the number of SNe II used is very different (40 for CSP, 16 for SDSS-II,

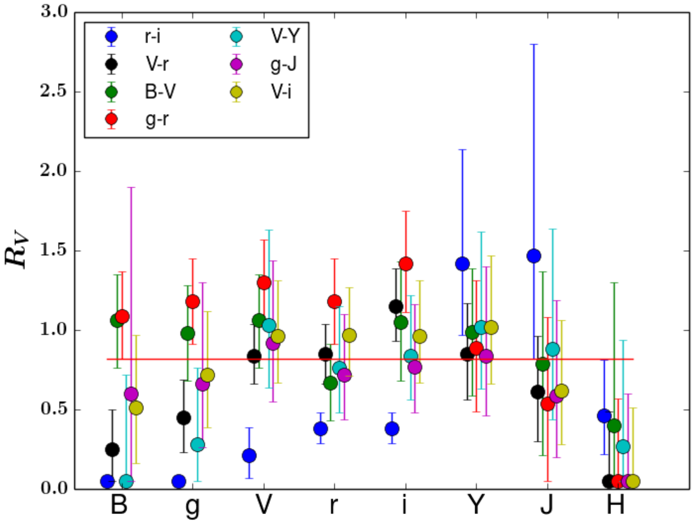

Figure 6.4: Different values of R_V obtained using different filters and colours. In the x-axis is the filter used, from B band to J band. For each filter we present different colours used to obtain β_{λ_1}. The blue circles present $(r-i)$, black for $(V-i)$, green for $(B-V)$, red for $(g-r)$, cyan for $(V-Y)$, magenta for $(g-J)$ and yellow for $(V-i)$.

and 5 for SNLS), the luminosity distribution appears different. The CSP sample has absolute magnitudes over a range of 2 magnitudes which is expected for SNe II. For the SDSS-II sample, as found by D'Andrea et al. (2010), it spreads only a small range of absolute magnitude (0.7 mag). The authors explained the lack of any dim SNe II above z =0.10 by the Malmquist bias. At low redshift, we do not have intrinsically dimmer SNe II in the SDSS-II sample due to the fact that dimmer candidates were not followed spectroscopically and no SNe II without spectroscopy from D'Andrea et al. (2010) sample could be added due to the photometry quality and/or sampling. For the SNLS sample, the sample size is too small to derive conclusions. The same result is found by analysing the distribution of Hβ velocities. The CSP sample spreads over a large range of velocities (2500-8500 km s^{-1}) while the SDSS-II sample has in general high velocities (5000-8000 km s^{-1}). The lack of low velocities for the SDSS-II sample could be explained by the bias toward more luminous SNe II in the SDSS-II sample. In the future, with larger datasets, we will be able to characterise systematic biases better.

6.2.2 PCM versus SCM

Using a larger data sample and higher redshift SNe II than de Jaeger et al. 2015b ($\sim$ 40 SNe II up to z~0.04), we obtain an intrinsic dispersion of 0.35 mag with the PCM and 0.27 mag with the SCM. The difference between both methods is only of 0.08 mag, i.e., 3% in distances but with the PCM, we are able to use more SNe II (73

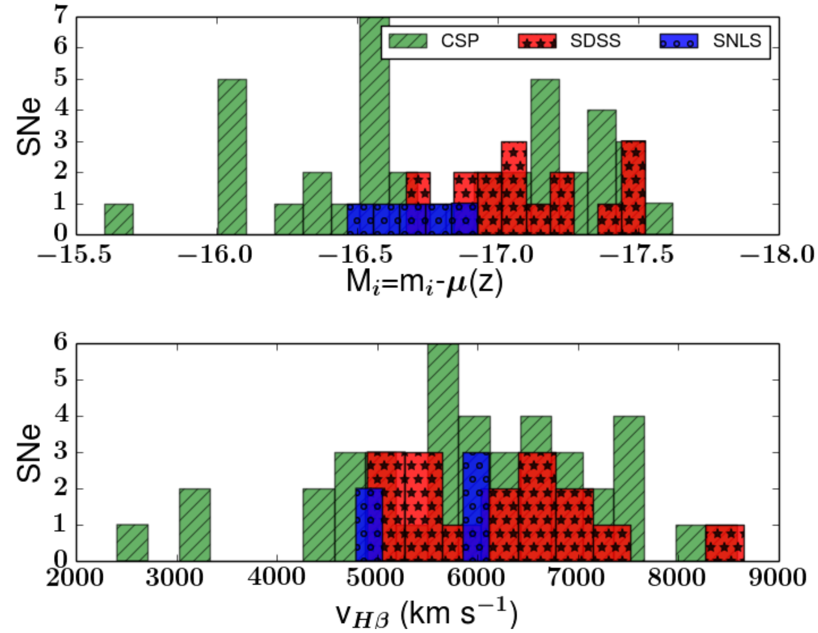

Figure 6.5: Comparison of the CSP, SDSS and SNLS samples. Top panel represents the absolute magnitude without any calibration (not corrected for velocity or dust) and assuming a Hubble constant of 70 km s^{-1} Mpc^{-1}, $\Omega_m = 0.3$, and $\Omega_\Lambda = 0.7$. The bottom panel shows the distribution of Hβ velocity. In both plots, green colour represents the CSP sample, red colour the SDSS sample, and blue colour the SNLS sample.

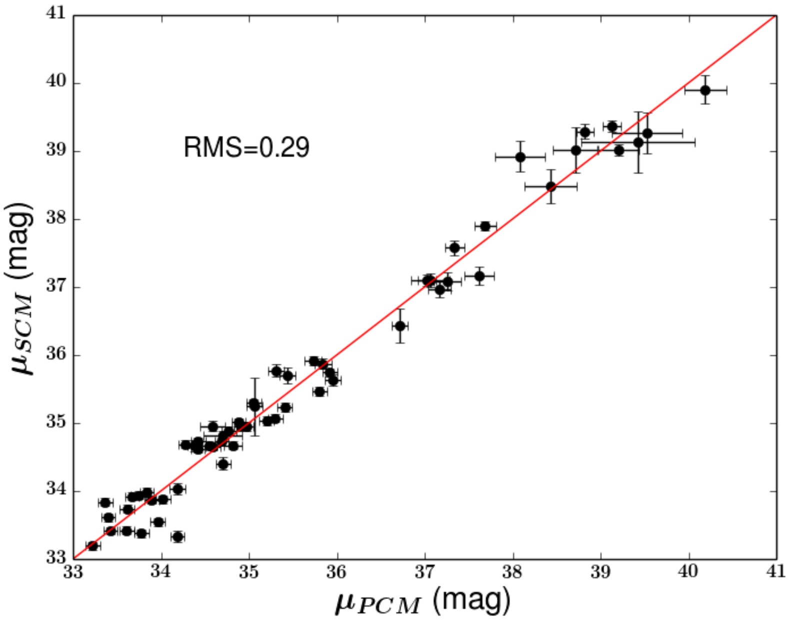

Figure 6.6: Comparison distance moduli obtained using the PCM (x-axis) and the SCM (y-axis). The red line shows $x = y$.

versus 61) and it can be extended to higher redshift (~ 0.5 versus ~ 0.2). The next generation of telescopes will observe many thousands of SNe II and the PCM will be very useful to derive cosmological parameters. In Figure 6.6 we present the distance modulus obtained using the PCM and the SCM. For these two methods, we have 59 SNe II in common. As we can see the values derived are very consistent using both methods with a RMS of 0.29 mag. All the distance modulus calculated from both methods are listed in Table 2.1.

6.2.3 SCM versus others works

The scatter found in this work is very consistent with those found by previous studies (Nugent et al., 2006; Poznanski et al., 2009; D'Andrea et al., 2010; Poznanski et al., 2010; Olivares et al., 2010; Rodríguez et al., 2014; de Jaeger et al., 2015b). For example with a similar methodology (same likelihood), D'Andrea et al. (2010) using 15 SNe II from SDSS-II with 34 SNe II low redshift SNe II from Poznanski et al. (2009) found an intrinsic dispersion of 0.29 mag. They also derived very consistent free parameters $\alpha = 4.0 \pm 0.7$, $\beta = 0.8 \pm 0.3$, but a different absolute magnitude $M_I = -17.52 \pm 0.08$, mainly due to the fact that they assumed an intrinsic colour of 0.53 mag to correct their magnitudes for extinction, which we did not.

Poznanski et al. (2009) found also similar dispersion, i.e., 0.38 mag using 40 SNe II ("full") or 0.22 mag after removing six outliers ("culled"). In Table 6.1 we present

Table 6.1. SCM-fit Parameters

Data Set	α	β	M_i	σ_{int}	SNe
Poznanski et al. (2009) “full”	4.4 ± 0.7	$0.6^{+0.3}_{-0.4}$	-17.42 ±0.10	0.35	40
Poznanski et al. (2009) “culled” (P09 culled)	4.2 ± 0.6	$0.8^{+0.3}_{-0.3}$	-17.38 ±0.08	0.20	34
SDSS from D’Andrea et al. (2010)	$1.8^{+0.9}_{-1.0}$	0.1 ± 0.5	$-17.67^{+0.11}_{-1.0}$	0.16	15
D’Andrea et al. (2010) + P09 culled	4.0 ± 0.7	$0.8^{+0.3}_{-0.3}$	-17.52 ±0.08	0.29	49
CSP	$3.04^{+0.47}_{-0.46}$	$1.54^{+0.38}_{-0.37}$	$-16.66^{+0.06}_{-0.06}$	$0.31^{+0.04}_{-0.03}$	40
CSP+SDSS	$3.16^{+0.42}_{-0.41}$	$1.02^{+0.28}_{-0.26}$	$-16.65^{+0.05}_{-0.05}$	$0.30^{+0.03}_{-0.03}$	56
CSP+SNLS	$3.05^{+0.45}_{-0.44}$	$1.42^{+0.34}_{-0.35}$	$-16.64^{+0.05}_{-0.06}$	$0.30^{+0.04}_{-0.03}$	45
CSP+SDSS+SNLS	$3.19^{+0.39}_{-0.40}$	$0.96^{+0.26}_{-0.25}$	$-16.63^{+0.05}_{-0.05}$	$0.29^{+0.03}_{-0.03}$	61

Note. — Best-fit values and the associated errors for each parameter of the SCM fit and using different samples.

the values of α, β, M_I, and σ_{int} from different works (values taken from Table 4 of D’Andrea et al. 2010) and using our different samples (CSP, SDSS-II, SNLS). As we can see in this table, the different parameters are not the same. For example, the discrepancy in the value of α could be explained by the method used. In this paper, we use the Hβ velocity while both other studies used the iron line. We also calculate a power-law for the majority of the SNe II for the velocity while both authors assumed a unique power-law for each SN. Thus, these differences could have an impact on the α value. For the $\mathcal{M}_{\lambda 1}$ as stated previously we do not correct the colour for intrinsic colour which could affect the value derived for the $\mathcal{M}_{\lambda 1}$. Additionally, the discrepancies on β and $\mathcal{M}_{\lambda 1}$ could arise from differences in the filters used. They used the Bessel filters R and I while we used the CSP filters r, and i.

Note also, that the differences of methodology are not the only cause affecting the SCM fit parameters. D’Andrea et al. (2010) explained that these effects could arise from selection effects as described in Section 6.2.1

We can also compare our distance moduli with those derived by Poznanski et al. (2009). Indeed, with Poznanski et al. (2009) we find two SNe II in the SNLS sample in common. For 04D1pj and 04D4fu, Poznanski et al. (2009) derived a distance moduli of 39.28 ± 0.11 and 38.85 ± 0.11 respectively. For the same SNe II we obtain 39.367 ± 0.084 for 04D1pj and 39.018 ± 0.087 for 04D4fu. For both SNe, the distance moduli obtained are consistent.

6.2.4 Hβ velocity: A and γ correlation

Pejcha & Prieto (2015) found a correlation between the two free parameters (A and γ) used in the expansion velocity formula described in equation 5.1. They found that velocity decays faster in SNe II with initially higher velocity. Using all the SNe II

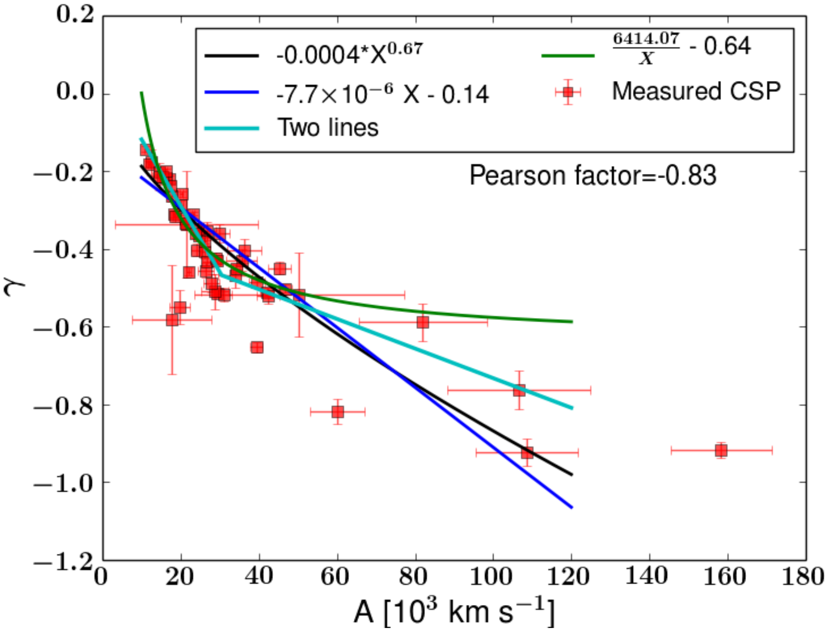

Figure 6.7: γ versus A using the CSP sample. The red squares represent the CSP sample, the black line a power-law fit, the blue line is a linear fit, the green line is an inverse fit, and in cyan a two lines fit.

from the CSP sample with more than three spectra, we present in Figure 6.7 the plot of the power-law exponent (γ) versus the initial velocity (A). As we can see, our observational data confirm the result found by Pejcha & Prieto (2015): SNe II with high initial velocity decay faster. Additionally, we remark that the shape of both relations (from Pejcha & Prieto 2015 and ours) is very consistent. The relation between these quantities is very important to derive the expansion velocity for the SNe II with only one spectrum. In the literature, the majority of the studies assumed the same power-law exponent for all SNe II or assumed a median value for the SNe II with only one spectrum (as done in Section 5.1). However thanks to this relation, we can derive the H_β velocity with more accuracy. In Figure 6.7 we show four different fits: a power-law (black), a linear fit (blue), an inverse fit (green), and a bi-modal fit (cyan). The best reduced chi square and dispersion are obtained using the bi-modal fit (16, 0.08 respectively). If the H_β velocities for the SNe II with only one spectrum are derived using the two lines fit, i.e., γ=-1.71×10^{-5} A + 5.25×10^{-2} for A$\leq$30500 or γ=-3.82×10^{-6} A -0.35 for A$\geq$30500, we are able to derive a Hubble diagram with an equivalent dispersion ($\sigma_{int} \sim 0.28$) than that derived in Section 5.4.2.

6.2.5 Sensitivity to progenitor metallicity?

Using theoretical models, Kasen & Woosley (2009) suggested that progenitors with different metallicities (Z =0.1-1 $Z_{\odot}$) could introduce some systematic errors (0.1 mag) in the expansion photosphere velocity-intrinsic luminosity relation. From an observational point of view, Anderson et al. (2016) and Taddia et al. (2016) using SNe II from the CSP and the intermediate Palomar Transient Factory (iPTF), respectively, showed that the equivalent width of the Fe II (EW_{Fe}) and the absolute magnitude at maximum peak are correlated in the sense of SNe II with smaller EW_{Fe} tend to be brighter.

In this part, we aim to study this using only the CSP sample, which is the only sample where metal line measurements are possible. We linearly interpolate the equivalent width to 45 days post-explosion and for this specific epoch, we end up with a sample of 25 SNe II.

Figure 6.8 shows EW_{Fe} versus the absolute Hubble diagram residual to the ΛCDM model (Ω_m=0.3 and Ω_Λ=0.7) and using the SCM. We find a trend between the EW_{Fe} and the absolute residual, i.e., SNe II with smaller EW_{Fe} have less dispersion. Note that no correlation was found between Hubble diagram residual and the EW_{Fe}. This figure could reflect the existence of one category of SNe II more standardisable than other, i.e., SNe II with small EW_{Fe} seem to be better standard candles than the others. It will be very interesting to construct a Hubble diagram using only SNe II with small EW_{Fe}, but unfortunately, we do not have sufficient SNe II yet. Note that adding another free parameter corresponding to $\gamma \times \mathrm{EW}_{Fe}$ to the SCM improve a little the intrinsic dispersion in the Hubble diagram (0.28 mag instead of 0.29 mag). Additionally, we confirm the correlation found by Anderson et al. (2016) and Taddia et al. (2016), more luminous SNe II have smaller EW_{Fe} at epoch 45 days post explosion. If we use the EW_{Fe} to standardise the SNe II instead of the colour correction, an intrinsic scatter of 0.35 mag is derived. Note that in our Hubble diagram (Figure 5.5), the high redshift SNe II (SDSS-II, SNLS) seem to have less intrinsic dispersion than the low redshift sample. This could be explained by the fact that high redshift SNe II have a smaller range in luminosity (Section 6.2.1), thus, a smaller range in EW_{Fe} which implies maybe less scatter.

If we use the equivalent width of the Fe II λ5018 absorption line as proxy for metallicity (Dessart et al., 2014), and if the Hubble diagram residual is only coming from the metallicity, we can conclude as Kasen & Woosley (2009) that differences in metallicity introduce some scatter in the Hubble diagram. The down side is that this correction does require a SN spectrum. All the figures and discussions regarding metallicity will be left for a future publication (Gutíerrez et al. in preparation).

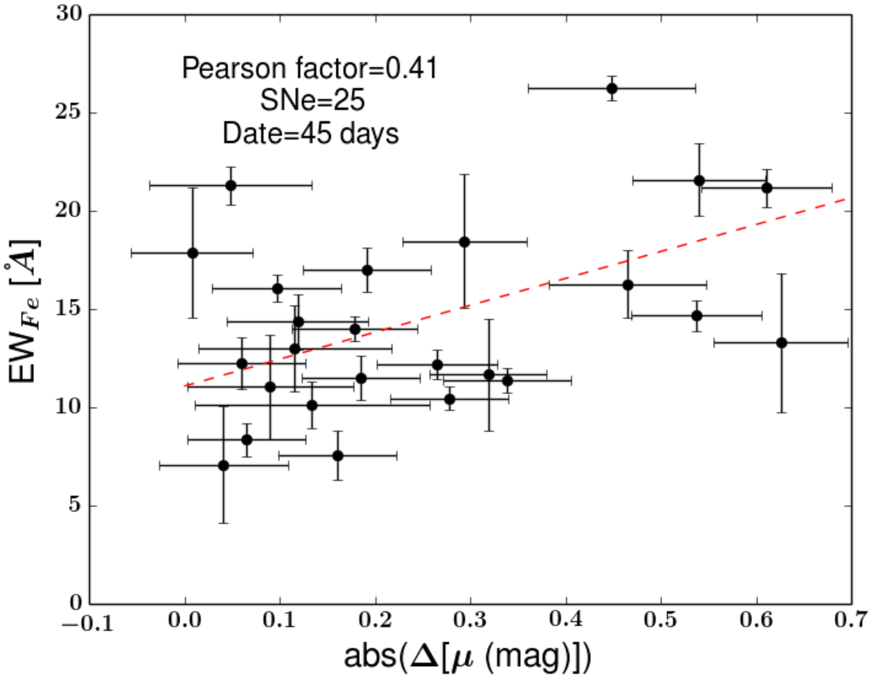

Figure 6.8: The absolute Hubble residual using the SCM and the ΛCDM cosmological model versus the equivalent width of the Fe II λ5018 absorption line.

6.2.6 Combined SNe Ia and SNe II Hubble diagram

In this section, we combine our SNe II sample with a complete SNe Ia sample (740 SNe Ia) from Betoule et al. (2014). In Figure 6.9, we show the combined Hubble diagram where both samples are fitted separately, i.e., using the distance moduli derived with the PCM for the SNe II and the distance moduli using the fitting parameters from Betoule et al. (2014) for the SNe Ia sample. Then, we try to fit simultaneously both samples following the work done by Scovacricchi et al. (2016) where they combined the SNe Ia sample and the SuperLuminous SNe sample. We minimise the likelihood corresponding to the product of two likelihoods $\mathcal{L} = \mathcal{L}_{Ia} * \mathcal{L}_{II}$. We have thus 9 free parameters: α, β, $\mathcal{M}_{\lambda 1}$, and σ_{int} for the two likelihoods plus the same Ω_m. Note that for the SNe Ia sample, we use the same likelihood used in equation 4.4 but, instead of the s_2 value or the Hβ velocities I use the stretch parameter. To estimate the effect of combining the two samples, we look at the value derived for Ω_m and especially its uncertainty. Using the PCM or the SCM the precision derived for the matter density with the combined samples is not better than the one obtained using only the SNe Ia sample. This can be easily explained by three different factors: the redshift range (SNe Ia up to 1.2), the size of the sample, and the fact that SNe Ia are better standardisable ($\sigma_{int} \sim$ 0.10-0.15 mag).

To compare the difference in precision achieved with the SNe Ia and SNe II, we restrict the SNe Ia sample to the same SNe II redshift range, i.e., $z \leq 0.5$. Doing

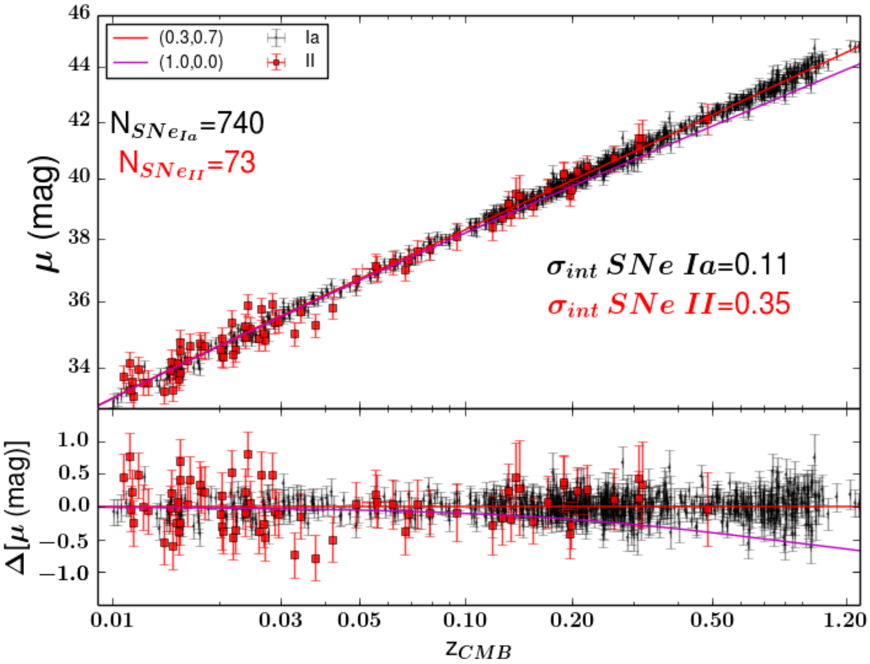

Figure 6.9: Combined Hubble diagram using SNe Ia from Betoule et al. (2014) and SNe II. The red squares are for the SNe II (using the PCM) and the black dots for the SNe Ia. Note that distance modulus errors for both methods include the intrinsic dispersion. The red line the Hubble diagram for the ΛCMB (Ω_m=0.3 and Ω_Λ=0.7) and in magenta line a Einstein-de Sitter cosmological model (Ω_m=1.0 and Ω_Λ=0.0)

a Monte Carlo simulation (hundred iterations), 73 SNe Ia (equivalent to the SNe II sample size) are randomly selected. A median uncertainty in the matter density of 0.1 is derived which compares to the $\sim$ 0.3 using only SNe II. Otherwise, we can count how many SNe Ia are necessary to reach a precision of $\sim$ 0.3 in the density matter comparing to the 73 SNe II needed. We find that 22 SNe Ia or 13 SNe Ia are required using the PCM and the SCM respectively which corresponds to $\sim$ 30 % (± 8%) or $\sim$ 20 % (± 7%) of the SNe II sample size for the PCM and the SCM respectively.

6.2.7 Malmquist bias

Using a basic simulation, I investigate the Malmquist bias, which leads to observe preferentially brighter objects in a magnitude limited survey. This bias implies a mean observed absolute magnitude brighter than the intrinsic mean, biasing distance measurements and therefore overestimating the matter density.

To derive an approximate Malmquist bias, I calculate the difference in magnitudes after applying the PCM (s_2 and colour corrections) of fake input SNe II distance modulus and output SNe II distance modulus, i.e., the SNe II which have passed the limiting magnitude cut of the survey. The (g, r, i, z) limiting magnitudes assumed are (25.5, 25.0, 24.8, 23.9) and (22.2, 22.2, 21.3, 20.5) for SNLS (1 hour exposure time) and SDSS-II ($\sim$ 55 seconds exposure time) respectively.

To generate fake apparent magnitudes, I adopt the low redshift sample distribution (CSP), i.e., the absolute V band magnitudes at the end of the plateau (M_{end}) between -15.0 and -17.0 (Anderson et al., 2014b). Using MC simulations and the correlation matrix between M_{end}, the s_2, the plateau duration (Pd), and the colours $(B-V)$, I generate 10 000 mock SNe II that follow the nearby distribution. Then, I select $\sim$ 2000 SNe II (i.e., $\sim$ 2000 set of M_{end}, s_2, Pd, $(B-V)$) from the MC simulation and for each SN II I use $\sim$ 2000 random redshifts between 0.03 and 0.80. From this, I can derive an apparent magnitude (i.e. $\sim$ 4 000 000 magnitudes) assuming a ΛCDM model and applying an inverse K-correction (similar to Section 3.3). Then, I compare the apparent magnitude (at the end of the plateau) with the limiting magnitude which depends on the redshift. For a redshift ≤ 0.3, an absolute magnitude in V band corresponds to an apparent magnitude in the r band, from 0.3<z<0.56 to the i band, finally from 0.56<z<0.80 to the z band. All the SNe II which pass this cut formed the output sample. From the input and output SNe II, I can derive the distance modulus after correcting the magnitude using $\alpha = 0.37$ and $\beta = 1.20$. The α and β values were derived using only the CSP sample and applying the PCM as achieved in de Jaeger et al. (2015b). The final Malmquist bias is taken as the mean value of the distance modulus difference of the input and output sample for a redshift bin of 0.02. Then, I interpolate linearly the Malmquist bias over all the bins in order to apply this bias to each SN of the SDSS and SNLS sample.

Roughly, for the SNLS survey, I derive a mean Malmquist bias of ~ -0.02 mag for a redshift range between 0.02 and 0.3. After this range, the mean Malmquist bias decreases up to ~ -0.16 mag for a redshift between 0.3 and 0.4 and finally to ~ -0.32 mag for a redshift between 0.4 and 0.5. Similarly, for the SDSS survey, I derive a mean Malmquist bias of ~ -0.08 mag for a redshift range between 0.02 and 0.1 and ~ -0.31 mag for a redshift range between 0.1-0.15. In Figure 6.10, I show the Malmquist bias for the different survey plus LSST versus the redshift.

The Malmquist bias is applied to each SN II. For this, to each SN II I add at the apparent magnitude the value of the Malmquist which corresponds to the SN II redshift. Then, I derive the matter density and compare it with the value obtained in Section 4.3. The matter density distribution shape is very similar to that derived in Figure 4.11 and the value obtained, $\Omega_m = 0.35^{+0.30}_{-0.22}$, is also very consistent. I caution the reader that even if the Malmquist bias seems not to affect the cosmology, the bias estimation is done using a simple method and should be calculated as done by Perrett et al. (2010) and simulating fake SN directly in the observed images.

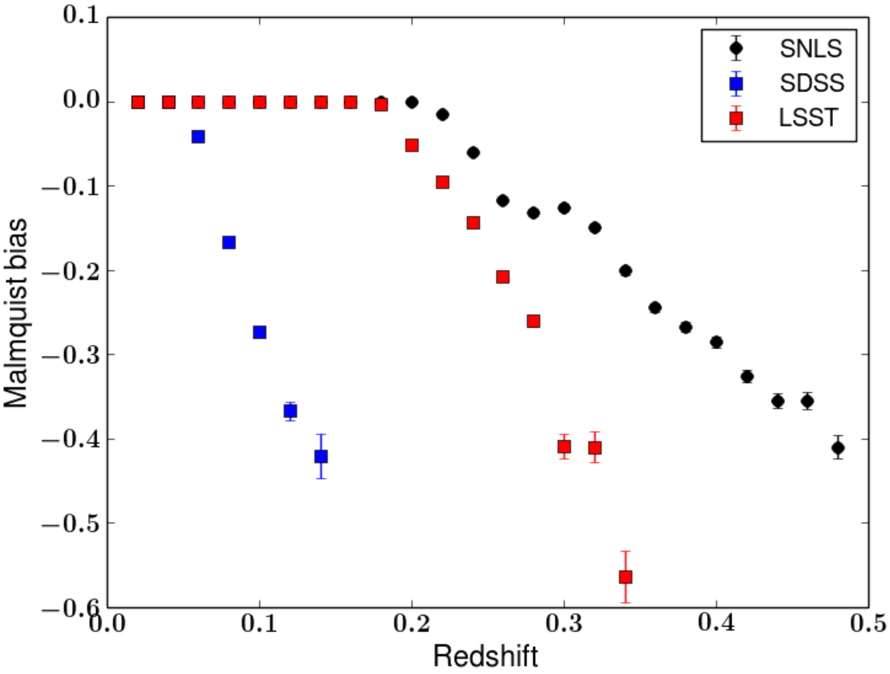

Figure 6.10: The squares represent the simulated Malmquist bias for the SNLS (black), SDSS-II (blue), and LSST (red) survey versus the redshift.

Chapter 7

Summary

In the first part of this dissertation, I used 39 SNe II at low redshift in the Hubble flow from the CSP sample in order to develop a new technique based solely on photometric data (PCM) to build a SNe II Hubble diagram. I also refined a pre-existing method using the photospheric expansion velocity (SCM) and compared both methods. The main conclusions from the first part of my thesis are the following.

1. For the first time a new method using solely the colour and the slope of the plateau allows us to reduce the scatter in the Hubble diagram to 0.41 mag using the r band and 0.40 mag with the Y band.
2. The s_2 slope plays a useful role, allowing us to reduce the dispersion from 0.56 mag to 0.46 mag for r band.
3. The colour term does not have so much influence on the NIR filters because it is related to the host-galaxy extinction which is less in the NIR.
4. I find very low (β) values (the colour-magnitude coefficient). If β is purely extrinsic, it implies very low R_V values. In the Appendix, I show a preliminary work done during this thesis.
5. The Hubble diagram derived from the CSP sample using the SCM yields a dispersion of 0.28 mag, somewhat better than those found in the literature and emphasising the potential of SCM in cosmology.
6. Using the SCM and NIR filters the scatter does not show a strong improvement as suggested by some authors.

In the second part of this thesis, I used a larger data sample composed of three sub-samples: CSP, SDSS, and SNLS. This data sample is the largest SNe II sample known in the literature. I successfully extended the PCM to higher redshift and thus construct the most complete SNe II Hubble diagrams. I also applied the SCM to this large sample. The main conclusions of the high redshift part are:

1. I applied the PCM and found an intrinsic dispersion of 0.35 mag using the i band. The PCM reduced the scatter in the Hubble diagram of 0.2 mag and allows us to derive distances with a precision of 16 %.
2. Using the PCM I derived cosmological parameters (Ω_m) consistent with the ΛCDM model. I found Ω_m=$0.33^{+0.29}_{-0.21}$, which implies a dark energy parameter of $0.67^{+0.21}_{-0.29}$. These results are consistent with the existence of the dark energy at two sigma.
3. Using the SCM, I also derived cosmological parameters (Ω_m) consistent with the ΛCDM model. I found Ω_m=$0.39^{+0.31}_{-0.26}$, which implies a dark energy parameter of $0.61^{+0.26}_{-0.31}$.
4. The Hubble diagram derived from the CSP+SDSS-II+SNLS samples using the SCM yields a dispersion of 0.27 mag which is similar than those found in the literature and emphasises the potential of SCM in cosmology.
5. We find a relation between the power-law exponent (γ) and the initial velocity (A) which is very useful to derive H_β velocities at any epoch with only one SNe II spectrum.
6. The distance moduli derived using the PCM and the SCM are very consistent with a dispersion of 0.29 mag.

The main conclusion of this thesis is that using an independent and new method I derived cosmological parameters consistent with the current cosmological model and show the existence of the dark energy at two sigma. The PCM is a very promising method as shown and allows us to add more SNe II for which spectra were not obtained. This is very important in the coming era of large photometric wide–field surveys like LSST, for that having spectroscopy for every SNe will be impossible hence the PCM which is the first purely photometric method could be very useful.

Appendix A

Host galaxy extinction

For my thesis project, I worked few months on the host galaxy extinction (Avh) probing five different methods, two spectroscopic and three photometric. The Avh is very difficult to estimate but it is the key to decrease the Hubble diagram dispersion further. In this Appendix, I will show my preliminary work on the Avh and intrinsic colour which hopefully will lead to a future publication. For this work, I use only the CSP sample and the SNe II with optical and near-infrared data. Note also that in this appendix, I use as reference epoch OPTd-X days and not OPTd*X% as done in Section 4.2. This study was done before the cosmology work and should be done using the same reference in a near future.

The host galaxy extinction is a crucial parameter in astronomy which describes how much light is absorbed by dust grains. Dust grains represent only about 1% of the mass of the interstellar medium (99% gas) and have a size distribution from angstroms to ~ 0.3 μm. Generally, they are formed by carbon or silicate core surrounded by an icy mantle of water ice, methane, carbon monoxide, and ammonia. First introduced by Trumpler (1930), the Avh which is greater in the blue part of the electromagnetic spectrum (Rayleigh scatter $A_\lambda \propto \lambda^{-4}$) makes the object appears redder than it would have been otherwise. The estimation of this interstellar reddening is very important and allows us to derive the absolute magnitude of an object and therefore obtain its distance. Its estimation is also useful to understand the intrinsic properties of SNe II like the intrinsic brightness distribution which gives valuable properties of the explosion and progenitor star. One classical parameter used to characterise the extinction law is its slope called R_V, the ratio of total-to-selective extinction. This quantity is dimensionless and defined as the extinction measured in the V band (A_λ) divided by the colour excess $E(B-V)$: $\mathrm{R}_V=\mathrm{A}_\lambda/E(B-V)$. This slope is directly related to the size grain: smaller grain sizes would make this slope steeper (small R_V), whereas very large grains (approaching the Mie regime) would produce grey extinction, i.e., $\mathrm{R}_V \rightarrow \infty$ and are found in denser regions (Draine, 2003).

In recent decades, many efforts have been made to find a relationship to determine the host extinction. There are mainly two ways in order to estimate the Avh: the spectroscopic or the photometric methods. In this appendix, I do a review of the most used methods found in the literature, beginning with the spectroscopic techniques and following by those photometric. Note that in this work I assume a Cardelli et al. (1989) law and $R_V = 3.1$ excepted when it is mentioned.

A.1 Spectroscopic methods

In this part I use hundreds of spectra from the CSP sample, i.e., SNe II from Table 2.1 with a note mark. The reader can found more information like the classification reference, the number of spectra for each SN II, in Table 3 from Anderson et al. (2014b).

A.1.1 Na I D measurement

One of the most used methods to estimate the Avh is to measure the strength of the sodium Na I doublet absorption ($\lambda\lambda 5889.95, 5895.92$). The Na I D equivalent width (EW) is correlated with the amount of dust along the line of sight. Using low resolution spectra, various authors have found some relation between the colour excess $E(B-V)$ and the EW. One of the first relation was established by Barbon et al. (1990), where the authors concluded that the $E(B-V) \sim 0.25$ EW (Na I). Similar relation was found also by Turatto et al. (2003) ($E(B-V) \sim 0.16$ EW (Na I) - 0.01). However, the validity of using the EW for low resolution spectra has been questioned (Phillips et al., 2013; Poznanski et al., 2011). Poznanski et al. (2011) showed that the EW Na I/$E(B-V)$ correlation using low resolution spectra is so much scattered that the method is useless.

From all the relation available in the literature, I use the Turatto et al. (2003) relation. All the spectra have been taken in low resolution, and the majority of them have an EW larger than 1 Å which prevents the use of the most recent relation (Poznanski et al., 2012), available only for small EW. All the host galaxy extinction measured and the associated errors using the Na I equivalent width are shown in the second column of Table A.1. Note that the errors were derived as done for the velocity measurement by varying the continuum.

A.1.2 Models fitting.

The second spectroscopic method used to estimate the Avh is with theoretical models. SNe II atmosphere models are now able to reproduce with an amazing accuracy observed spectra (Dessart & Hillier, 2006; Dessart et al., 2008). This method consists of fitting my spectra library with one SNe II theoretical model without any extinction and trying to obtain the best fit by reddening the model. One important thing is that the continuum of a spectrum is affected by the reddening but also the temperature. To be sure that the difference between the theoretical and the observed spectrum is only due to the reddening, we can use the spectral lines to constrain the photometric temperature. Then the continuum is employed to estimate the extinction. Because each SN II evolves at different velocities we cannot use the observed spectrum epoch to fix the temperature.

I develop a Python program which allows me to estimate automatically the host galaxy extinction. First, I select only the observed spectra with a wavelength range including at least V, r, i–bands (4760–8630 Å) in order to do a flux calibration. I include also only the spectra with an epoch range from 15 days after the explosion to the end of the plateau (Optd $\sim$ 80 days). Secondly, I do a flux calibration of each observed spectrum using synthetic magnitudes and compare them to the observed magnitudes linearly interpolated to the spectrum epoch. This operation is important due to possible modification of the relative shape of the spectrum. These variations could be the result of contamination by the light from the host galaxy or because the slit and the object were not perfectly aligned. To calculate the synthetic magnitudes, I use all the filters available for each spectrum. From the difference between the synthetic and observed magnitude I obtain the color-matching function (quadratic, cubic depends on the number of filters used) and do a constant extrapolation for the parts of the spectrum which are not covered by the filters used.

After checking the flux calibration, the next step is to correct for Galactic absorption (using the Cardelli et al. 1989 law with $R_V = 3.1$) and deredshift the spectrum. I also smooth the spectrum obtained and cut the extremity of the spectrum when some aberrations (board effect) are presents. Additionally, I remove the telluric lines ($\sim$ 7605 Å; O_2) with a linear interpolation to be consistent with the model (not telluric lines are present).

The last step consists of comparing the observed spectrum after all the corrections above and the model. To find the best fit I use three free fitting parameters: the host galaxy extinction, the factor of normalisation and the epoch of the model. The parameters are fitted using a constrained Levenberg-Marquardt least-squares minimisation algorithm. The function to minimise is the chi–squared where the error on the observed flux is taken as 5% of the mean flux. For each set of parameters, the algorithm compared the same 15 bins of each spectrum (observed and theoretical). For each bin, I do an average of the flux. The standard errors on the host galaxy extinction are the square-root of the diagonal elements of the covariance matrix multiply by reduced chi–square. Note that I tried various size of bins and for a larger number of bins the algorithm gives me very bad fit. In Figure A.1, I present an example of the result given by the algorithm. We can see that the model fits very well the observed spectrum. For each SN II, I obtain various values of the host galaxy extinction (one per spectrum) at different epochs. Some of these values were removed after a sanity check of the fit quality by eye. Then the final host galaxy extinction and the associated error are obtained by doing a weighted average and standard deviation of all the values remaining.

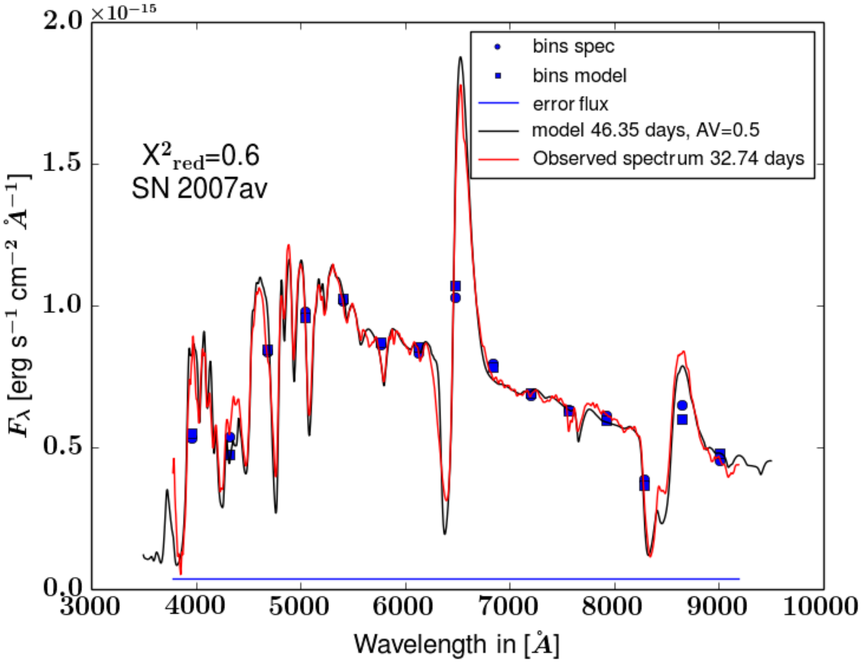

Figure A.1: In red I present the observed flux of SN 2007av with an epoch 32.74 days after the explosion. This spectrum is corrected for Milky Way extinction and for redshift. In black the model at the epoch 46.35 days is represented. The model is reddened with an extinction of A_V=0.50. The blue circles and squares represent for each bin respectively the mean observed flux and the average of the flux model. The blue line is the error on the observed flux chosen. The reduced chi–squared is also represented.

For some SN II, only one spectrum was available thus, as error, I use the mean of all the errors from the entire sample.
As theoretical model, a supernova progenitor with a main–sequence mass of 15 $M_\odot$ and a solar metallicity, Z=0.002, zero rotation and a mixing–length parameter of 3 is used. More information about this model (named m15mlt3) are provided in Dessart et al. (2013), and especially in Table 1. I also tried three other models with different metallicities (m15z2m3, m15z8m3, m15z4m2) and in Figure A.2, I show the comparison between the two models. We can see that the values found with the two different models are very consistent. In the following for the comparison and in Table A.1 I only use/show the values found using the model m15mlt3.

A.2 Photometric methods

In this part, I will explore three photometric methods using 51 low redshifts SNe II with optical and NIR filters. Derive photometric methods to estimate the host galaxy

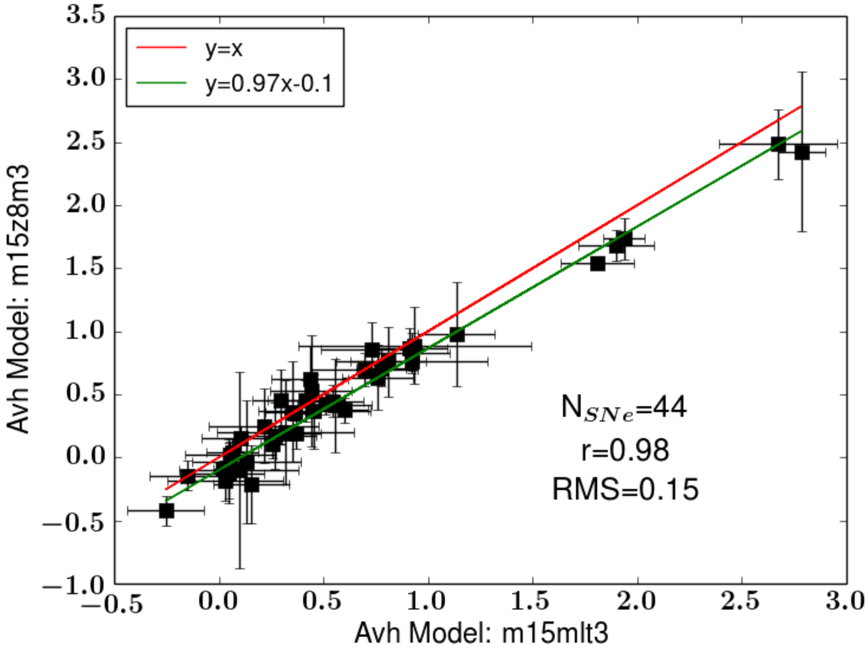

Figure A.2: The difference of host galaxy extinction using two models. In x–axis I use the model m15mlt3 whereas in y-axis the model m15z8m3. The green line is the weighted least–square fit to the data with a slope of 0.97 ± 0.02 and a zero point of -0.09 ± 0.03. The red line represents the 1:1 line. The Root Mean Square (RMS), the Pearson factor (r) and the number of SNe II are also represented in the figure.

extinction are very important tools for the next generation surveys. These techniques will allow us to characterise SNe II properties without the need of acquiring spectrum, which requires a lot of observing time. For the photometric methods, I assume that all SNe II should evolve from a hot initial stage to one of constant photospheric temperature, due to the hydrogen recombination. This implies that all SNe II reach the same colour at a certain epoch and that colour differences between SNe II are dominated by differences in extinction and not intrinsic colour differences. To verify the assumption the colour-colour plot is a good diagnostic in which unreddened SNe II should occupy a small region in the bottom left on the plot, i.e., the blue part. Before using the photometric methods to estimate the host galaxy extinction, I correct the observed photometry by two factors, the Milky Way (MW) extinction and the K-Correction (KC) as done in de Jaeger et al. (2015b).

A.2.1 Colour-time method

In the following, to estimate the Avh I use the photometric method developed by Olivares et al. (2010). I will quickly describe this technique and the reader can find more information on the article referenced. The key of this method is to pick a single epoch in the colour evolution to avoid the fact that the colour curve shape can vary from SN II to SN II.
First, we need to find this best single epoch. For this, I investigate many filter combinations and plot the colours-colours diagram at different epochs. For each set of colours, the best epoch is choosing as the one for which the dispersion is the smallest. In the Figure A.3, I show one of the best fit obtained using the colours $(V-i)$ and $(V-Y)$ for an epoch of 23 before the OPTd. Note that, this epoch is consistent with Olivares et al. (2010), who found as best epoch the middle of the transition phase minus 30 days ($(V-R)$ versus $(V-i)$). We can verify and look if the unreddened SNe II occupy the bottom left on the colour-colour plot. In my sample, I can guess which SNe II should have low Avh. To select these SNe II, I use different criteria. First using the spectra, I select only the SNe II showing few Na I D absorption. Second, I select the SNe II located away from the nuclei of spiral galaxies (less dust), and finally, only SNe II with a good sample are chosen. Using this, I adopt 5 unreddened SNe II: SN2004fx, SN2005dk, SN2007aa, SN2008M and SN2008ag. These five SNe II are shown in blue in Figure A.3 and as expected are situated in the bottom left of the plot. With the five unreddened SNe II, I can estimate an intrinsic colour $(V-Y)_0$ taking as the average of the five colours ($(V-Y)_0 = 0.725$). Using the correlation between the colour excess and the Avh,

$$
\begin{aligned}
\beta_V =& \frac{A_V}{E(V-Y)} = \frac{A_V}{A_V - A_Y} \\
\beta_V =& \frac{1}{1-(a_Y + \frac{b_Y}{R_V})},
\end{aligned}
\tag{A.1}
$$

where a_Y and b_Y are the Cardelli et al. (1989) coefficients and can be derived using my theoretical spectra library. I finally obtain the β_V value assuming R$_V$ = 3.1 and find $\beta_V = 1.61$.
To finish, I obtain the Avh and the associated error as:

$$
\begin{aligned}
A_V =& \beta_V \times [(V-Y) - (V-Y)_0] \\
\sigma_{A_V} =& \beta_V \times \sqrt{\sigma^2_{(V-Y)} + \sigma^2_{(KC)} + \sigma^2_{(RMS)}},
\end{aligned}
\tag{A.2}
$$

where $(V-Y)$ is the colour of a given SN II at epoch OPTd-23 days and σ_{A_V} is a combination of the instrumental errors in the V and Y magnitudes, the RMS of the colour-colour plot and the errors of the AKS terms. The Avh found using this method is listed in Table A.1 in column 4.

A.2.2 colour-colour method

Recently a new photometric method to estimate the host galaxy extinction has been proposed by Rodríguez et al. (2014) called C3 method (colour-colour curves). This method based on the fact that the majority of the SNe II show the same color-color diagram (CCD) with a linear evolution. Thus, the SN II cooling curve (CC) without extinction can be written as:

$$
(X1-Y1)_0 = b_0 + a_0 \times (X2-Y2)_0 \tag{A.3}
$$

where $(X1-Y1)_0$ and $(X2-Y2)_0$ are two set of colours without extinction. Assuming that the SNe II have the same CCD, i.e, the same slope, any difference in Avh will result in a difference in the zero point. Therefore, the extinguished SNe II will move on the right and upward colour-colour plot. This effect is illustrated in Figure A.4, where using our SN II theoretical spectra library (only epoch between 20 and 80 days after the explosion), I apply 10 synthetic extinctions (from $A_V = 0$ mag to $A_V = 2.0$ mag by step of 0.2 mag). As we clearly see in this figure, when the extinction increases, only the zero point of the linear fit changes and the photometric points are moving to the top right of the CCD. The slope remains mainly constant when the Avh increases (slope range from 1.37 to 1.32).

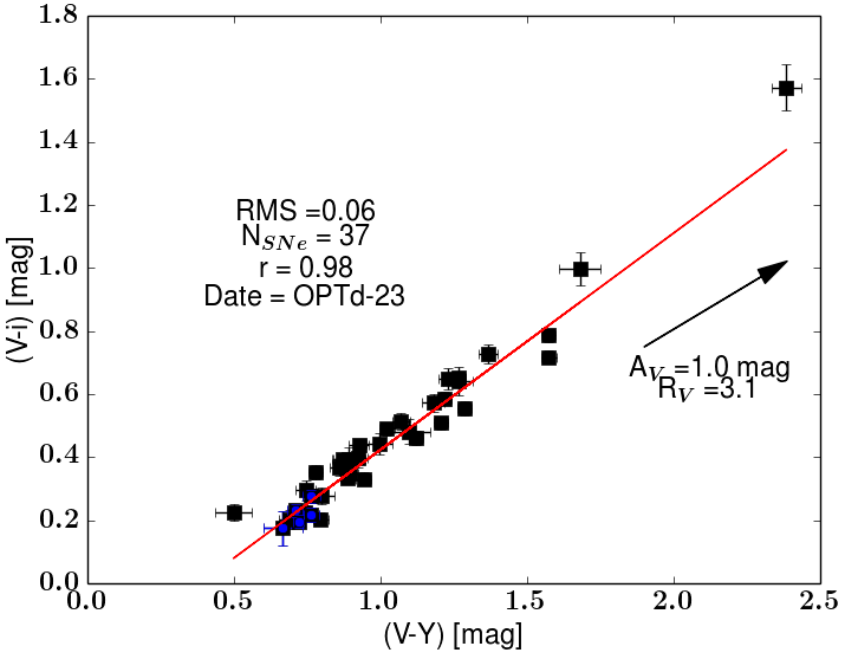

Figure A.3: $(V-Y)$ vs $(V-i)$ diagram for 37 SNe II after corrected for AKS and at an epoch of OPTd-23 days. The arrow has a slope of 0.565 and corresponds to the reddening vector for $A_V = 1.0$ mag and a Cardelli et al. (1989) extinction law ($R_V = 3.1$). The blue circles show the six SNe II consistent with zero Avh. The red line is the weighted least–square fit to the data with a slope of 0.696 ± 0.021 and a zero point of -0.308 ± 0.021 . The Root Mean Square (RMS), the Pearson factor (r) and the number of SNe are also represented in the figure.

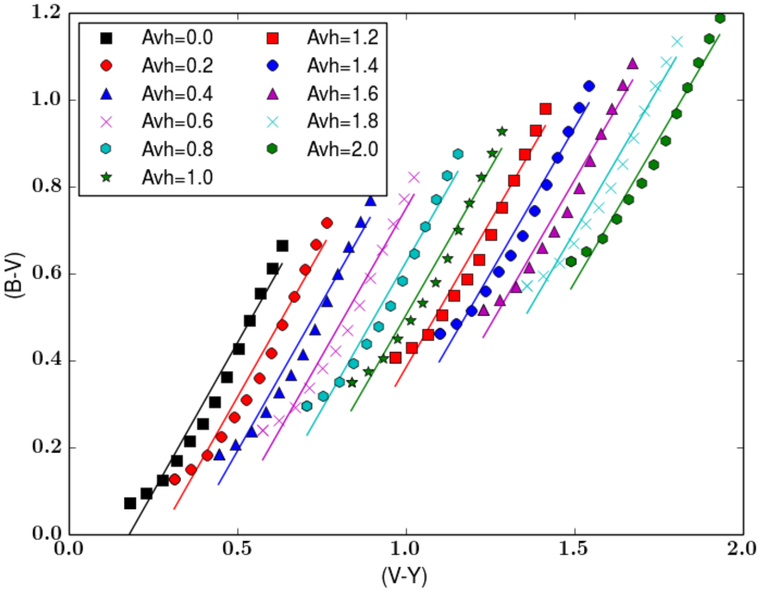

.

Figure A.4: $(B-V)$ vs $(V-Y)$ diagram using our theoretical model. I apply different synthetic extinctions (from 0.0 to 2.0 mag). The black squares represent the raw SNe II, i.e, without any reddening. In each case, the straight line represents the slope of our model without extinction.

For an extinguished SNe II, the CC can be written as a linear function with the same slope:

$$(X1 - Y1) = b_{new} + a_0 \times (X2 - Y2) \tag{A.4}$$

where (X1-Y1) and (X2-Y2) are the colours affected by the extinction, and b_{new} the new zero point.
From my data set, after trying many colour combinations I select three set of colour-colours : $(B-V)$ versus $(V-Y)$, $(B-V)$ versus $(V-i)$ and $(g-i)$ versus $(V-Y)$. I select these set of colours because they include optical and NIR filters or because looking at the theoretical simulations, the slope is constant with the extinction, which is not the case for others combinations where an evolution can be seen. The method is only applied during the plateau phase. I cut the epochs between 20 days after the explosion date to the end of the plateau (OPTd) or 80 days after the explosion (as for the spectroscopic method). The choice of 20 days is arbitrary but by looking at all the SNe II CCD, I find that this value seems a good approximation due to the fact that the evolution is more linear after this epoch. Note that, I remove from the sample all the SNe II with small baseline in colours, SNe without linear evolution and SNe with only one point in the CCD. First, I fit the observed data by a straight line I perform a weighted chi-square minimisation in order to derive the common CC slope of all the

SNe II :

$$\chi^2 = \sum_{i=1}^{N} \frac{(y_i - (ax_i + b))^2}{\sigma_{y_i}^2 + a^2 \times \sigma_{x_i}^2} \tag{A.5}$$

where x_i, y_i are the colours corrected by AKS and σ_{x_i}, σ_{y_i} the errors associated. The errors on the colours are simply the quadratic sum, i.e, for example $\sqrt{\sigma_B^2 + \sigma_V^2}$. To obtain the uncertainties in both parameters I perform also a Monte Carlo simulation varying randomly each photometric point according to the photometric uncertainties. The errors are taken as the standard deviation. Supposing that all the SNe have the same cooling curve, I use the weighted average slope as the common slope, i.e., a_0 value in equation A.4. However, there are some intrinsic differences in slope due to the variations in each SN II of the line profile formation. This dispersion on the slope is taken as the error on the mean slope. In Figure A.5, I show the distribution of the slope using $(B - V)$ versus $(V - Y)$ and the CCD.

Now that I have the averaged slope, I will fit again all the SNe II but this time I fix the slope and only keep the zero point as a free parameter because it will be the only parameter affected by the extinction. I apply the same method that I described above and derive a new value for the zero point (b_{new}). As seen in Figure A.5, the distribution of the cooling curve slope is broad and thus, we need a test to the goodness of this new fit. For this, I use a F-test defined as the division between the $\chi^2_{a,b}$ reduced calculating when the slope and the zero point ("a" and "b") are free parameters and the χ^2_b reduced when only "b" is a free parameter,

$$F = \frac{\chi^2_{a,b}}{\nu^2_{a,b}} \frac{\nu^2_b}{\chi^2_b} \tag{A.6}$$

where $\nu_{a,b}$, ν_b are the degrees of freedom, i.e, numbers of points - 2 and numbers of points - 1 respectively. If the result, F is close to 1, this means that both χ^2 are similar because $\nu_b/\nu_{a,b} \approx 1$, so fixing "a" and fit only "b" is a good approximation. I decide to keep only the SNe II with a value of F superior to 0.3.

Finally, to obtain the colour excess, one need to find in the data set the SNe II with the smallest reddening. For this, we need to look at the value of the mean slope and the reddening vector, define as:

$$E^{X1Y1X2Y2} = \frac{E(X2 - Y2)}{E(X1 - Y1)} \tag{A.7}$$

I choose as the unreddened SN II the one with the lowest zero point (b_{new}) if the slope of the reddening vector ($E^{X1Y1X2Y2}$) is larger than mean slope (a_0), or the one with the highest b_{new} if the slope of the reddening vector is lower than a_0. We can obtain the colour excess with respect to this low reddening SNe II and convert it in Avh using a reddening law as Cardelli et al. (1989).

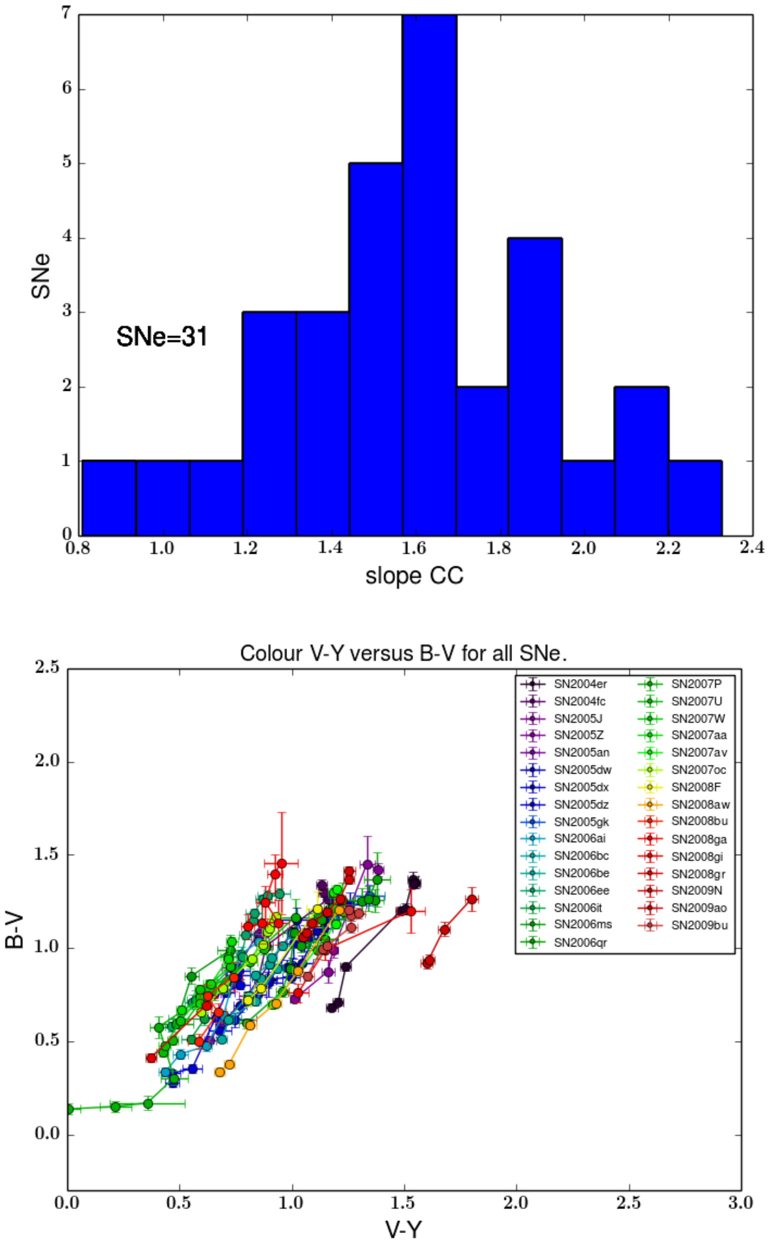

Figure A.5: *Top:* $(B-V)$ vs $(V-Y)$ diagram using the CSP sample. *Bottom:* Distribution of the cooling curve slope for all the SNe II available for this colour combination.

$$E(X1 - Y1) = \frac{(b_{new} - b_0)}{(E^{X1Y1X2Y2} - a_0)}, \tag{A.8}$$

where b_{new} is the zero point using the mean slope, b_0 is the zero point of the unreddened SNe II, a_0 the mean slope and $E^{X1Y1X2Y2}$ the reddening vector.

A.2.3 Multi bands fit method

The last photometric method used takes advantage of the availability of photometric data spanning the blue band through NIR band. This technique used by Folatelli et al. (2010) allows us to derive the Avh but also the R$_V$ for each SNe II. For a specific epoch, I plot the colour excesses $E(V-X_\lambda)$ as a function of the effective wavelength of each filter X$_\lambda$, where X$_\lambda$=u, B, g, r, i, Y, J, H. To derive the colour excess , i.e., for the intrinsic colour, I use the same low reddening SNe II taken in Section A.2.1. Figure A.6 shows the colour excesses versus the effective wavelength of each filter for SN 2009N at a specific epoch OPTd-35 days, which corresponds to the plateau phase. The best fit is obtained doing a least-square minimisation using the Cardelli et al. (1989) modified reddening law from O'Donnell (1994), called CMM+O.The final Avh is obtained doing a median of the values derived during the plateau phase and are shown in the last column of the Table A.1.

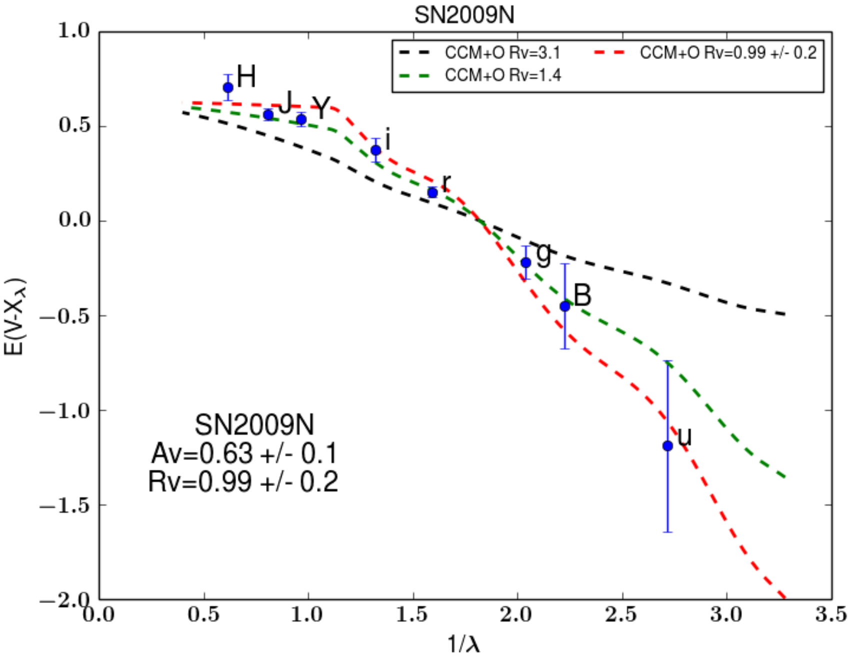

Figure A.6: Color excesses $E(V-X_\lambda)$, for bands X$_\lambda$=$ugriBYJH$, for SN 2009N. The red dashed line shows the best-fit CCM+O laws, whereas the black and green lines show the CCM+O model for R$_V$= 3.1 and R$_V$= 1.4 respectively.

Table A.1. Host galaxy extinction

SN	A_V(NaID)	A_V(Spectrum) mag	A_V(colours) mag	A_V(CCC) mag	Excess colours mag
2004er	0.121(0.065)	1.786(0.34)	1.284(0.143)	1.615(0.538)	1.516(0.21)
2004fc	0.405(0.085)	0.79(0.133)	···	0.614(0.21)	0.565(0.214)
2004fx	0(0.015)	0.065(0.136)	-0.027(0.143)	···	0.239(0.096)
2005J	0.096(0.11)	0.289(0.378)	0.13(0.144)	0.314(0.116)	0.138(0.074)
2005Z	0.537(0.169)	1.221(0.147)	0.948(0.144)	1.242(0.415)	0.842(0.022)
2005an	0.361(0.088)	0.607(0.283)	0.39(0.143)	0.685(0.233)	0.57(0.354)
2005dk	0.181(0.015)	-0.064(0.078)	-0.027(0.144)	···	-0.079(0.033)
2005dn	0(0)	···	0.709(0.143)	···	0.684(0.069)
2005dw	0.434(0.008)	0.534(0.147)	0.648(0.146)	0.854(0.287)	0.679(0.045)
2005dx	0(0.015)	0.155(0.147)	0.509(0.159)	0.666(0.231)	0.577(0.042)
2005dz	0(0)	0.344(0.165)	0.028(0.147)	0.520(0.180)	0.07(0.03)
2005es	0(0.015)	···	···	···	0.411(0.240)
2005gk	0(0.015)	···	···	1.172(0.397)	0.685(0.623)
2005lw	0.535(0.09)	1.579(0.147)	1.456(0.157)	···	1.508(0.273)
2006Y	0(0.015)	···	-0.149(0.145)	···	···
2006ai	0(0.015)	0.335(0.069)	-0.062(0.144)	0.521(0.180)	0.187(0.069)
2006bc	0.386(0.013)	···	···	0.871(0.293)	0.32(0.327)
2006be	0(0)	0.558(0.208)	0.261(0.143)	0.648(0.220)	0.338(0.05)
2006bl	0(0.015)	0.161(0.098)	···	···	0.799(0.681)
2006ee	0(0)	0.01(0.217)	0.146(0.144)	0.112(0.062)	-0.11(0.055)
2006it	0(0)	-0.225(0.147)	···	0.308(0.119) ···	
2006ms	0(0.015)	-0.276(0.052)	···	0(0.066)	-0.051(0.086)
2006qr	0(0)	···	0.784(0.150)	0.972(0.326)	0.775(0.063)
2007P	0(0)	···	0.182(0.151)	0.165(0.081)	-0.1(0.047)
2007U	0(0.015)	···	0.235(0.144)	0.285(0.107)	0.268(0.209)
2007W	0(0)	···	-0.058(0.145)	0.172(0.076)	0.025(0.029)
2007aa	0(0)	0.036(0.021)	-0.117(0.143)	0.126(0.065)	-0.081(0.021)
2007ab	0(0.015)	···	0.728(0.145)	···	0.778(0.476)
2007av	0.203(0.046)	0.551(0.143)	0.688(0.143)	0.913(0.307)	0.672(0.059)
2007hm	0(0.015)	···	-0.185(0.155)	···	0.12(0.294)
2007il	0(0)	0.342(0.077)	0.23(0.144)	···	0.283(0.113)
2007oc	0(0.015)	0.321(0.194)	0.189(0.143)	0.356(0.128)	0.194(0.045)
2007od	0(0.015)	0.22(0.12)	0.174(0.143)	···	0.244(0.222)
2007sq	0.704(0.114)	2.696(0.147)	2.597(0.149)	···	2.565(0.136)
2008F	0(0.015)	···	···	0.745(0.254)	0.364(0.474)
2008M	0(0)	···	-0.097(0.142)	···	0.072(0.03)
2008W	0.256(0.015)	···	0.47(0.144)	···	0.641(0.123)
2008ag	0(0)	0.142(0.222)	-0.002(0.143)	···	-0.271(0.077)

Table A.1 (cont'd)

SN	A_V(NaID)	A_V(Spectrum)	A_V(colours)	A_V(CCC)	Excess colours
		mag	mag	mag	mag
2008aw	0.117(0.016)	0.880(0.019)	0.551(0.143)	1.037(0.347)	0.671(0.131)
2008bh	0.275(0.024)	1.839(0.064)	···	···	1.524(0.168)
2008bk	0(0)	···	1.863(0.143)	···	···
2008bu	0(0)	0.425(0.147)	-0.457(0.154)	0.628(0.217)	···
2008ga	0(0.015)	0.767(0.147)	0.350(0.147)	···	0.28(0.159)
2008gi	0.198(0.021)	0.788(0.147)	···	···	···
2008gr	0(0.015)	0.292(0.191)	···	0.17(0.079)	-0.054(0.113)
2008hg	0(0.015)	0.467(0.147)	···	···	-0.041(0.087)
2009N	0.0465(0.057)	0.57(0.246)	0.787(0.143)	0.806(0.272)	0.659(0.029)
2009ao	0.49(0.04)	2.743(0.054)	1.284(0.143)	2.41(0.800)	0.854(1.146)
2009bu	0(0.015)	0.895(0.145)	0.821(0.143)	1.145(0.383)	0.825(0.206)
2009bz	0(0.015)	0.264(0.062)	0.026(0.143)	···	0.081(0.08)

Note. — Host galaxy extinction. In the first column the SN II name, followed by its reddening due to dust in the host galaxy measured using the Na I EW method. In column 3 host galaxy extinction using theoretical spectrum. In columns 4 I use the colours method to estimate the extinction in the host galaxy as Olivares et al. (2010). And to finish in columns 5 I present the reddening using the colour-colours method as in Rodríguez et al. (2014).)

A.3 Comparisons and conclusions

Figure A.7 shows the comparison between all these methods. As we can see, all these methods are very consistent and obtain similar host galaxy extinction. However, it is important to note that the photometric methods are very dependent of the intrinsic colours. In the future, we need to investigate the intrinsic properties of the SNe II better in order to derive more accuracy Avh. Finally, it would be interesting to refine the multi bands fit method to derive a R_V different for each SN II and construct a new Hubble diagram. Indeed, due to the difficulty in understanding the host galaxy extinction, I assumed, throughout my whole thesis, the same total-to-selective extinction for all the SNe II which is not accurate. All the SNe II arise from different host galaxy and thus different dust nature, so it would be better to derive a R_V for each SN II.

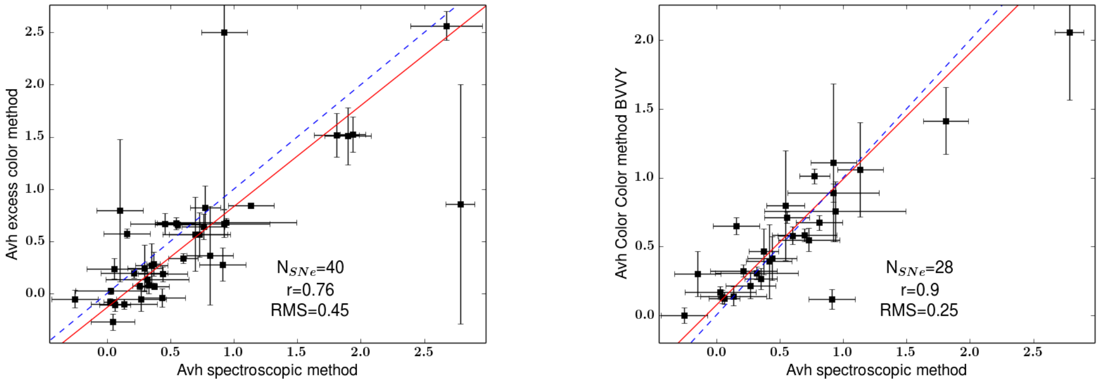

(a) Excess colour method vs spectroscopic method

(b) Colour colour method vs spectroscopic method

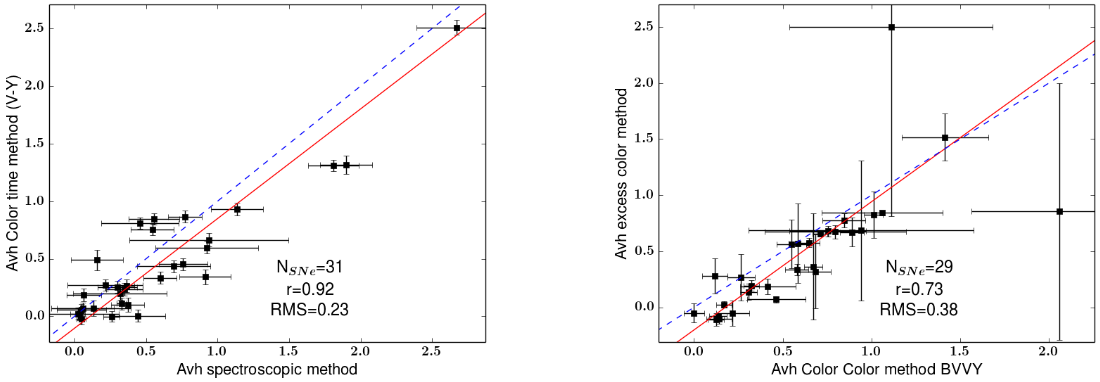

(c) Colour time method vs spectroscopic method

(d) Excess colour method vs Colour colour method

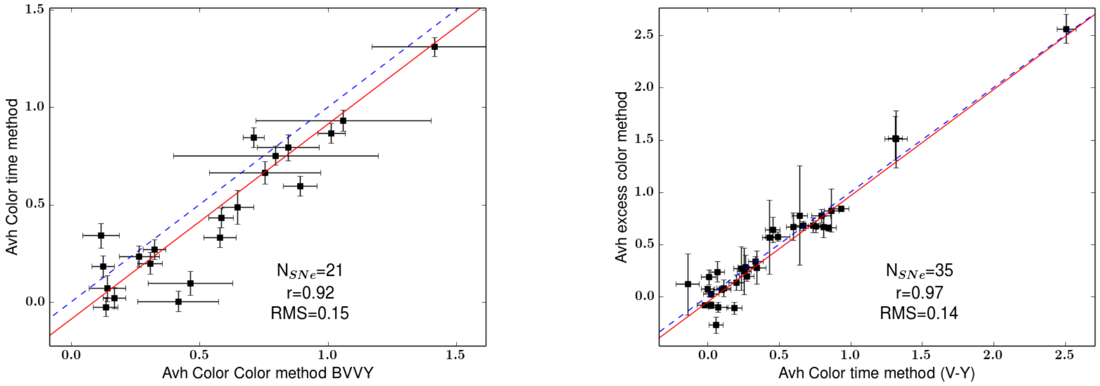

(e) Colour time method versus Colour colour method

(f) Excess colour method versus Colour time method

Figure A.7: Comparison of the Avh derived using different methods. The blue dashed line shows the 1 to 1 fit (x=y) while the red line is a linear fit.

Bibliography

Anderson, J. P., Dessart, L., Gutierrez, C. P., et al. 2014a, MNRAS, 441, 671

Anderson, J. P., González-Gaitán, S., Hamuy, M., et al. 2014b, ApJ, 786, 67

Anderson, J. P., Gutierrez, C. P., Dessart, L., et al. 2016, A&A, 589, A110

Anderson, J. P., Habergham, S. M., James, P. A., & Hamuy, M. 2012, MNRAS, 424, 1372

Arcavi, I., Gal-Yam, A., Cenko, S. B., et al. 2012, ApJ, 756, L30

Arnett, D. 1996, Supernovae and Nucleosynthesis: An Investigation of the History of Matter from the Big Bang to the Present

Arnett, W. D. 1982, ApJ, 253, 785

Astier, P., Guy, J., Regnault, N., et al. 2006, A&A, 447, 31

Baade, W., & Zwicky, F. 1934, Physical Review, 46, 76

Balland, C., Baumont, S., Basa, S., et al. 2009, A&A, 507, 85

Barbon, R., Benetti, S., Rosino, L., Cappellaro, E., & Turatto, M. 1990, A&A, 237, 79

Barbon, R., Ciatti, F., & Rosino, L. 1979, A&A, 72, 287

Barnes, C., Hill, R. S., Hinshaw, G., et al. 2003, ApJS, 148, 51

Baron, E., Nugent, P. E., Branch, D., & Hauschildt, P. H. 2004, ApJ, 616, L91

Baumont, S., Balland, C., Astier, P., et al. 2008, A&A, 491, 567

Bazin, G., Palanque-Delabrouille, N., Rich, J., et al. 2009, A&A, 499, 653

Benedict, G. F., McArthur, B. E., Feast, M. W., et al. 2007, AJ, 133, 1810

Bennett, C. L., Hill, R. S., Hinshaw, G., et al. 2003, ApJS, 148, 1

Bersten, M. C., Benvenuto, O. G., Folatelli, G., et al. 2014, AJ, 148, 68

Bethe, H. A. 1990, Reviews of Modern Physics, 62, 801

Betoule, M., Kessler, R., Guy, J., et al. 2014, A&A, 568, A22

Bionta, R. M., Blewitt, G., Bratton, C. B., Casper, D., & Ciocio, A. 1987, Physical Review Letters, 58, 1494

Blake, C., & Glazebrook, K. 2003, ApJ, 594, 665

Blondin, S., Mandel, K. S., & Kirshner, R. P. 2011, A&A, 526, A81

Boulade, O., Charlot, X., Abbon, P., et al. 2003, in Proc. SPIE, Vol. 4841, Instrument Design and Performance for Optical/Infrared Ground-based Telescopes, ed. M. Iye & A. F. M. Moorwood, 72–81

Branch, D., Baron, E. A., & Jeffery, D. J. 2003, in Lecture Notes in Physics, Berlin Springer Verlag, Vol. 598, Supernovae and Gamma-Ray Bursters, ed. K. Weiler, 47–75

Branch, D., Benetti, S., Kasen, D., et al. 2002, ApJ, 566, 1005

Bronder, T. J., Hook, I. M., Astier, P., et al. 2008, A&A, 477, 717

Burrows, A. 2000, Nature, 403, 727

Burrows, A., & Goshy, J. 1993, ApJ, 416, L75

Caldwell, R. R., Dave, R., & Steinhardt, P. J. 1998, Physical Review Letters, 80, 1582

Cappellaro, E., & Turatto, M. 2001, in Astrophysics and Space Science Library, Vol. 264, The Influence of Binaries on Stellar Population Studies, ed. D. Vanbeveren, 199

Cardelli, J. A., Clayton, G. C., & Mathis, J. S. 1989, ApJ, 345, 245

Chandrasekhar, S. 1931, ApJ, 74, 81

Chevalier, R. A. 1976, ApJ, 207, 872

—. 1981, ApJ, 251, 259

Chevalier, R. A., & Fransson, C. 2008, ApJ, 683, L135

Chevalier, R. A., & Irwin, C. M. 2011, ApJ, 729, L6

Chugai, N. N., & Danziger, I. J. 1994, MNRAS, 268, 173

Colgate, S. A. 1974, ApJ, 187, 333

Colgate, S. A., & McKee, C. 1969, ApJ, 157, 623

Conley, A., Guy, J., Sullivan, M., et al. 2011, ApJS, 192, 1

Contreras, C., Hamuy, M., Phillips, M. M., et al. 2010, AJ, 139, 519

D'Andrea, C. B., Sako, M., Dilday, B., et al. 2010, ApJ, 708, 661

de Jaeger, T., Anderson, J. P., Pignata, G., et al. 2015a, ApJ, 807, 63

de Jaeger, T., González-Gaitán, S., Anderson, J. P., et al. 2015b, ApJ, 815, 121

Deng, J., et al. 2004, ApJ, 605, L37

Dessart, L., Blondin, S., Brown, P. J., et al. 2008, ApJ, 675, 644

Dessart, L., Gutierrez, C. P., Hamuy, M., et al. 2014, MNRAS, 440, 1856

Dessart, L., & Hillier, D. J. 2005, A&A, 439, 671

—. 2006, A&A, 447, 691

Dessart, L., Hillier, D. J., Waldman, R., & Livne, E. 2013, MNRAS, 433, 1745

Draine, B. T. 2003, ARA&A, 41, 241

Dunkley, J., Komatsu, E., Nolta, M. R., et al. 2009, ApJS, 180, 306

Eastman, R. G., Schmidt, B. P., & Kirshner, R. 1996, ApJ, 466, 911

Eldridge, J. J., Izzard, R. G., & Tout, C. A. 2008, MNRAS, 384, 1109

Elias-Rosa, N., Benetti, S., Turatto, M., et al. 2008, MNRAS, 384, 107

Elias-Rosa, N., Van Dyk, S. D., Li, W., et al. 2010, ApJ, 714, L254

—. 2011, ApJ, 742, 6

Ellis, R. S., Sullivan, M., Nugent, P. E., et al. 2008, ApJ, 674, 51

Emilio Enriquez, J., Leonard, D. C., Poznanski, D., et al. 2011, in Bulletin of the American Astronomical Society, Vol. 43, American Astronomical Society Meeting Abstracts #217, 337.21

Falk, S. W. 1978, ApJ, 225, L133

Falk, S. W., & Arnett, W. D. 1977, ApJS, 33, 515

Faran, T., Poznanski, D., Filippenko, A. V., et al. 2014a, MNRAS, 445, 554

—. 2014b, MNRAS, 442, 844

Filippenko, A. V. 1989, PASP, 101, 588

—. 1997, ARA&A, 35, 309

Fitzpatrick, E. L. 1999, PASP, 111, 63

Fixsen, D. J., Cheng, E. S., Gales, J. M., et al. 1996, ApJ, 473, 576

Folatelli, G., Morrell, N., Phillips, M. M., et al. 2013, ApJ, 773, 53

Folatelli, G., Phillips, M. M., Burns, C. R., et al. 2010, AJ, 139, 120

Folatelli, G., et al. 2015, ApJ, 811, 147

—. 2016, ApJ, 825, L22

Foreman-Mackey, D., Hogg, D. W., Lang, D., & Goodman, J. 2013, PASP, 125, 306

Fransson, C. 1982, A&A, 111, 140

Frieman, J. A., Bassett, B., Becker, A., et al. 2008a, AJ, 135, 338

Frieman, J. A., Turner, M. S., & Huterer, D. 2008b, ARA&A, 46, 385

Fukugita, M., Ichikawa, T., Gunn, J. E., et al. 1996, AJ, 111, 1748

Galbany, L., Hamuy, M., Phillips, M. M., et al. 2016, AJ, 151, 33

González-Gaitán, S., Tominaga, N., Molina, J., et al. 2015, MNRAS, 451, 2212

Goobar, A. 2008, ApJ, 686, L103

Grassberg, E. K., Imshennik, V. S., & Nadyozhin, D. K. 1971, Ap&SS, 10, 28

Gunn, J. E., Carr, M., Rockosi, C., et al. 1998, AJ, 116, 3040

Gunn, J. E., Siegmund, W. A., Mannery, E. J., et al. 2006, AJ, 131, 2332

Gutiérrez, C. P., Anderson, J. P., Hamuy, M., et al. 2014, ApJ, 786, L15

Guy, J., Sullivan, M., Conley, A., et al. 2010, A&A, 523, A7

Habergham, S. M., Anderson, J. P., James, P. A., & Lyman, J. D. 2014, MNRAS, 441, 2230

Hamuy, M. 2003, ApJ, 582, 905

Hamuy, M., Folatelli, G., Morrell, N. I., et al. 2006, PASP, 118, 2

Hamuy, M., Phillips, M. M., Suntzeff, N. B., et al. 1996, AJ, 112, 2391

—. 2003, Nature, 424, 651

Hamuy, M., Phillips, M. M., Wells, L. A., & Maza, J. 1993, PASP, 105, 787

Hamuy, M., & Pinto, P. A. 2002, ApJ, 566, L63

Hamuy, M., Pinto, P. A., Maza, J., et al. 2001, ApJ, 558, 615

Hamuy, M. A. 2001, PhD thesis, The University of Arizona

Harkness, R. P., & Wheeler, J. C. 1990, in Supernovae, ed. A. G. Petschek, 1–29

Hayden, B. T., Garnavich, P. M., Kessler, R., et al. 2010, ApJ, 712, 350

Hillebrandt, W., & Niemeyer, J. C. 2000, ARA&A, 38, 191

Hirata, K., Kajita, T., Koshiba, M., Nakahata, M., & Oyama, Y. 1987, Physical Review Letters, 58, 1490

Hogg, D. W. 1999, ArXiv Astrophysics e-prints

Hogg, D. W., et al. 2002, ArXiv Astrophysics e-prints

Holtzman, J. A., Marriner, J., Kessler, R., et al. 2008, AJ, 136, 2306

Howell, D. A. 2011, Nature Communications, 2, 350

Howell, D. A., Sullivan, M., Perrett, K., et al. 2005, ApJ, 634, 1190

Hoyle, F., & Fowler, W. A. 1960, ApJ, 132, 565

Hsiao, E. Y., Conley, A., Howell, D. A., et al. 2007, ApJ, 663, 1187

Hubble, E. 1929, Proceedings of the National Academy of Science, 15, 168

—. 1936, ApJ, 84, 517

Hubble, E. P. 1926, ApJ, 64

Iben, Jr., I., & Tutukov, A. V. 1984, ApJS, 54, 335

Ivezić, Ž., Lupton, R. H., Schlegel, D., et al. 2004, Astronomische Nachrichten, 325, 583

Ivezić, Z., Tyson, J. A., Axelrod, T., et al. 2009, in Bulletin of the American Astronomical Society, Vol. 41, American Astronomical Society Meeting Abstracts 213, 460.03

Jaffe, A. H., Ade, P. A., Balbi, A., et al. 2001, Physical Review Letters, 86, 3475

Janka, H.-T. 2001, A&A, 368, 527

Jones, M. I., Hamuy, M., Lira, P., et al. 2009, ApJ, 696, 1176

Kankare, E., Ergon, M., Bufano, F., et al. 2012, MNRAS, 424, 855

Kasen, D., & Woosley, S. E. 2009, ApJ, 703, 2205

Kim, A., Goobar, A., & Perlmutter, S. 1996, PASP, 108, 190

Kim, A. G., Gabi, S., Goldhaber, G., et al. 1997, ApJ, 476, L63

Kirshner, R. P., & Kwan, J. 1974, ApJ, 193, 27

Klein, R. I., & Chevalier, R. A. 1978, ApJ, 223, L109

Komatsu, E., Smith, K. M., Dunkley, J., et al. 2011, ApJS, 192, 18

Kotak, R., Meikle, W. P. S., Adamson, A., & Leggett, S. K. 2004, MNRAS, 354, L13

Krisciunas, K., Garnavich, P. M., Stanishev, V., et al. 2007, AJ, 133, 58

Landolt, A. U. 1992, AJ, 104, 340

Leavitt, H. S. 1908, Annals of Harvard College Observatory, 60, 87

Li, W., Leaman, J., Chornock, R., et al. 2011, MNRAS, 412, 1441

Lien, A. Y., Fields, B. D., Beacom, J. F., Chakraborty, N., & Kemball, A. 2011, in Bulletin of the American Astronomical Society, Vol. 43, American Astronomical Society Meeting Abstracts 217, 337.28

Magnier, E. A., & Cuillandre, J.-C. 2004, PASP, 116, 449

Maguire, K., Kotak, R., Smartt, S. J., et al. 2010, MNRAS, 403, L11

Marion, G. H., Brown, P. J., Vinkó, J., et al. 2016, ApJ, 820, 92

Massey, P., Morrell, N. I., Neugent, K. F., et al. 2012, ApJ, 748, 96

Maund, J. R., Smartt, S. J., Kudritzki, R.-P., et al. 2006, MNRAS, 369, 390

Mayle, R., & Wilson, J. R. 1988, ApJ, 334, 909

Millard, J., Branch, D., Baron, E., et al. 1999, ApJ, 527, 746

Minkowski, R. 1941, PASP, 53, 224

Moriya, T. J., Sanyal, D., & Langer, N. 2015, A&A, 575, L10

Nomoto, K. 1982a, ApJ, 257, 780

—. 1982b, ApJ, 253, 798

Nugent, P., Kim, A., & Perlmutter, S. 2002, PASP, 114, 803

Nugent, P., Sullivan, M., Ellis, R., et al. 2006, ApJ, 645, 841

O'Donnell, J. E. 1994, ApJ, 422, 158

Oke, J. B., & Sandage, A. 1968, ApJ, 154, 21

Olivares, F., Hamuy, M., Pignata, G., et al. 2010, ApJ, 715, 833

Pakmor, R., Kromer, M., Röpke, F. K., Sim, S. A., Ruiter, A. J., & Hillebrandt, W. 2010, Nature, 463, 61

Pastorello, A., Cappellaro, E., Inserra, C., et al. 2013, ApJ, 767, 1

Patat, F., Barbon, R., Cappellaro, E., & Turatto, M. 1994, A&A, 282, 731

Pejcha, O., & Prieto, J. L. 2015, ApJ, 799, 215

Percival, W. J., Reid, B. A., Eisenstein, D. J., et al. 2010, MNRAS, 401, 2148

Perlmutter, S., Aldering, G., Goldhaber, G., et al. 1999, ApJ, 517, 565

Perlmutter, S., Gabi, S., Goldhaber, G., et al. 1997, ApJ, 483, 565

Perrett, K., Balam, D., Sullivan, M., et al. 2010, AJ, 140, 518

Persson, S. E., Madore, B. F., Krzemiński, W., et al. 2004, AJ, 128, 2239

Phillips, M. M. 1993, ApJ, 413, L105

Phillips, M. M., Lira, P., Suntzeff, N. B., et al. 1999, AJ, 118, 1766

Phillips, M. M., Simon, J. D., Morrell, N., et al. 2013, ApJ, 779, 38

Pinto, P. A., & Eastman, R. G. 2000, ApJ, 530, 744

Planck Collaboration, Ade, P. A. R., Aghanim, N., et al. 2013, ArXiv e-prints

Planck Collaboration et al. 2015, ArXiv e-prints

Podsiadlowski, P., Joss, P. C., & Hsu, J. J. L. 1992, ApJ, 391, 246

Popov, D. V. 1993, ApJ, 414, 712

Poznanski, D., Butler, N., Filippenko, A. V., et al. 2009, ApJ, 694, 1067

Poznanski, D., Ganeshalingam, M., Silverman, J. M., & Filippenko, A. V. 2011, MNRAS, 415, L81

Poznanski, D., Nugent, P. E., & Filippenko, A. V. 2010, ApJ, 721, 956

Poznanski, D., Prochaska, J. X., & Bloom, J. S. 2012, MNRAS, 426, 1465

Regnault, N., Conley, A., Guy, J., et al. 2009, A&A, 506, 999

Rest, A., Scolnic, D., Foley, R. J., et al. 2014, ApJ, 795, 44

Richardson, D., Jenkins, III, R. L., Wright, J., & Maddox, L. 2014, AJ, 147, 118

Riess, A. G., Filippenko, A. V., Challis, P., et al. 1998, AJ, 116, 1009

Riess, A. G., Press, W. H., & Kirshner, R. P. 1996, ApJ, 473, 88

Rodríguez, Ó., Clocchiatti, A., & Hamuy, M. 2014, AJ, 148, 107

Rubin, V. C., Ford, W. K. J., & . Thonnard, N. 1980, ApJ, 238, 471

Sahni, V., & Starobinsky, A. 2000, International Journal of Modern Physics D, 9, 373

Saio, H., & Nomoto, K. 1985, A&A, 150, L21

Sanders, N. E., Soderberg, A. M., Gezari, S., et al. 2015, ApJ, 799, 208

Schlafly, E. F., & Finkbeiner, D. P. 2011, ApJ, 737, 103

Schlegel, E. M. 1990, MNRAS, 244, 269

Schmidt, B. P., Kirshner, R. P., Eastman, R. G., et al. 1994, ApJ, 432, 42

Schmidt, B. P., Suntzeff, N. B., Phillips, M. M., et al. 1998, ApJ, 507, 46

Scolnic, D., Rest, A., Riess, A., et al. 2014, ApJ, 795, 45

Scovacricchi, D., Nichol, R. C., Bacon, D., Sullivan, M., & Prajs, S. 2016, MNRAS, 456, 1700

Seo, H.-J., & Eisenstein, D. J. 2003, ApJ, 598, 720

Shanks, T., Allen, P. D., Hoyle, F., & Tanvir, N. R. 2002, in Astronomical Society of the Pacific Conference Series, Vol. 283, A New Era in Cosmology, ed. N. Metcalfe & T. Shanks, 274

Slipher, V. M. 1912, Lowell Observatory Bulletin, 2, 26

—. 1917, Proceedings of the American Philosophical Society, 56, 403

Smartt, S. J. 2009, ARA&A, 47, 63

—. 2015, PASA, 32, 16

Smartt, S. J., Eldridge, J. J., Crockett, R. M., & Maund, J. R. 2009, MNRAS, 395, 1409

Smith, J. A., Tucker, D. L., Kent, S., et al. 2002, AJ, 123, 2121

Smith, N., Li, W., Silverman, J. M., et al. 2011, MNRAS, 415, 773

Smith, N., & Owocki, S. P. 2006, ApJ, 645, L45

Spergel, D. N., Bean, R., Doré, O., et al. 2007, ApJS, 170, 377

Stoughton, C., Lupton, R. H., Bernardi, M., et al. 2002, AJ, 123, 485

Stritzinger, M., Hamuy, M., Suntzeff, N. B., et al. 2002, AJ, 124, 2100

Stritzinger, M. D., Phillips, M. M., Boldt, L. N., et al. 2011, AJ, 142, 156

Sullivan, M., Guy, J., Conley, A., et al. 2011, ApJ, 737, 102

Taddia, F., Stritzinger, M. D., Sollerman, J., et al. 2012, A&A, 537, A140

Taddia, F., et al. 2016, A&A, 587, L7

Takáts, K., & Vinkó, J. 2012, MNRAS, 419, 2783

Tartaglia, L., Pastorello, A., Taubenberger, S., et al. 2015, MNRAS, 447, 117

Taylor, M., Cinabro, D., Dilday, B., et al. 2014, ApJ, 792, 135

Thielemann, F.-K., Brachwitz, F., Höflich, P., Martinez-Pinedo, G., & Nomoto, K. 2004, NAR, 48, 605

Tominaga, N., Morokuma, T., Blinnikov, S. I., et al. 2011, ApJS, 193, 20

Tripp, R. 1998, A&A, 331, 815

Trumpler, R. J. 1930, PASP, 42, 214

Truran, J. W., Arnett, W. D., & Cameron, A. G. W. 1967, Canadian Journal of Physics, 45, 2315

Turatto, M., Benetti, S., & Cappellaro, E. 2003, in From Twilight to Highlight: The Physics of Supernovae, ed. W. Hillebrandt & B. Leibundgut, 200

Valenti, S., Howell, D. A., Stritzinger, M. D., et al. 2016, MNRAS

van den Bergh, S. 1959, Annales d'Astrophysique, 22, 123

—. 1990, PASP, 102, 1318

Van Dyk, S. D., Li, W., & Filippenko, A. V. 2003, PASP, 115, 1289

Van Dyk, S. D., Peng, C. Y., King, J. Y., et al. 2000, PASP, 112, 1532

Vink, J. S. 2008, New Astronomy Review, 52, 419

Vink, J. S., & de Koter, A. 2005, A&A, 442, 587

Walker, E. S., Hook, I. M., Sullivan, M., et al. 2011, MNRAS, 410, 1262

Webbink, R. F. 1984, ApJ, 277, 355

Welty, D. E., & Fowler, J. R. 1992, ApJ, 393, 193

Wheeler, J. C., & Harkness, R. P. 1990, Reports on Progress in Physics, 53, 1467

Whelan, J., & Iben, Jr., I. 1973, ApJ, 186, 1007

Wilson, O. C. 1939, ApJ, 90, 634

Woosley, S. E., Heger, A., & Weaver, T. A. 2002, Reviews of Modern Physics, 74, 1015

Woosley, S. E., Pinto, P. A., Martin, P. G., & Weaver, T. A. 1987, ApJ, 318, 664

Woosley, S. E., & Weaver, T. A. 1994, ApJ, 423, 371

—. 1995, ApJS, 101, 181

York, D. G., Adelman, J., Anderson, Jr., J. E., & Anderson, o. 2000, AJ, 120, 1579

Zwicky, F. 1933, Helvetica Physica Acta, 6, 110

—. 1935, The Scientific Monthly, 40, 461

—. 1939, Physical Review, 55, 726